Dissertation

submitted to the

Combined Faculty of Natural Sciences and Mathematics

of Heidelberg University, Germany

for the degree of

Doctor of Natural Sciences

Put forward by

Simon, Sailer

born in: Körle

Oral examination: 28.10.2020

The FlashCam camera for CTA:

trigger verification and

fluorescence light detection capabilities

Referees: Prof. Dr. Jim Hinton

Prof. Dr. Andreas Quirrenbach

Zusammenfassung

Das Gammastrahlen-Observatorium der nächsten Generation - das Cherenkov Telescope Array (CTA) - strebt an, die Entdeckungsfähigkeiten in einem breiten Energiebereich des Gammastrahlen Spektrums um einen Faktor 10 zu verbessern. Die FlashCam Kamera ist einer der auf den mittelgroßen Teleskopen (MST) installierten Kamera Typen, bestimmt für die Observation des mittleren Energiebereichs zwischen 150 GeV und 5 TeV. Der erste Teil dieser Arbeit übernahm die Aufgabe, das Trigger System von FlashCam zu verifizieren. Es wurden Studien zur Triggereffizienz und Triggerantwort auf Hintergrundlicht des Nachthimmels durchgeführt, anhand derer auch die Monte-Carlo Beschreibung des Detektors verbessert wurde. Der zweite Teil wurde der Untersuchung der möglichen Detektion von Fluoreszenzlicht durch den vollen 25 FlashCam-MST Unterdetektorverband anhand von Simulation gewidmet. Eine Triggerlogik wurde entwickelt, die die Detektion von Luftschauern, mit Primärenergien von mehr als 1 PeV, durch ihre Fluoreszenz Emission erlaubt. Die effektive Fläche dieser Detektionsmethode wurde bestimmt und die Winkelauflösung unter zuhilfenahme einer Schauerachsen Rekonstruktion berechnet. Die Kombination dieser einzelnen Untersuchungen erlaubte es, die Sensitivität auf punktförmige Gammastrahlen Quellen zu berechen, die in einem Energiebereich größer als 1 PeV emittieren.

Abstract

The next generation of Gamma-ray observatory - Cherenkov Telescope Array (CTA) - aims at improving the detection capabilities at a broad energy range of the gamma-ray spectrum by a factor of 10 in sensitivity. The FlashCam camera is one of the camera types mounted on the medium-sized telescopes (MST) of CTA, responsible for the observation of the core energy range between 150 GeV and 5 TeV. The first part of this thesis assumed the task of verifying the trigger system of FlashCam. Studies of the trigger efficiency and night-sky background light trigger response were performed, whilst also improving the Monte-Carlo description of the detector. The second part was dedicated to the research of the fluorescence light detection capabilities of the full 25 FlashCam-MST sub-array using simulations. A trigger logic was developed, which allows the detection of air showers with primary energies higher than 1 PeV through their fluorescence emission. The effective area of this detection method was determined and the angular resolution using a shower axis reconstruction calculated. The combination of these individual studies allowed the estimation of the sensitivity on point-like gamma-ray sources emitting in the energy range above 1 PeV.

Contents

Chapter 1

Introduction

Cosmic rays have first been detected in 1912 by Victor Hess, while studying the source of ionising radiation in the atmosphere with experiments performed during several balloon flights. He found that the ionisation rate decreased up to altitudes of ~ 1 km, as expected, but surprisingly increased for higher altitudes up to 5 km. The conclusion, that the source of the ionising radiation must come from beyond Earth's atmosphere lead to the discovery of cosmic rays. The endeavour to understand the nature of these cosmic rays for many decades lead to the remarkable all particle spectrum of cosmic rays spanning eleven orders of magnitude from $\sim 10^9$ eV up to energies of $\sim 10^{20}$ eV. Cosmic-rays at the lowest energy are generally understood to originate from solar flares of the sun. The source of the cosmic-rays up to the knee $\sim 10^{15}$ eV are attributed to galactic sources such as supernovae explosions. The generally accepted scenario regarding the source of these cosmic rays assumes, that cosmic rays below the "knee" mainly originate from within the Milky Way, with an interim region up to the "ankle", where the extra-galactic contribution takes over [17]. The detection of cosmic-ray accelerators has been furthered by the development of γ-ray detectors, as γ-ray photons are not deflected by the interstellar magnetic field (unlike charged cosmic-rays) and allow the observation of the production sites of cosmic-rays. The combined detectable range of the γ-rays spans from tens to hundreds of GeV using satellite experiments up to hundreds of TeV using ground-based detectors. Through these methods, hundreds of sources could be detected, ranging from Galactic emitters like pulsar wind nebula, supernova remnants to extragalactic sources like Active Galactic Nuclei and starburst galaxies.

In this work, the FlashCam camera proposed as a camera for the medium-sized telescopes of the Cherenkov Telescope Array will be presented. A detailed study of the trigger system and its systematics has been conducted, while simultaneously improving the Monte-Carlo description of the detector. The unique trigger system - allowing a reconfiguration due to its fully digital nature - offers the opportunity to extend the firmware and its abilities. This fact has lead to the research the detection capabilities of fluorescence emission of cosmic- and γ-ray air showers of energies above 1 PeV.

1.1 Acceleration mechanisms

A short overview of the acceleration mechanisms of charged particles and the production mechanisms of γ-rays is given in this section.

Acceleration of charged particles

The theory describing the acceleration of charged particles in the vicinity of strong shocks is referred to as "first-order" Fermi acceleration or diffuse shock acceleration [6]. The theory models the movement of relativistic charged particles as a diffuse process (random walk) with the particles conserving their energy on either side of the shock, while gaining energy when crossing [13]. Assuming the gas is highly ionised mono-atomic and a strong shock condition, the ratio of velocity upstream to downstream is 4. Particles crossing from upstream to downstream will thermalise, gaining energy and being accelerated by $\frac{3}{4}U$ with U being the velocity of the the shock in the laboratory frame, and by random motion due to the magnetic fields of the plasma, cross the shock again. From the downstream rest frame, the unshocked material approaches the particles with a velocity of $\frac{3}{4}U$, which will accelerate the particles once again.

Assuming a fixed fraction δ of kinetic energy gain per crossing, the energy of the particle will reach $E = E_0\delta^n$ after n crossings, with E_0 the initial energy of the particle. Also assuming, that this process has a probability p, whereby the particle escapes the shock front eventually, the remaining number of particles after n crossings will be $N = N_0 p^n$, with N_0 the number of original particles. Combining and differentiating yields $dN/dE \propto E^{-1+\frac{\log p}{\log \delta}}$. Taking relativistic effects of the shock crossing and the average angular distribution of the particles moving across the shock front into account, it can be shown (in this idealised case), that $\log p = -\log \delta$ leading to the power-law $dN/dE \propto E^{-2}$.

This process produces the observed power-law spectra in a natural way, with the maximum energy determined by the age and the size of the shock.

Synchrotron Radiation

Charged particles moving with relativistic speeds through regions with magnetic fields are deflected by the magnetic field (accelerated) and emit linearly polarised electromagnetic radiation. The emission observed in the laboratory frame has an opening angle of $\frac{1}{\Gamma}$ with Γ the Lorentz factor. The power of the emitted synchrotron radiation of an electron is given by the following relation:

$$P_{\mathrm{sync}} = -\frac{dE}{dt} = \frac{4}{3}\, c\, \sigma_{\mathrm{T}} \left(\frac{E}{m_e c^2})\right)^2 \beta^2\, u_{\mathrm{B}} \tag{1.1}$$

with σ_{T} the Thomson cross-section, $u_{\mathrm{B}} = B^2/(2\,\mu_0)$ the magnetic energy density (μ_0 the permeability in vacuum). The emitted power of any charged particle with

mass m scales with the mass like $P_{\text{sync}} \propto \frac{1}{m^4}$, leading to stronger synchrotron losses for lighter particles, making it a dominant process for light electrons (compared to protons with the same energy). The cooling time of an electron due to synchrotron losses is given by:

$$\tau_{\text{cool}} \cong 1.2 \cdot 10^3 \left(\frac{B}{10\mu G})\right)^{-2} \left(\frac{E_e}{100TeV}\right)^{-1} yr \tag{1.2}$$

Inverse Compton scattering

Compton scattering describes the process of the scattering of a sufficiently energetic photon on an electron, thereby transferring part of the photon's momentum onto the electron. An inverse process is possible, whereby cosmic ray electrons upscatter low energy photons from an ambient photon density field like the cosmic microwave background (CMB). This process can be separated into two regimes, depending on the photon energy of the ambient light field and the energy of the incoming electron. With

$$\epsilon = \frac{E_{\text{ph}}\, E_e}{m_e^2\, c^4} \tag{1.3}$$

the process is differentiated into the Thomson regime and the Klein-Nishina regime. With $\epsilon \ll 1$ the cross-section for the inverse Compton is

$$\sigma_{\text{IC,T}} \cong \sigma_{\text{T}}\,(1 - 2\epsilon) \cong \text{constant} \tag{1.4}$$

and for $\epsilon \gg 1$ (the Klein-Nishina regime) the cross-section is given by

$$\sigma_{\text{IC,KN}} \cong \frac{3\,\sigma_{\text{T}}\,\ln(4\epsilon)}{8\,\epsilon} \tag{1.5}$$

Due to the suppression of the Klein-Nishina regime for highly relativistic electrons, the energy loss of a cosmic ray electron can be approximated using the Thomson regime formula.

$$P_{\text{T}} = \frac{4}{3}\, c\, \sigma_{\text{T}} \left(\frac{E_e}{m_e c^2}\right)^2 \beta^2 u_{\text{R}} \tag{1.6}$$

with u_{rmR} the energy density of the photon field. The mass dependence of the energy loss rate with $\frac{1}{m^4}$ suppresses this process for particles with a much larger rest mass (hadrons).

Bremsstrahlung

Photons emitted by charged particles decelerating in the electrostatic field of another charged particle are called "Bremsstrahlung". The most common process involves electrons bending around ions and atomic nuclei. The energy loss of a

relativistic electron (or positron) due to Bremsstrahlung is given by:

$$P_{\mathrm{br}} = 4 n_{\mathrm{gas}} Z^2 r_e^2 \alpha \gamma m_e c^3 g \tag{1.7}$$

with Z the proton number, of the nucleus, n_{gas} the density of the target material, r_e the classical electron radius, α the fine structure constant and g the Gaunt factor, incorporating quantum and other corrections like the ionisation state of the gas.

$$\tau_{\mathrm{cool}} = \frac{E}{P_{\mathrm{br}}} \cong 4 \cdot 10^7 \left(\frac{n_{\mathrm{gas}}}{cm^3} \right) \mathrm{yr}) \tag{1.8}$$

Pion production

The inelastic interactions of cosmic ray protons with the interstellar medium (hydrogen gas and other nuclei) leads to the production of pions (neutral and charged), with a production ratio of $\sim \frac{1}{3}$ per resulting pion. The minimal kinetic energy needed of the cosmic ray proton for this process to occur is

$$E = 2 m_\pi c^2 + \frac{m_\pi^2}{2 m_{\mathrm{p}}} c^2 \cong 280\, MeV \tag{1.9}$$

with $m_\pi = 135\, MeV/c^2$ the pion mass, and $m_{\mathrm{p}} = 938\, MeV/c^2$ the proton mass. The charged pions decay further into muons and neutrinos, with the muons further decaying into electrons/positrons and neutrinos. The direct decay of the charged pions into electrons and neutrinos is possible, but highly suppressed with a branching ratio of $\sim 10^{-4}$. Detection of these neutrinos with experiments like IceCube may shed light onto the underlying production mechanism of γ-rays.

The dominant decay branch of neutral pions produced in such a hadronic interaction decay is via the electromagnetic interaction into two photons, in opposite direction (due to conservation of momentum). The average energy of the produced photons in the laboratory frame is $E_\gamma \cong 0.1\, E_{\mathrm{kin,p}}$

1.2 Extensive Air Showers

γ-rays cannot be directly detected on the ground, due to absorption by interaction with the atmosphere. For lower energy bands (<10 GeV), detectors on satellites like FERMI-LAT have proven effective. For higher energy ranges, the flux of γ-rays drops significantly, making the small effective area of satellites too small (within the life-time of the satellite). The alternative detection method using the Cherenkov emission from charged particles of the shower lead to the development of Imaging Atmospheric Cherenkov Telescopes (IACTs), pioneered by the Whipple collaboration [37]. The field developed further with the next generations of telescopes, with HEGRA [43] being the first to use a stereoscopic observation, and the following generations of the H.E.S.S. [29], MAGIC [9] and VERITAS [30]

telescope arrays opening up the field of γ-ray astronomy. The detection technique of IACTs makes use of the fact, that charged particles produced in extensive air showers induced by the primary particles (γ's, hadrons and electrons) move faster than the phase velocity of light through the air, thereby emitting Cherenkov photons, condensed in a focussed beam, while travelling to the ground.

Shower development

The first interaction of a VHE particle with atmospheric nuclei occurs at >10 km in altitude, creating secondaries, which in turn interact again with the particles of the atmosphere, producing a cascade of particles. The main processes in the production of these secondaries are *pair production* and *bremsstrahlung* in the case of electromagnetic interacting primaries and additional hadronic processed in the case of hadronic primaries.

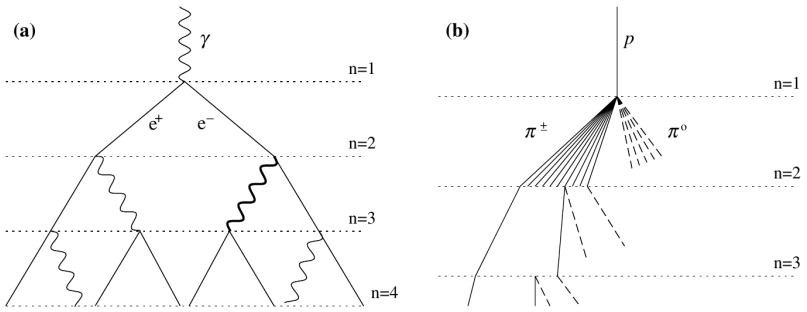

Figure 1.1: Shower cascade due to the Heitler model for an electromagnetic shower (a) and a hadronic shower (b). (image credit [41])

The Heitler model describing the cascading shower development of electromagnetic showers and the Heitler-Matthews [45] extended model describing the development of hadronic air showers have proven very successful. The assumptions of the electromagnetic model are:

1. In each step of the cascade, the same number of particles are produced.
2. The energy of the previous particle is evenly distributed among its secondaries.
3. If the particle is an electron or positron, bremsstrahlung occurs, resulting in a photon and the previous particle.
4. If the particle was a photon, pair production occurs, producing an electron and a positron.
5. The interaction length λ_{em} is the same for both processes on the order of the radiation length X_0 of an electron in air $\sim 37\,\mathrm{g/cm^2}$.
6. The cascade stops, when the ionisation losses of the charged particles dominate the losses due to bremsstrahlung at $E_c \cong 81\,MeV$.

The number of particles N_i, energy of each particle E_i and atmospheric depth of the step X_i at each step i of the cascade is then given by:

$$N_i = 2^i \tag{1.10}$$

$$E_i = \frac{E_0}{2^i} \tag{1.11}$$

$$X_i = i \cdot \lambda_{\mathrm{em}} \tag{1.12}$$

with E_0 the energy of the primary particle. The left panel of figure 1.1 shows the schematic view of the electromagnetic cascade. The depth of maximum shower development in units of radiation length is reached when

$$E_{i_{\mathrm{max}}} = \frac{E_0}{2^{i_{\mathrm{max}}}} = E_c \tag{1.13}$$

$$i_{\mathrm{max}} = \frac{\ln\left(E_0/E_c\right)}{\ln 2} \tag{1.14}$$

$$N_{\mathrm{max}} = \frac{E_0}{E_c} \tag{1.15}$$

$$X_{\mathrm{max}} = X_0 \frac{\ln\left(E_0/E_c\right)}{\ln 2} \tag{1.16}$$

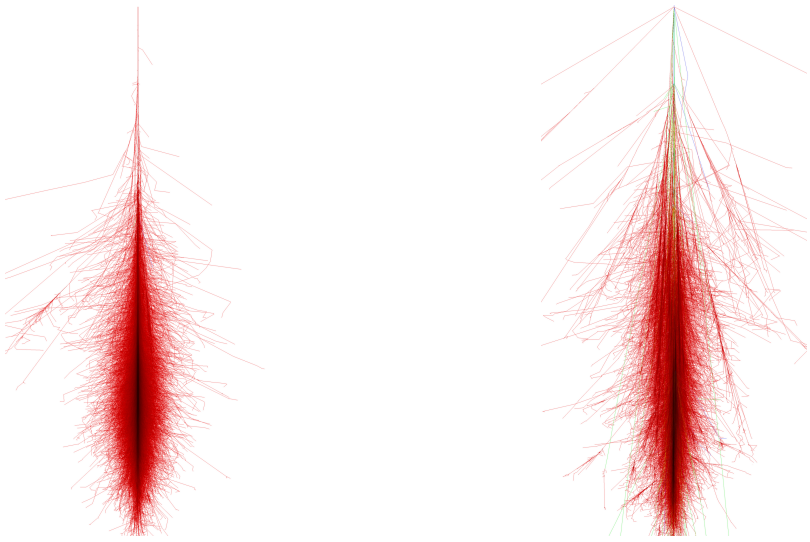

(A) Examplary γ-ray induced shower. **(B)** Examplary hadronic induced shower

Figure 1.2: A γ shower (A) and a proton shower (B), with an initial energy of 1 TeV simulated with CORSIKA. The electromagnetic shower is more compact than the hadronic shower, with its various sub-components. (image credit [55])

For hadronic showers, where the first interaction is mediated dominantly by the strong force, the picture is more complicated, with the most abundant particles being neutral and charged pions, but also kaons and other particles. Neutral pions decay into two photons transferring most of the energy of the shower into an electromagnetic sub-shower component. The charged pions interact again, producing a number of charged pions N_{ch} and $\frac{1}{2}N_{\mathrm{ch}}$ neutral pions. The assumption is, that a significant fraction of the parent particle is transferred to a single daughter

particle (the so-called leading particle), staying in the hadronic component of the shower. Charged pions with energies below $\sim 30\,\mathrm{GeV}$ decay mostly into muons and neutrinos. Since muons are minimum ionising particles in air and travel at relativistic speeds, they can reach the ground.[1]

The secondaries comprising a hadronic shower receive on average a larger transverse momentum, and in combination with the multiple sub-component showers lead to a larger lateral extent of hadronic showers (cf. fig 1.2).

Cherenkov emission

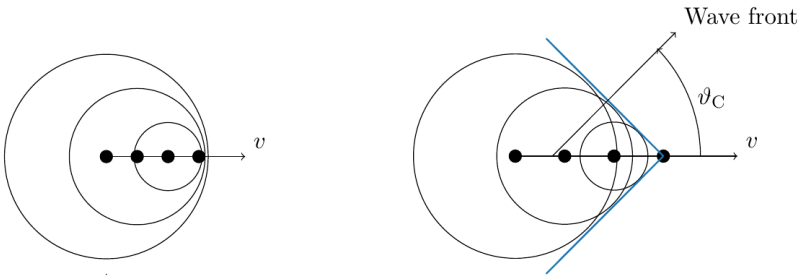

Figure 1.3: Cherenkov radiation principle. The particle in (a) is moving with a speed less than the phase velocity of light in the medium and the waves do not interfere. The particle in (b) is moving fast than the phase velocity of light in that medium, and the waves interfere constructively. This leads to the wave front of Cherenkov light, emitted with an angle θc. (image credit [52])

A charged particle moving through a dielectric medium causes a net polarisation of the surrounding particles through a displacement of the atoms and molecules present. This displacement is symmetric around the particle for speeds less than the phase velocity of light within that medium $v < c_0/n$, with v the speed of the particle, c_0 the speed of light in the vacuum and n the refractive index of the medium, and exhibits no far-field effect of the polarisation of the medium. If the velocity of the particle passing through the medium exceeds the phase velocity of light within that medium, i.e. $v > c_0/n$ a far-field dipole field develops and emits photons. The emission from each point of the track of the particle interferes constructively only in the direction, where the emitted light travels the same distances as the particle causing the emission. This is demonstrated in figure 1.3 (left panel $v < v_c$, right panel $v > v_c$). The angle of the emission is called the Cherenkov angle and depends on the speed of the incoming particle and the density of the medium:

$$\cos\theta\mathrm{c} = \frac{1}{\beta n} \tag{1.17}$$

[1]These muons are used in detector experiments to determine the nature of the primary particle, as they clearly identify a hadronic primary particle.

The minimal energy of a particle emitting Cherenkov light is given by:

$$E_{\min} = \frac{m_0 c^2}{\sqrt{1 - n^{-2}}} \tag{1.18}$$

As the refractive index n depends on the atmospheric conditions (mainly density), θc and $E_{\min}$ change accordingly. The minimum energy of an electron moving through the atmosphere changes from ~ 40 MeV at ~ 10 km altitude to ~ 20 MeV at sea level. Similarly the emission angle of the Cherenkov light changes from $\sim 8°$ to $\sim 1.4°$, with the maximum angle (for $\beta \cong 1$) approaching $\arccos(1/n)$. The angle of emission increases therefore with the particle travelling down to earth concentrating the emitted light into a cone shaped form with the arrival time of all Cherenkov photons on the order of nanoseconds. For an extensive air shower, the contributions from the slightly scattered charged particles (mainly electrons and positrons) overlap on the ground filling the so-called Cherenkov light pool, with a radius ~ 120 m on the ground (at ~ 2 km a.s.l). Figure 1.4 shows the emission angles from a single charged particle and the total light pool of an exemplary air shower.

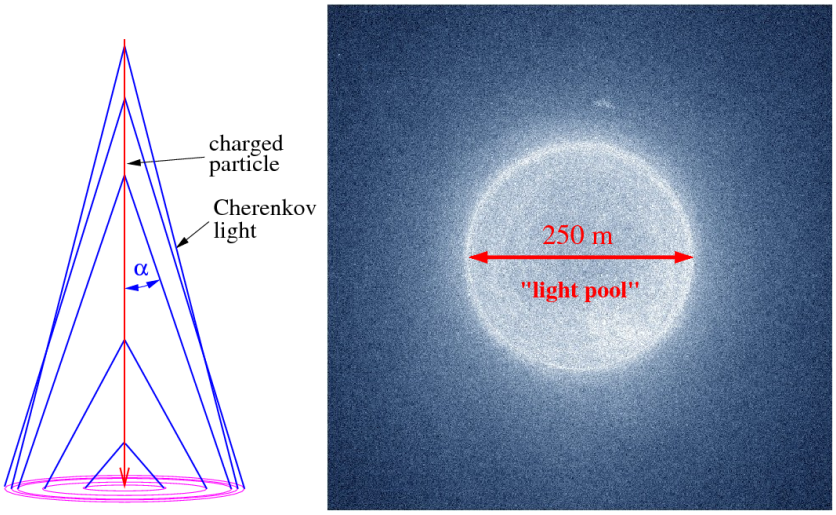

Figure 1.4: Depiction of the change in Cherenkov emission angle with decreasing altitude of the emitting particle (left). The light pool detected on the ground is shown on the right panel (image credit [59]).

The number of Cherenkov photons emitted along the track depending on the unit wavelength λ and the unit length x is expressed by the Frank-Tamm formula:

$$\frac{dN}{dx d\lambda} = 2\pi\alpha z^2 \left(1 - \frac{1}{\beta^2 n^2}\right) \tag{1.19}$$

with α the fine structure constant, z the particle charge, and $n = n(\lambda)$ depending on the wavelength of the emitted Cherenkov light. The detected Cherenkov emission spectrum at ground peaks at a wavelength $\sim$300-350 nm, in the blue region of the visible light spectrum due to strong absorption processes in the UV

region. The formula is only valid in the regime where the Cherenkov condition holds, otherwise a UV explosion due to the $1/\lambda$ dependence would occur.

Fluorescence emission

An additional optical emission is produced by extensive air showers, namely the isotropic fluorescence emission in the near UV and optical light spectrum. Fluorescence light is emitted by the spontaneous de-excitation of nitrogen molecules in the air, where the excitation was induced by the charged particles of the air shower. Due to the isotropic emission, the shower can be viewed side-on and along its development (depending on the field of view of the detector).

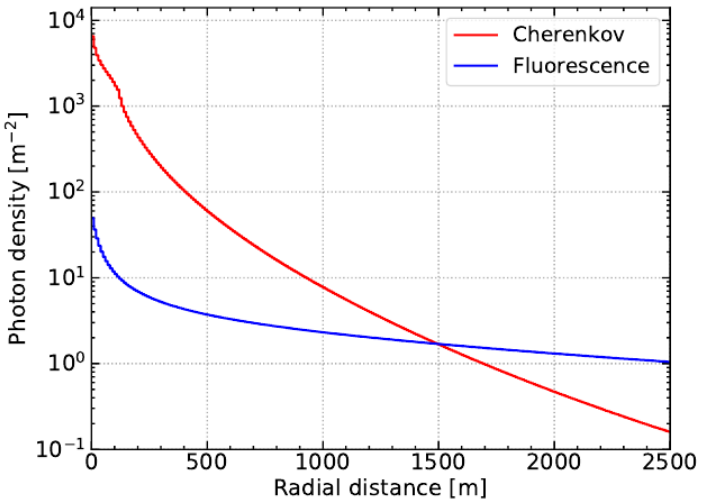

Figure 1.5: The average radial distribution of all Cherenkov and fluorescence light emitted from a 10 TeV γ-ray shower. (image credit [47])

The number of fluorescence photons emitted by nitrogen is proportional to the deposited energy E_{dep} of the ionising particles in the volume observed by a detector, allowing a calorimetric measurement of the shower.

$$\frac{dN_\gamma}{dX} = \frac{dE^{\text{tot}}_{\text{dep}}}{dX} \cdot \int Y(\lambda, T, p) \cdot \tau_{\text{ATM}}(\lambda, X) \cdot \epsilon_{\text{FD}}(\lambda, X) d\lambda \tag{1.20}$$

with $Y(\lambda, T, p)$ the fluorescence yield [54, 48] depending on pressure, temperature and wavelength, ϵ_{FD} the detector efficiency, τ_{ATM} the transmittance of the atmosphere. A good approximation for the fluorescence yield is ~ 4 photons/m for an electron energy of ~ 0.85 MeV, determined through laboratory experiments of nitrogen fluorescence emission [39]. The spectrum of the fluorescence emission (cf. fig. 1.6) overlaps with the Cherenkov spectrum, making it possible to detect the fluorescence photons also with IACTs.

So far, the fluorescence emission has been largely treated as a contamination in the detection of Cherenkov photons, but research into the validity of using the fluorescence emission as an additional signal in IACTs has been undertaken [47].

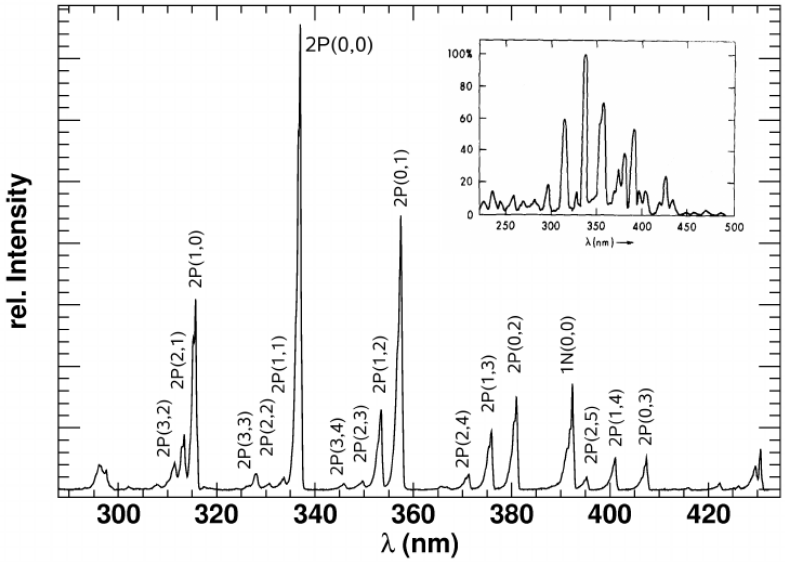

Figure 1.6: The fluorescence spectrum of air between 280 nm and 430 nm as measured by the AIRFLY experiment, with the dominant transition at 337 nm. The nitrogen gas was excited with 3 MeV electrons at a pressure of 800 hPa. Top right shows the spectrum reported by Bunner (1967). (image credit [48])

Due to the isotropic nature, much larger impact distances of showers can be observed (as very successfully demonstrated by the Pierre Auger Observatory [3], among others), increasing the effective area for VHE und UHE primary particles considerably, compared to the usual Cherenkov detection method (see figure 1.5 for a comparison of photon intensities as function of impact distance between Cherenkov and fluorescence emission).

1.3 Imaging Atmospheric Cherenkov Telescopes

As mentioned previously, Imaging Atmospheric Cherenkov Telescopes image the Cherenkov emission of air showers by observing the shower from within the light pool of the emission on the ground (cf. fig 1.7). The light pool of a typical air shower extends up ~ 150 m depending on the elevation of the detectors. Typically 100 Cherenkov photons per m^2 at 1 TeV primary energy are observed within a time frame on the order of nanoseconds, making the detectable minimal energy related to the size of the mirror dish of a telescope. The dish size of the CT5 telescope of the H.E.S.S. experiment amounts tot $614\,m^2$ reducing the energy threshold to $O(20\,\text{GeV})$. A considerable background due to the Night Sky light is present, requiring the typically fast sampling rate of the cameras. Additional trigger mechanisms have to be deployed to find the fast elliptical shaped images of the air showers. The reconstruction of those images makes use of the fact, that the elongated shower form (due to the highly relativistic travelling shower particles) points back to the direction of origin of the primary particle, with showers induced by γ-rays being more compact.

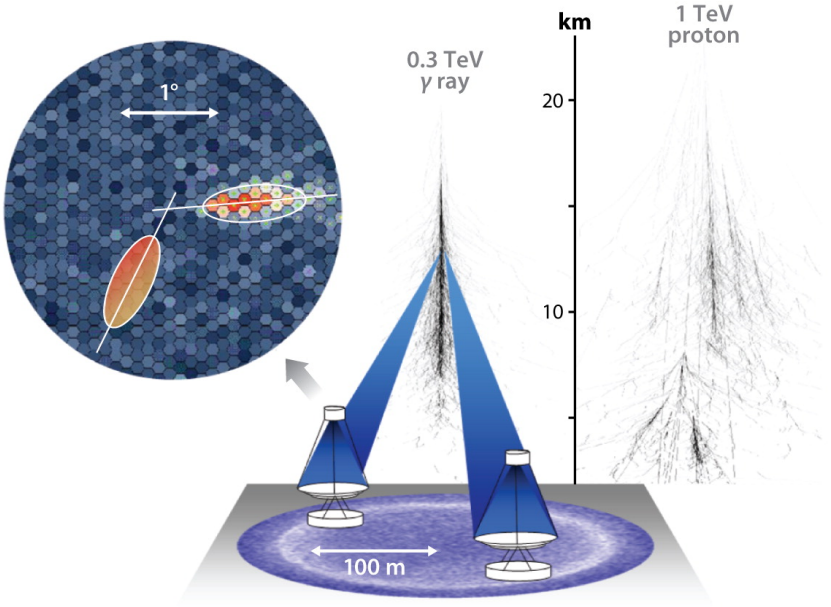

Figure 1.7: Detection principle of stereoscopic operating Imaging Atmospheric Cherenkov Telescopes. (image produced by K. Bernlöhr, taken from Hinton & Hofmann [28])

The mirror layout of the telescopes allows each pixel to observe a different part of the sky, while seeing the full mirror dish (hence "imaging"). Each pixel in the camera corresponds then to a different angle on the sky, enabling the measurement of the shower extent by the angular separation of the hit pixels. The angular resolution of the telescopes is vastly improved by using a stereoscopic reconstruction method, observing the shower from different directions (typical angular resolution $\sim 0.1°$), while also enabling coincidence triggers, reducing trigger contributions from the night-sky background fluctuations. Examples of working operating experiments are H.E.S.S, VERITAS and MAGIC, deploying five, four and two telescopes respectively.

Cherenkov Telescope Array

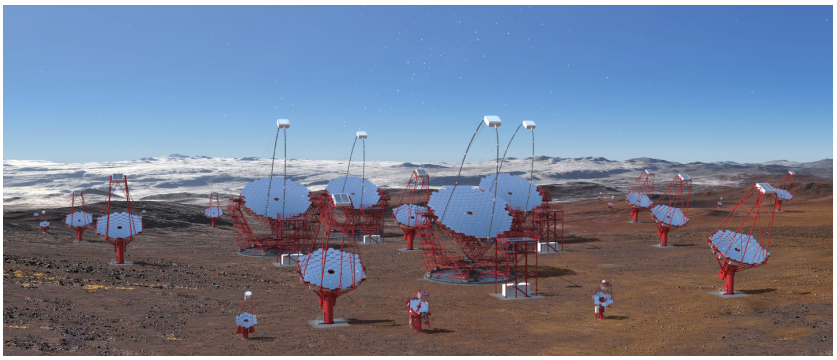

Figure 1.8: Artist's impression of the CTA south observatory (G. P. Diaz)

The Cherenkov Telescopes Array is the next generation of γ-ray experiments [56], and with an international combined effort expected to be deployed on two sites covering both the Southern and the Northern sky. The Southern location is planned in the Paranal desert, Chile, where observations of the Galactic Plane are favoured, while the Northern location on La Palma, Spain has been chosen due to favourable conditions observing extragalactic sources. The sensitivity requirements for both target types are different, with the focus on the VHE energy band in the south (up to 300 TeV) and the low energy bands focusing an transient sources down to $\sim$20 GeV. Three classes of telescope sizes are in development covering the energy range of 20 GeV up to 300 TeV, the small-, medium- and large-sized telescopes (SST, MST, LST respectively), the dish sizes range in diameter from 8 m, 12 m up to 23 m. The focus of the LSTs with their large mirror area is on the low energy band, where the fainter images require larger detection areas, and the required number of telescopes (4) is less, due to the higher flux of particles. The SSTs on the other hand (only deployed in the South), will focus on the high energy range of the observatory, being deployed over a large area of several km^2 in high numbers (70). The sensitivity of the observatory in core energy range will be provided by the MSTs (between 150 GeV up to 5 TeV). The total sensitivity in comparison to existing observatories is given in figure 1.9, while the layout of both sites is shown in figure 1.10. The sensitivity improvement compared to the existing generation of IACT arrays is by a factor of $\sim$10. The field of views of the telescopes vary between 5° and 10°.

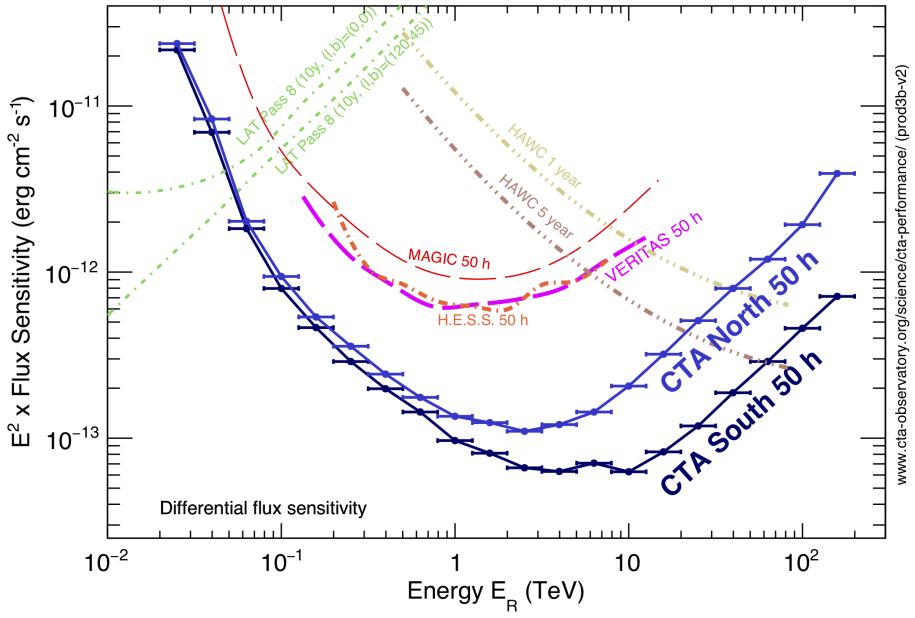

Figure 1.9: Expected flux sensitivity the CTA North and South compared to existing experiments. (image credit [49])

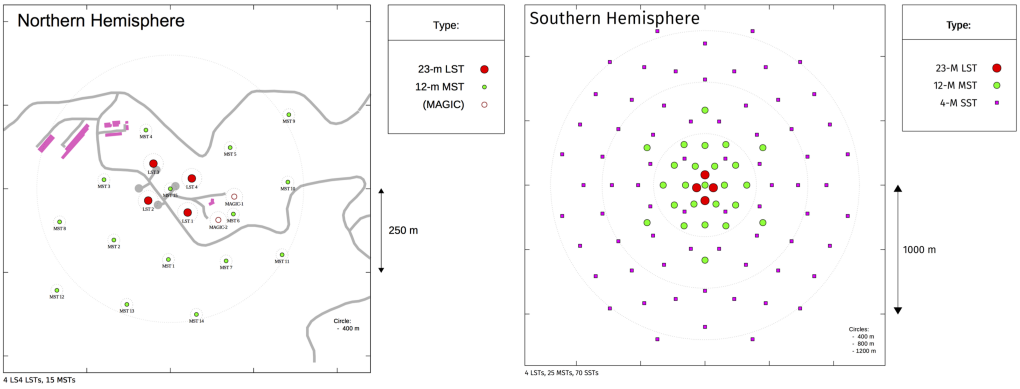

Figure 1.10: The proposed layout of the Northern and Southern array, on La Palma and in the Paranal desert, respectively.(image credit [49])

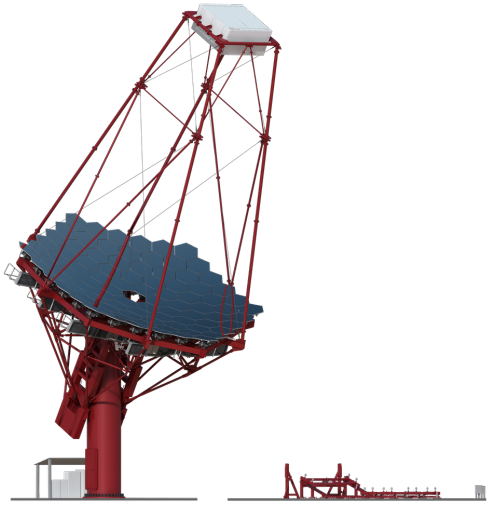

Figure 1.11: Artist's impression of the medium-sized telescope (MST) (G. P. Diaz)

Medium-sized telescope The MST telescope structure (cf. fig.1.11) follows a modified Davis-Cotton design, with curved mirror segments (flat-to-flat diameter is 1.2 m) aligned on a spherical surface with a curvature of 19.2 m [19]. The 84 mirrors are moveable, with actuators enabling a high precision alignment to the camera, ensuring a small point spread function of the telescope. The effective mirror area is 88 m^2 include the shadowing effects from the camera and the mast structure. The camera is mounted in the telescope's focal plane at a distance of 16 m. The central mirror space is used to hold a camera calibration device (laser unit) and a lid CCD for pointing calibration using LEDs on the camera body. The CCD is also used for the mirror alignment process. The expected pointing precision is within <7 arc-seconds and a re-pointing time <90 s.

The designs for the full CTA observatory expects deployment of 25 MSTs in the South and 15 MSTs in the North. Two camera prototypes are proposed for the final design: NectarCam [53] and FlashCam [20].

At the time of this work, a final decision regarding a possible choice has not

been announced. Chapter 2 provides a more in depth discussion of FlashCam, as the main focus of this work revolved around the trigger verification of FlashCam and the fluorescence detection capabilities of the MST sub-array of CTA South equipped with FlashCam cameras.

1.4 PeV detection perspective

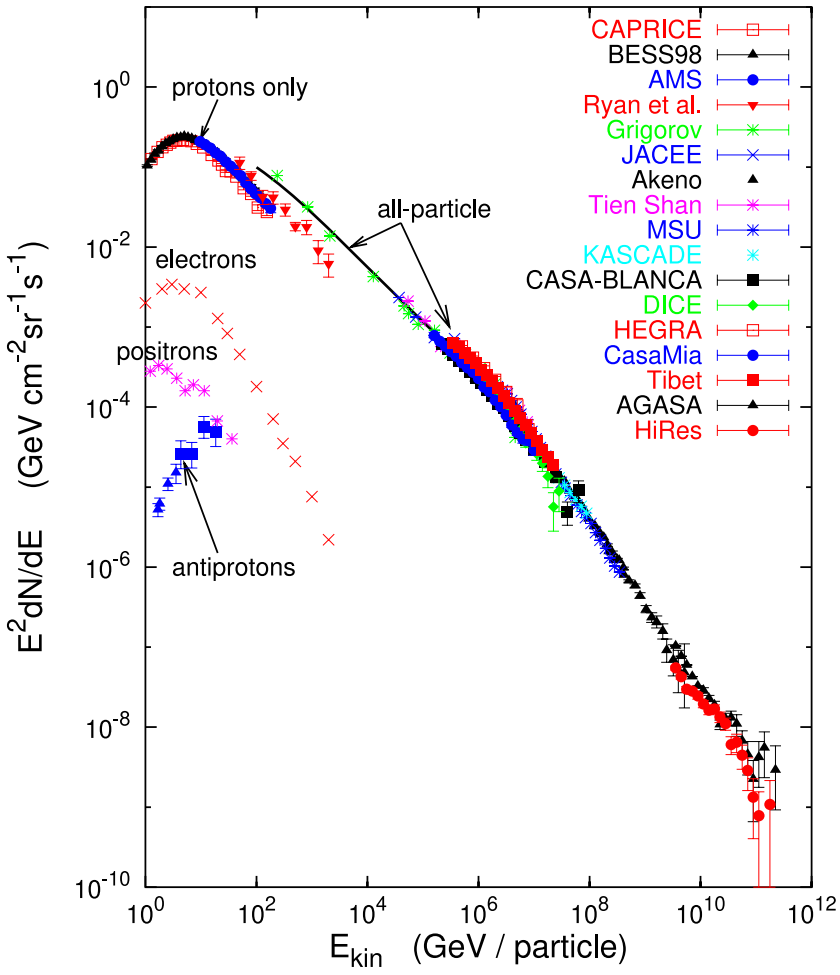

Figure 1.12: (credit Gaisser, 2006 [17].)

Cosmic rays with energies up to the knee ($3 \cdot 10^{15}$ eV) are attributed to the acceleration in collisionless shock fronts, e.g. generated in supernova remnants, where the ejecta of the supernova explosion sweep up the galactic interstellar material [13], while the cosmic rays around the ankle come from extragalactic sources. The softening of the spectrum beyond the knee is interpreted as being correlated with the maximum achievable acceleration of cosmic-rays by sources in the Galaxy. Additionally, the change in the composition of the cosmic-ray population around the knee from dominantly protons to heavier nuclei supports this interpretation, as a shift in the cut-off energy of the spectra is explained by the different magnetic rigidities ($\propto E/Z$) of the different nuclei, resulting in

the maximal attainable energy of heavy nuclei at around $\sim 10^{17}$ eV (under the assumption of a maximum proton energy of $\sim 10^{15}$ eV). An additional suspected feature between the knee and the ankle, the "second-knee" ($\sim 10^{17}$ eV), with a second steepening of the spectral index, maybe indicating a second Galactic cosmic-ray component, with a higher cut-off energy.

The maximum containment energy of cosmic-ray protons due to the typical Galactic magnetic field strength ($3\mu G$) is around $\sim 10^{18}$ eV, allowing the escape of cosmic-rays above the energy of the ankle, thereby interpreting cosmic-rays in that energy band of extragalactic origin. Several models explain the transition regime between the knee and the ankle (see reviews: [31, 5]) with the general consensus, that Galactic sources, able to accelerate cosmic-rays up to >PeV energies, should exist.

Due to the deflection of charged cosmic-rays by the magnetic background field in the Milky Way, γ-rays provide an excellent tool to probe the origin of the cosmic-rays, as they travel non-deflected (disregarding negligible gravitational effects) to the Earth, pointing back to their origin.

Sources capable of accelerating cosmic-rays to >PeV energies should also act as γ-ray sources (through hadronic interactions nearby). The characteristic expected power law spectra in γ-rays should extend up to ≥ 100 TeV without cut-off or spectral break, with a hard spectral index ~ 2.

The H.E.S.S. Collaboration reported γ-ray emission from the Galactic centre region (Sagittarius A* [26]) consistent with a PeVatron acceleration site, albeit not with a high enough rate. Alternative sources such as young massive star clusters have been proposed [4]. The HAWC observatory recently reported the discovery of sources with γ-ray energies >54 TeV (and >100 TeV) [2]. Additional searches have been performed by IceCube, using five years of data, providing upper limits to the unbroken power law hypothesis of several sources and on the diffuse γ-ray flux from the Galactic plane [1].

The upcoming Cherenkov Telescope Array is expected to provide the sensitivity (with energies up to 300 TeV) to probe the γ-ray emission of promising sources with hints of hard spectra without cut-off or breaks.

The work presented in chapter 4 will demonstrate the feasibility of using the fluorescence emission of air showers to detect γ-ray with energies >1 PeV with a 25 FlashCam-equipped MST sub-array. It shall be noted here that γ-γ absorption effects, where $\sim$ PeV γ-rays interaction with the radiation fields, may play a role. Studies have shown, that the maximum of absorption at ~ 2 PeV reduces the average diffuse γ-ray flux over the whole Galaxy by $\sim 30\%$ [57].

Chapter 2

FlashCam

In this chapter, an overview of the FlashCam camera design is given, with a detailed review of the trigger system. The laboratory set-up used to study the trigger performance is shown, and the relevant concepts of the signal and trigger signal calibration are highlighted. The main improvements of the Monte-Carlo detector simulation description, worked out during the course of this work, are reported in the last section.

2.1 FlashCam camera concept

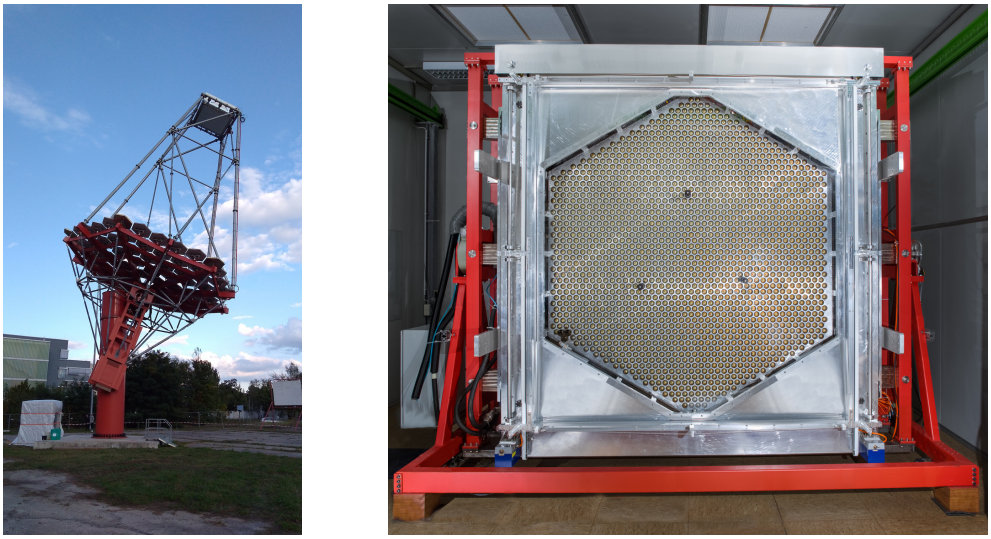

(A) The FlashCam prototype mounted on the MST prototype structure in Berlin-Adlershof in September, 2017.

(B) Frontal view of the FlashCam mounted in a rotating test frame. At the time of this picture, the Winston light guides had not been installed

Figure 2.1: Images of the FlashCam prototype mounted in the MST prototype structure and in the laboratory (kindly provided by C. Föhr.)

The FlashCam camera is designed as a walk-in camera implementing a modular design philosophy (cf. 2.2), with the separated photon detector plane (PDP), the readout electronics (ROS) and the data acquisition system (DAQ) as the key camera sub-systems. The readout and trigger system uses a novel fully-digital approach, whereby the trigger decision is computed from the sampled analogue

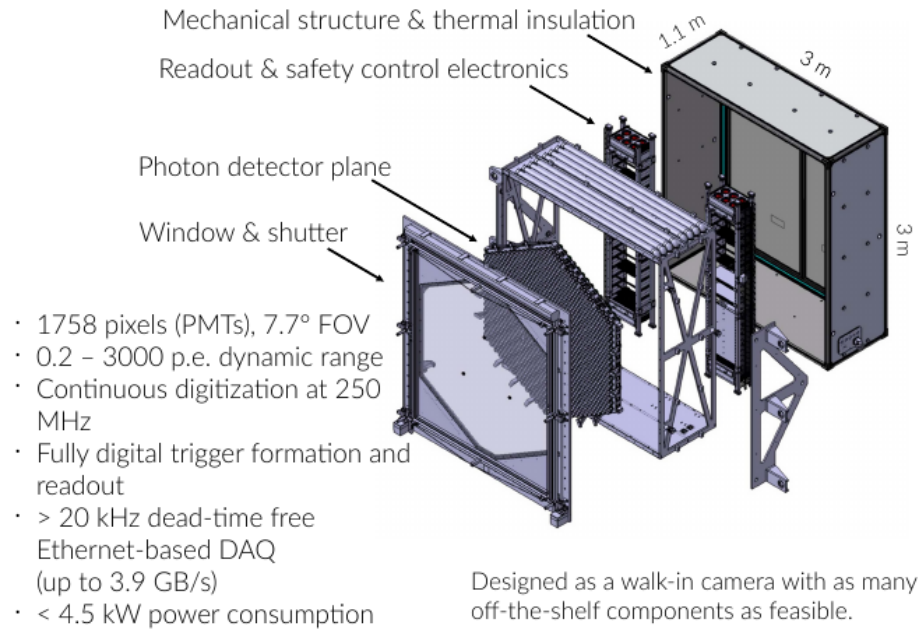

Figure 2.2: FlashCam camera concept with highlights of the key technical specifications (credit FlashCam team).

output of the photon detectors in the front-end electronics, without a separate analogue trigger path, thereby removing the additional systematic uncertainty such a separate signal processing path introduces.

Additional auxiliary sub-systems are located inside the camera housing, the camera safety system, power distribution, slow control interfaces and cooling. A unique feature of FlashCam is the spatial separation of the PDP from the readout electronics, connected via Ethernet cables transmitting the amplified analogue signals differentially to the digitisation boards, making an exchange of the photon detection modules an easy task (e.g. maintenance or upgrades). The analogue signals of the photomultipliers are then sampled with 12-bit analogue-to-digital converters (ADCs) at a rate of 250 MS/s and buffered continuously in a ring-buffer in the FPGAs located on the digitisation boards. This ring-buffer spans a time interval of 16μs. The trigger system operates on these buffered samples to form a trigger decision on a sample by sample basis.[1] If a trigger decision is made, the readout system transfers a length configurable (<15.6μs) and delay adjustable time slice of the waveforms into a secondary event buffer, which are then read out from the camera server via a raw Ethernet based networking protocol.

The camera server is connected from outside the camera via four 10 Gbit/s Ethernet fibres to camera-internal network switches, which in turn are connected to the ADC boards via 1 Gbit/s Ethernet based connections. The individual traces of all ADC channels are then merged into an event on the camera server and, depending on the operation mode, transferred to the array computing cluster, or stored on the readout server itself. Additionally, a central trigger decision between

[1]The trigger system is detailed further in the next section 2.2.

the telescopes is supported via a software array trigger interface operating on the camera readout server. An overview of key systems is given in figure 2.3.

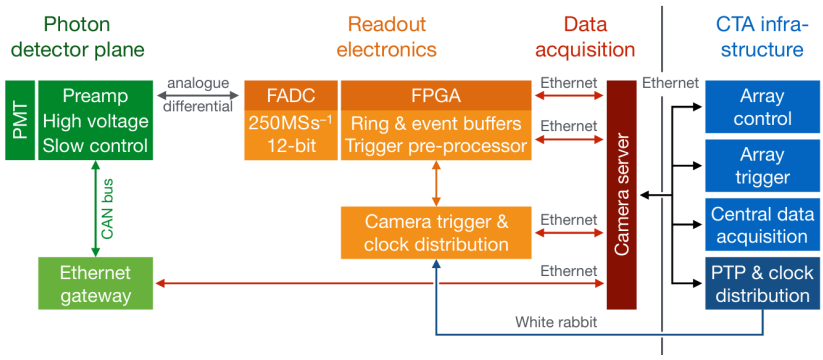

Figure 2.3: Schematic of the photon detection, readout electronics and data acquisition. (credit F.Werner [60]).

Camera body

An exploded view of the camera mechanics are shown in figure 2.2, with dimensions of 3x3x1.1m^3. It was designed with the aim to allow easy access to all contained subsystems, making it a "walk-in" camera. The read of the camera can be opened using two doors spanning the full height of the camera body. The camera housing is built around a load-carrying frame, connecting the camera to the telescope mast structure. The walls of the camera housing are made from aluminium-foam composite (used also as a thermal insulator). The telescope facing side of the camera body is equipped with a transparent window, shielding the photon detection plane and keeping the interior dust free. Light concentrators are installed between the holding structure of the PDP modules and the window, with a 50 mm flat-to-flat hexagonal entrance area. These cones are installed to reduce the dead space between the individual photo cathodes of the PMTs and are shaped in such a way, that stray light coming outside the mirror-dish of the telescope is rejected [52].

A lid is installed in front of the camera window, which functions like a roller shutter, minimising shadowing effects on the telescope mirrors during operation and making the camera light-tight during daytime. The total weight of the camera including all internal components is <2 tons.

Cooling

The FlashCam electronics crates are actively cooled via forced air-flow by four fan units installed on the top and on the bottom of each 19-inch racks. Additionally, four air-to-water heat exchanger are placed in between, connected via a closed circuit to a chiller unit outside of the camera on the ground. The air flows through the fans inside the electronics racks from the bottom and the top, thereby creating convection inside the camera. The PDP is passively cooled, supported by this

convection. The total power draw of FlashCam is <4.5 kW, excluding the outside components (chiller and readout server).

PDP

(A) Front with photomultiplier tubes facing the telescope mirrors

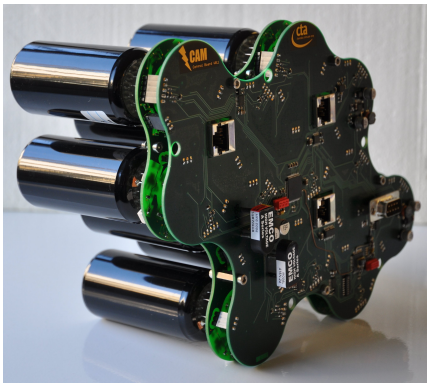

(B) Backview with 3 RJ45 connectors for the Ethernet cables, transfering the differential analogue signals to the ADC boards.

Figure 2.4: A photon detector plane module (PDP module) of which 147 are installed in a fully-equipped FlashCam, with 12 photomultiplier tubes mounted. The shape of the module allows seamless alignment, resulting in the hexagonal shape of the PDP.

The camera photon detection plane is equipped with 147 individual modules forming the hexagonal detection plane. Each module hosts twelve 1.5-inch photomultipliers (PMTs) soldered to the printed circuit board (PCB) structure. These PCBs house the pre-amplifiers, the high-voltage (HV) supply for each pixel, as well as a microcontroller for slow control of the module, with a total power consumption of ~2.8 W. Also equipped are three Ethernet plugs connecting the module to the readout system via Ethernet cables and the D-Sub connector, which provides the CAN-bus interfaces for the slow control and the 24 V power supply. The dynamic range of the signals is up to >3000 PE using a non-linear amplification scheme for signals >250 PE, where the amplification process changes from a linear regime into a controlled saturated regime. The analysis in the saturated regime is performed by evaluating the integral of the pulses, which grows logarithmically with input charge.

Two PMT types have been installed in the FlashCam prototype with different numbers of dynodes; the 7-dynode (R12992) PMT and the 8-dynode PMT (R11920). The layout is given in figure A.1 of appendix B. Both types exhibit small differences in their pulse shapes, afterpulsing and single photoelectron spectrum, with consequences on the signal and trigger signal chain, which will be shown later in this chapter. A detailed study of their characteristics has also been performed [15].

ROS

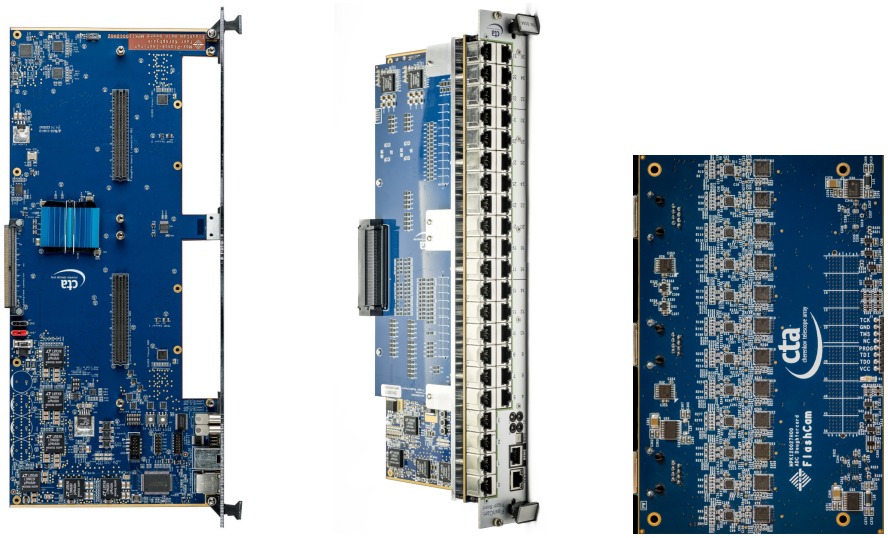

(A) FlashCam mother board. **(B)** FlashCam trigger board. **(C)** ADC piggy board with 12 readout channels. Two per mother board.

Figure 2.5: Images of a FlashCam mother board (A) equipped with a trigger card (B) and a separate ADC piggy board (C). The modular design make use of the same underlying motherboard using a Xilinx Spartan-6 FPGA.

The front-end electronics of FlashCam are designed using common platform, the motherboard, hosting a Xilinx Spartan-6 FPGA, a 1 GBit/s Ethernet interface, a clock and trigger interface and a backplane connector [25]. The functionality of the board is determined by the daughter boards plugged into the onboard high-density connectors and the corresponding loaded firmware. Three types of daughter cards have been designed, the digitiser card (ADC card) using one or two ADC daughter boards with 12 ADC channels (resulting in up to 24 readout channels per ADC card), the trigger card using one daughter board (using both connectors to the motherboard) and the master distribution board, responsible for the camera wide (GPS) clock and trigger signal distribution (cf. fig. 2.5).

The readout system uses common trigger and clock interface named CTI, which synchronizes the components of the system to common clock, ensuring that all components run in the same phase. A sync signal is transmitted via the CTI interface, sending an absolute time stamp (pulse per second, PPS) and broadcast commands to the attached sub-cards (in FlashCam the trigger cards). The commands include readout signals, start/stop of the data acquisition, etc.

The master distribution board distributes the external GPS clock to the 12 connected trigger cards, which distribute the common clock signal further to the ADC cards (84 in total, 7 per trigger card). The reverse signal path transmits the pre-trigger signals from the ADC cards to the trigger cards, which exchange their information with topologically neighbouring trigger cards to form a trigger decision, which in turn gets transmitted to the master distribution board, where an

individual trigger decision triggers a readout signal to the ADC boards,inducing the copying of the set time slice from the continuous running ring-buffer into the event buffer. The main advantage of this common interface is a synchronous operation of all front-end electronic cards, which operate on a 250 MHz time basis, with fixed delays between all cards of the hierarchy, ensuring a synchronous event building. The combined data process rate of the ADC boards is ~5.3 Tbit/s, all trigger cards process around ~1.5 Tbit/s of input data, reducing the data stream further to 0.25 Tbit/s, the final trigger decision rate of the master distribution board. The event data readout rate of the system is >3.3 GByte/s with a possible dead-time free trigger rate >20kHz, depending on the set trace length during data acquisition.

The electronics are housed inside the camera in mini-crates, with seven ADC cards and one trigger card per mini-crate. twelve mini-crates are deployed in two 19-inch racks with four mini-crates connected to one of the three sectors of the photon detection plane. An image of the rear of the camera housing is shown in figure 2.6, while a schematic overview is shown in figure 2.7.

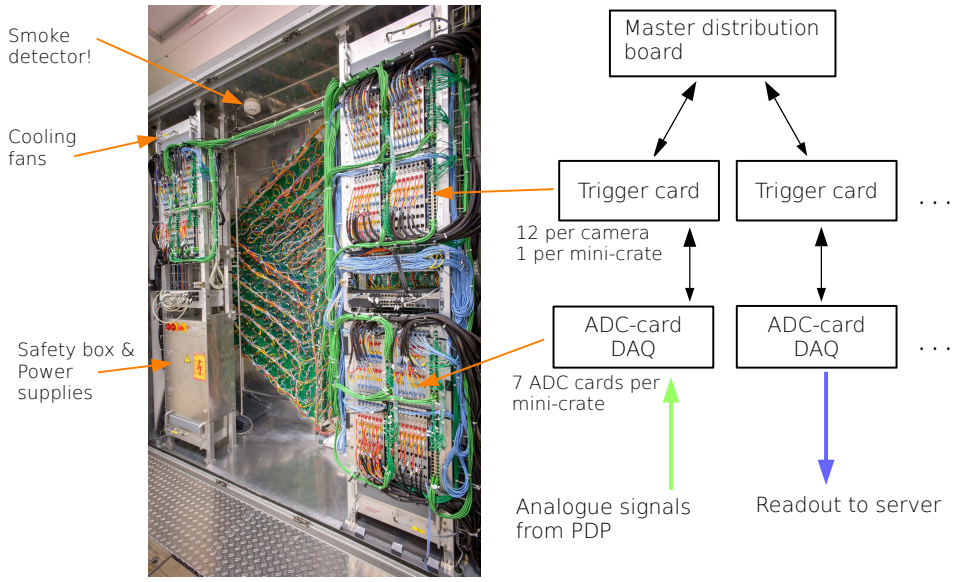

Figure 2.6: Overview of the hierarchical signal chain in FlashCam, demonstrated in hand of the rear of the camera.

DAQ

The final data acquisition is controlled in software running on an external camera server, connected to the readout electronics via four 10 Gbit/s fibre cables, and additional two fibres for the slow control of the individual subcomponents. The DAQ operates on a request based system, checking if the readout electronics have triggered events and transferring the traces of the ADC cards to the server,

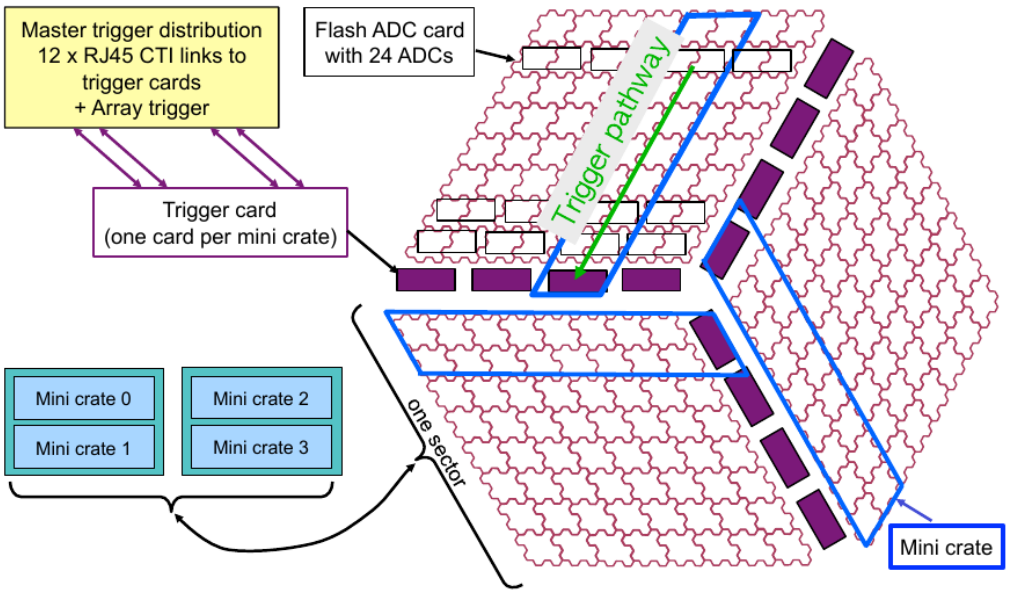

Figure 2.7: Schematic of the FlashCam signal chain. Two PDP modules (12 PMTs each) differentially transmit pre-amplified signals to one ADC card. 7 ADC cards transmit their trigger signals to one trigger card (12 trigger cards, 84 ADC cards), which exchanges the signals with the topological neighbours (due to the PDP and ADC card layout) to form a trigger signal, transmitted to the master trigger distribution card (image from CTA internal technical design report [16]).

where the event building occurs. Additionally the start and stop commands and configuration of the system are set either at the start of the run, or adjusted during runtime (where possible). An example of the read out traces is shown in figure 2.8, while figure 2.9 shows an image of an air shower taken during a testing campaign in Berlin-Adlershof in September 2017, where the FlashCam prototype was mounted on the MST prototype structure.

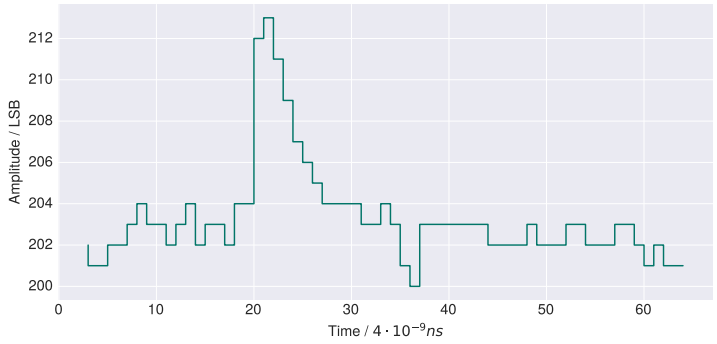

Figure 2.8: Exemplary readout trace of a detected photoelectron.

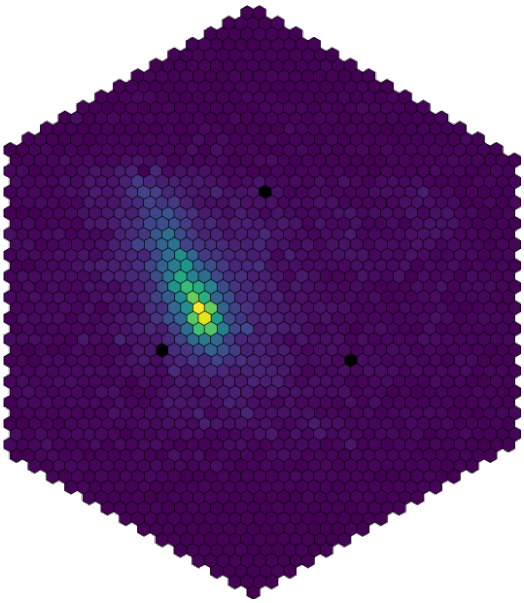

Figure 2.9: Air shower image taken during a testing campaign, where the FlashCam prototype was mounted on the MST prototype structure in Berlin-Adlershof in September, 2017. The upper and lower part of the camera were covered, while the remaining rectangular area was covered with light absorbing foil, to reduce the background light of the night-sky over Berlin to acceptable levels.

2.2 Trigger System

Overview

The FlashCam camera trigger system is designed to be sensitive to the typical Cherenkov emission photons from γ-induced air showers. These signals arrive in a timespan of a few nanoseconds in neighbouring pixels in the camera. The signal amplitude per pixel depends on the energy and impact distances of the primary particle and triggering on signals as small as possible is therefore directly related to the achievable energy detection threshold of the observatory [7].

The detectable images (and their sizes) of air showers in a Cherenkov telescope depend on the energy of the primary and the impact distance. The minimum analysable sizes of these images require a few significant pixels to determine the direction and impact distance of the primary. The design of a trigger algorithm involves therefore correlating the number of detected photoelectrons (PE) in neighbouring pixels and comparison to a threshold. The background against which these signal photoelectrons have to be measured, stems mainly from the night sky, on the order of 10^8-10^9 photoelectrons per second, depending on the pointing of the telescope and the observation conditions.

The trigger logic implemented in the FlashCam camera operates on three different levels of hardware, where each step in the hierarchy is condensing the information of the previous step. The full trigger computation occurs at a continuous rate of 250 MSamples/s. The first level takes place on the ADC cards, which are responsible for the digitisation of the analogue signals from the photon

detection plane modules (PDP modules). Here, an integer differentiation filter is applied (one of four variants implemented in the firmware), and the resulting value subjected to a lower threshold, which passes on the original value if larger than the threshold or 0 if lower. This value is then scaled with a factor S (<1, multiple of $\frac{1}{256}$, minimum 0, maximum $\frac{255}{256}$) and clipped to a maximum value of 85. The next step is a sum of three neighbouring channels to a so called patch sum, of which each ADC card has 8. This matches with the 24 readout channels of the ADC cards (cf. figure 2.10A). The patch sum is then divided by 2 and sent to the next hardware stage, the trigger cards, which are connected to 7 ADC cards via backplane links, as well as their topologically neighbouring trigger cards (cf. figure 2.10B). Each incoming patch sum is then summed up again with the specified neighbouring patch sums to a final trigger sum. The number of neighbouring patches going into the final trigger sum is variable, although fixed for each initialization of the readout system and can be chosen between the local ADC-channel trigger (3-pixels) and up to 6 neighbouring patches (18-pixels), corresponding to the hexagonal pixel layout of FlashCam, resulting in 588 trigger patches in the camera. Due to the inclusion of the neighbouring pixels into the trigger patch sum, the trigger provides an overlapping and homogeneous response across the camera plane.

The final stage is then to compare each of these trigger sums to the trigger threshold. The response of this check is then encoded in a one bit signal from the trigger cards to the master card of the readout system, which responds with the command to the ADCs of transferring the set number of samples from the ring buffer into their event buffer. The final readout of the events from the event buffer is then performed from the readout server. Each of these steps is described in more detail below.

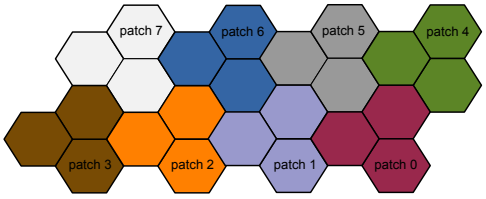

(A) The 24 channels of each ADC module are divided into groups of 3 pixels, resulting in 8 basic trigger patches. These building blocks are summed again into the final master patch sum (588 in the camera).

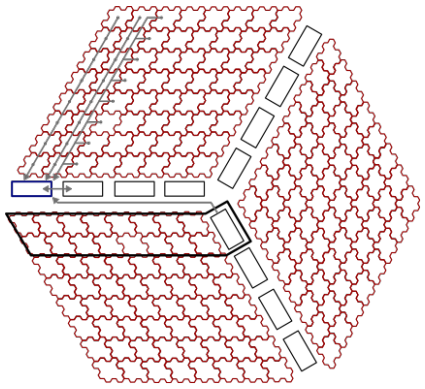

(B) Schematic of the FlashCam PDP modules and trigger cards. ADC cards not shown here, but represented by the two PDP modules connected to each ADC card. Trigger signals of individual ADC cards are transmitted (grey lines) to the trigger cards (rectangular boxes). Exchange of data between trigger cards happens with topological neighbours, depicted by the grey arrows.

Figure 2.10

Digital filter

The first stage of the trigger system applies one of the following differentiating filters to the samples (s_i) of each channel. The differentiating filters shown have been designated by abbreviating the basic operations of addition (p), subtraction (m) and no-operation (o). The explicit equations are given in the follow, but could also be expressed as a convolution operation of the incoming samples with a finite vector (e.g. ppmm corresponds to $\left[+1, +1, -1, -1\right]$).

$$\text{ppmm: } d_i = s_i + s_{i-1} - s_{i-2} - s_{i-3} \tag{2.1}$$

$$\text{ppomm: } d_i = s_i + s_{i-1} - s_{i-3} - s_{i-4} \tag{2.2}$$

$$\text{2pm: } d_i = 2 \cdot \left[s_i - s_{i-1}\right] \tag{2.3}$$

$$\text{2pom: } d_i = 2 \cdot \left[s_i - s_{i-2}\right] \tag{2.4}$$

$$x_i = \begin{cases} d_i \text{ if } d_i \geq 0 \\ 0 \text{ otherwise} \end{cases} \tag{2.5}$$

As the result of the filter is always positive, the filters produce signals from the rising edge of a pulse only. The dynamic ranges of the integer numbers are:

- s_i: 12-bit unsigned (the raw FADC samples)
- d_i: 14-bit signed
- x_i: 13-bit unsigned

This filtering stage is most sensitive on the rising edge of the digitised PMT pulses resulting in a sharpening of the trigger coincidence time between pixels. Additionally this makes the algorithm independent of the baseline, where otherwise a baseline subtracting scheme would have to be used. The current default setting is the `ppmm`-filter, which provides a good trade-off between the `2pm`-filter, which has a larger response to individual pulses, but is also more sensitive to fluctuations, and the sample skipping variants, which have the inverse effect.

The units used for the raw readout traces are LSB (least significant bit), representing the minimum change in signal voltage to increase the output of the analogue-to-digital converters (ADCs) by one bit.

Lower threshold

This threshold looks for a minimum contribution to the sum and can be adjusted for all channels individually:

$$y_i = \begin{cases} x_i & \text{for } A_i = 1 \\ x_i & \text{for } A_i > 1 \text{ and } \lfloor \frac{x_i}{2} \rfloor \geq A_i \\ 0 & \text{otherwise} \end{cases} \tag{2.6}$$

The dynamic range of y_i is 13-bit. The default lower threshold is $A_i = 1$.

Scaling and clipping

The scaling reduces the dynamic range of the signals and can be adjusted for each channel individually. After scaling by a factor S_i, the signals get clipped to a maximum value of 85, providing an upper limit to the contribution of each channel to the sum. This clipping limits the influence of afterpulses to the trigger.

$$z_i = \min\left(85, \left\lfloor \frac{\lfloor y_i \cdot S_i \rfloor}{256} \right\rfloor\right) \text{ for } S_i \in \left[0, 255\right], S_i \in \mathbb{N} \tag{2.7}$$

The dynamic range of z_i is 7-bit.

Summation and trigger decision

The z_i of three (next) neighbouring channels are summed to a patch signal (1764 pixels $\rightarrow$ 588 non-overlapping patches).

$$p_l = \sum_{i \in L_l} z_i \text{ with } L_l \text{ sets of trace indices of one patch} \tag{2.8}$$

The effective range of the resulting p_l is $3 \cdot 85 = 255$ (8-bit).

Each patch signal gets further divided by 2 such that the effective range is $[0, 127]$ (7-bit), which allows the board-to-board links (backplane or cables) to use 1 parity bit to detect single-bit transmission errors.

These patch signals are then summed with an adjustable number of (next) neighbouring patch signals to a master patch sum, resulting in 588 overlapping master patches in the camera:

$$m_k = \sum_{l \in K^k} \left\lfloor \frac{p_l}{2} \right\rfloor \text{ for } K_k \text{ sets of patch indices} \tag{2.9}$$

The default master patch size is 3 next neighbouring patches, corresponding to 9 pixels. The sums of all combinations of neighbouring patches (i.e., all possible master patch sums) are computed and are able to trigger the camera if they exceed the trigger threshold T:

$$\text{camera trigger if } m_k > T \quad \forall\, k \tag{2.10}$$

The readout window of a triggered event then begins at a configurable offset relative to the triggered sample. The length of the readout window is configurable. Should a trigger occur within a configurable portion of a readout window (e.g., within the last N samples), the camera will re-trigger and construct a second, consecutive event, effectively extending the first event.

C-implementation of the trigger logic: FCTriggerSim

The fact that the FlashCam trigger is purely digital (implemented in the firmware) offers the opportunity to cross-check the camera trigger behaviour by implementing the same logic in a programming language of choice, which has been done in the context of the FlashCam analysis and operation framework (`fc-utils`). Instead of running the camera in the self-triggered operation, the system can be set to trigger the readout externally and then compute the trigger response of the system by analysing the event traces offline (e.g on the MPIK computing cluster) and get the exact same response the camera would have computed. Especially in trigger threshold regimes, where the expected trigger rate is very low, this speeds up the *measuring* process, as the externally-triggered measured data must only be recorded once, allowing to compute the response of the trigger system with various trigger settings offline, while the self-triggered camera measurement must be done sequentially.

The set of programs and libraries of `fc-utils` is implemented in the C programming language, and the trigger logic has been implemented as a sub-library named `FCTriggerSim`. An unoptimised reference implementation of the trigger logic is detailed in appendix A. The default implementation makes use of the AVX instruction set [33] and the OpenMP [50] multi-threading library. Compared to the processing power of the 97 parallel FPGAs used in the camera, the analysis on a multicore server is orders of magnitude slower. The processing speed of FCTriggerSim has been tested for a single set of trigger settings and an event size of 3900 samples using a 40-core server, resulting in an estimated ~ 230 kSamples/s (~ 60 events/s). When increasing the number of trigger settings to 32 combinations of the filter, scaling and patch-size parameter, and 889 trigger threshold, the speed drops to ~ 0.2 events/s allowing the analysis of a dataset of 10,000 events in ~ 14 h.

In this work, this library has been used to compute accidental trigger rates due to night-sky background as well as trigger response and trigger efficiency curves due to additional pulsed laser emission emulating the Cherenkov image light. As the simulation package `sim_telarray` provides the output of the simulations also as raw traces, `FCTriggerSim` can be used input-agnostic, although a conversion of the data formats has to take place.

2.3 FlashCam Prototype - laboratory set-up

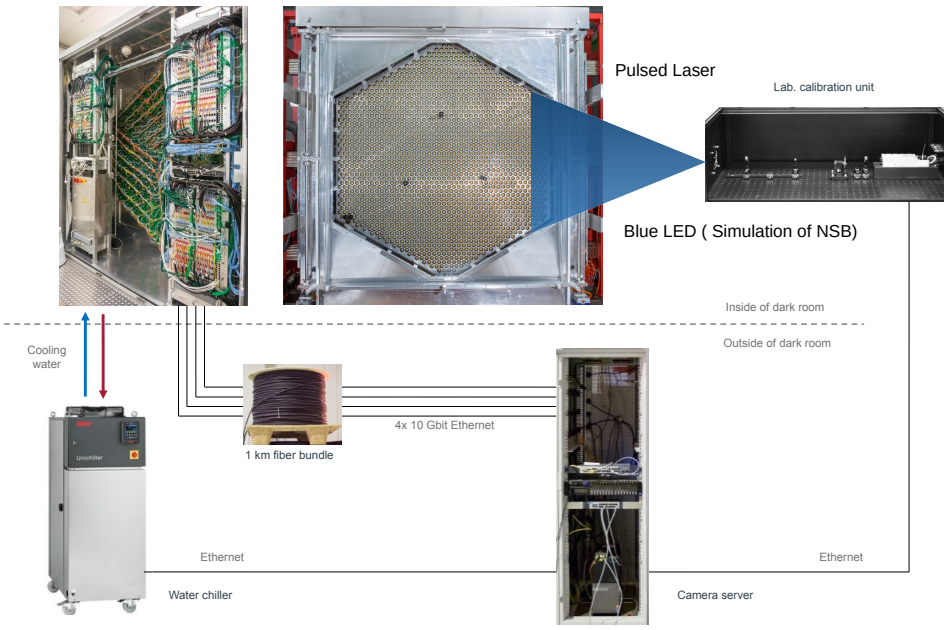

Figure 2.11: Laboratory set-up used for data taking with the FlashCam prototype camera. The camera was mounted on a dedicated frame, with a calibration unit mounted 4.25 m in front of the centre of the camera. The readout- and control server was set up outside of the dark room, connected to the camera via 1 km long fibre bundles, emulating the set-up of the live operation. A water chiller unit was attached to via flexible tubes, providing the needed cooling.

The FlashCam prototype camera was mounted in a dark room at MPIK, where the performance tests and the measurements of various camera and subcomponent characteristics took place. The calibration unit provided an LED emulating continuous night-sky background light and a pulsed laser unit emulating the short and faint Cherenkov flashes of air showers. A server installed outside the dark room was connected via fibre to the camera, and responsible for the control and readout of the camera and control of both light sources.

The laser unit (~ 300 ps FWHM of light pulse width and peak wavelength emission at 355 nm) is able to flash light with a rate of up to 1.5 kHz, while the intensity of the light flashes can be set with an attenuating filter wheel in-between the laser and the diffuser (at the output of the calibration unit).

It also provides a electrical reference pulse output, which was connected to the camera readout system on a spare readout channel. This allowed taking data with the camera by triggering on the reference pulse, instead of PMT traces itself. This reference pulse was duplicated four times, with a phase shift of 1 ns between each channel and also a pulse height much larger than the usual pulse response from single or multi photoelectron signals from the laser flashes, providing a stable

timing reference for the charge reconstruction and the analysis of the trigger signals.

The datasets used in this work were taken during a few data taking campaigns, were the dark room had been carefully prepared and checked for light tightness, as well as tracking down unexpected sources of faint background light emitted from inside the dark room. Additionally the system was turned on a few hours before the actual data taking, monitoring the temperature of the components until a stable equilibrium had been reached, thereby minimising the influence of the temperature drifts during the warm-up phase.

2.4 Calibration

The procedure The later trigger verification studies rely on an accurate model and calibration of the signal chain. The FlashCam flat-fielding scheme determines the high-voltage settings and the gain of the individual pixels through photon statistics. The following equation shows the relation used.

$$G_{\text{upsampled}} = \frac{\text{Var}[N_{PE}]}{< N_{PE} > \cdot \text{ENF}} = \frac{\text{Var}[S] - \text{Var}[B]}{(< S > - < B >) \cdot \text{ENF}} \tag{2.11}$$

The number of detected photoelectrons (S) is determined with a peak search of the upsampled trace in an interval of ± 1 ns, around the time the incident laser pulse is expected, while the background (B) is the amplitude measured at a fixed offset before the signal sample. The application of equation 2.11 depends on the knowledge of the excess noise factor of each PMT, which is set to 1.289.

In practice, the FlashCam flat-fielding has been modified to set the gains in such a way, that the response of the trigger signals is uniform across the camera. As the trigger filter response is dependent on the pulse-shape of each PMT, the algorithm calculates the `trigger_loss` factor for each channel and computes the trigger gain from the signal gain as follows:

$$\text{trigger\_loss} = \frac{< T_s > - < T_b >}{< S > - < B >} \tag{2.12}$$

$$G_{\text{trigger}} = \text{trigger\_loss} \cdot G \tag{2.13}$$

with T_s the signal after application of the `ppmm`-filter to the raw trace and T_b the trigger amplitude with the same offset as in the gain determination. This modification ensures that the final trigger sums take the output of each constituent channel with the same weight into account. A consequence of this modification is, that the signal gains of the channels must not be on the same level, as can be seen in figure 2.12, where the dotted lines show the median gain coefficients of the 7- and 8-dynode PMTs. The faster rise time of the 7-dynode PMTs leads to a larger response of the `ppmm`-filter than the response of the 8-dynode PMTs and in turn the gain is lower by $\sim 5\%$ on average. This difference in signal gain

is taken into account in reconstruction of Cherenkov signals, but improves the trigger uniformity of the camera.

Measurements In the laboratory the laser has been used to illuminate the camera with pulsed flashes with fixed intensity at ~30 PE, while adjusting the high-voltage settings of the individual pixels until the target trigger gain has been reached (within 1%). The procedure was performed with very low levels of background illumination (~ MHz PE), taking a known effect into account, where a slight increase in the gain occurs without any background illumination. Figure 2.12 and 2.13 provide a reference of this calibration as horizontal lines and are name "online".

Cross-checks have also been performed by applying the calibration procedure to datasets taken under similar conditions, although different levels of background illumination (0 and 417 MHz PE), which differ by a few percent due to the background dependence of the PMT gain and measurement biases.

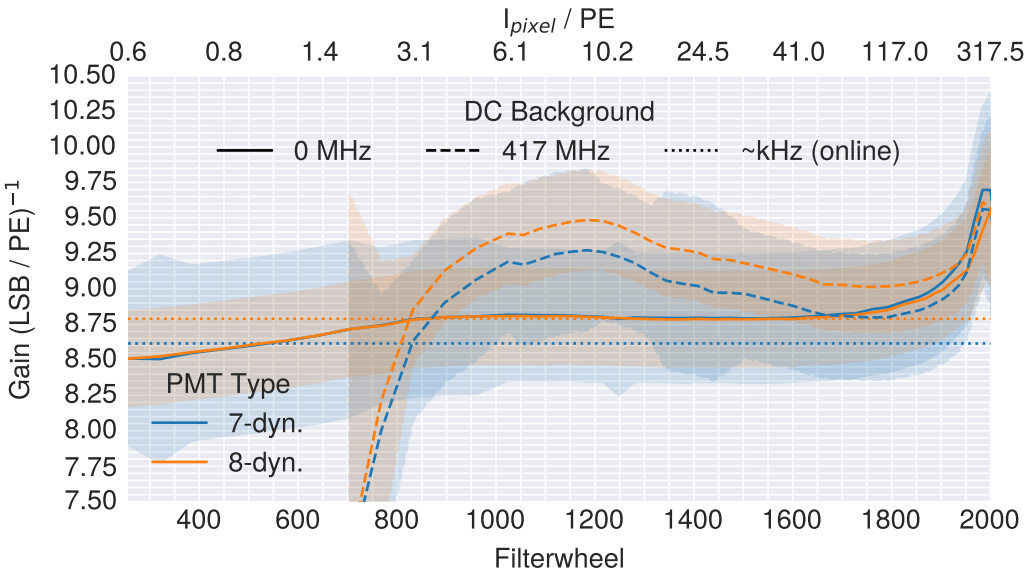

Figure 2.12: Comparison of gain coefficients determined from datasets taken at 0 MHz (solid lines) and 417 MHz (dashed lines) with fixed high-voltage (HV) settings. Also shown are the gain coefficients determined online while adjusting the HV settings to reach the desired gain (dotted horizontal lines for reference) at a fixed laser intensity. The shaded regions show the standard deviation over all pixels in the camera.

Simulations The pulse height of individual photoelectrons in the simulation software sim_telarray is determined by the gain input value (`fadc_amplitude`) and scales the normalised pulse shape, which is given as a high-resolution time series in tabular form. A random sample is drawn from the the single-photoelectron spectrum to determine the PMT response and the corresponding sampling phase aligned pulse shape is added to the readout trace, taking an additional random transit-time jitter into account. Since only the peak of the fine-resolution tabulated

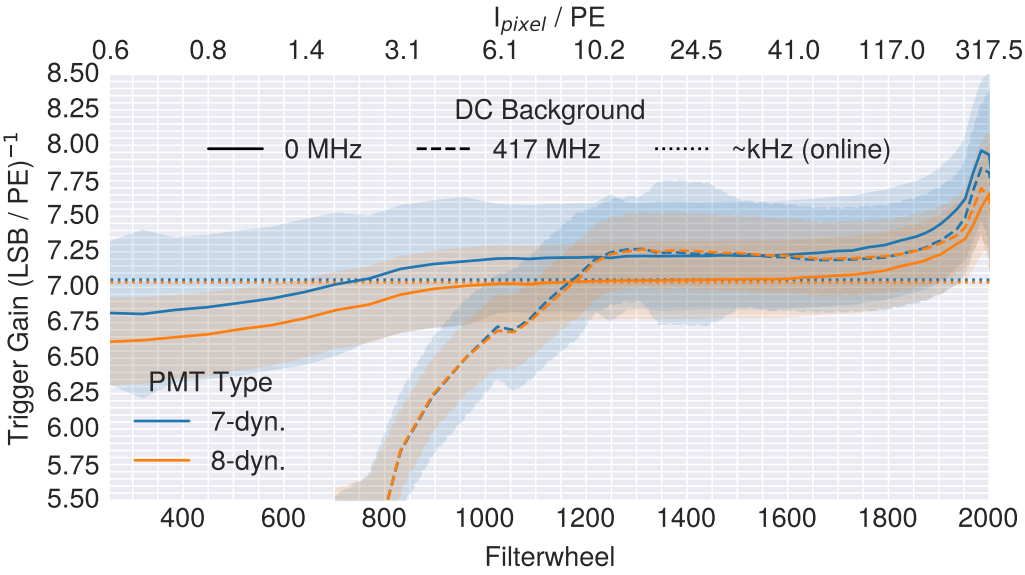

Figure 2.13: Comparison of trigger gain coefficients determined from datasets taken at 0 MHz (solid lines) and 417 MHz (dashed lines) with fixed high-voltage settings. The dotted lines show the trigger gain determined during the online calibration run at a fixed laser intensity. The shaded regions show the standard deviation over all pixels in the camera.

pulse shape is normalised, the (coarse) sampling will (for nearly all values of phase offset) lead to smaller pulses. This leads to an average loss (`sampling_loss`) compared to the `fadc_amplitude`, when analysing the simulated raw readout traces.

Additionally, the reconstruction method used in the calibration procedure uses the upsampled raw traces for the charge estimation, which has also has an associated loss factor (`upsampling_loss`) and the differentiation filter with the `trigger_loss`. These various loss factors are dependent on the actual PMT pulse shape and have been calculated from the pulse shape parameters (cf. figure 2.17 in section 2.5).

$$G_{\text{raw}} = \texttt{sampling\_loss} \cdot \texttt{fadc\_amplitude} \tag{2.14}$$

$$G_{\text{upsampled}} = \texttt{upsampling\_loss} \cdot G_{\text{raw}} \tag{2.15}$$

$$G_{\text{trigger}} = \texttt{trigger\_loss} \cdot G_{\text{raw}} \tag{2.16}$$

To verify the Monte-Carlo description of the parameters, the simulated data has been subjected to the same calibration scheme as the camera data and the `fadc_amplitude` input parameter has been adjusted according to the pulse shape dependent sampling and upsampling losses. The result using datasets with comparable background illumination and relevant range of simulated laser illumination are shown in figure 2.14. The trigger gain shows an good agreement within 1 % compared to the measured datasets (I_{pixel} range 30-40 PE), while the signal

7-dynode PMT		8-dynode PMT	
NSB [GHz PE]	gain corr.	NSB [GHz PE]	gain corr.
0.4234	1.0038	0.4078	1.0057
0.8434	1.0076	0.8126	1.0115
1.3883	1.0127	1.3364	1.0191
2.0554	1.0188	1.9766	1.0285
2.7148	1.0250	2.6084	1.0379
4.0036	1.0374	3.8612	1.0571

Table 2.1: Background illumination dependent gain correction factors for the 7- and 8-dynode PMTs.

gain has a larger offset of $\sim 3\,\%$. Additionally, the further simulation need to take a dependence of the PMT gain on the level of background illumination into account, where the corresponding scaling factors are given in table 2.1 (not taken into account in fig. 2.14).

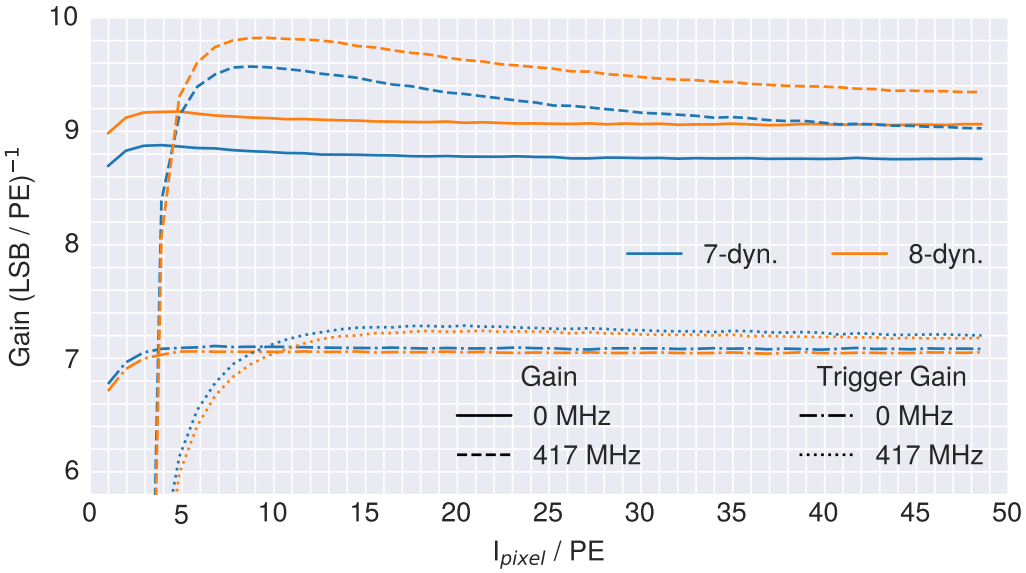

Figure 2.14: Comparison of the gain and trigger gain of the sim_telarray simulations, obtained by applying the same algorithm to the simulation as to the measured data.

Trigger signal calibration The equation used to apply the gain calibration of the master trigger patch trigger signals is given here.

$$T_{\mathrm{PE}} = (0.5 + 0.25\, n_{\mathrm{pixel}} + T_{\mathrm{TLSB}})\, \frac{256}{S}\, \frac{2}{G_{\mathrm{trigger}}} \tag{2.17}$$

T_{TLSB} is the sample wise trigger amplitude in the master trigger patches in hardware units (TLSB) and offset with an additional value dependent in the number of pixels in the trigger sum. This takes digitisation effects into account (see section 3.4.4). The factor $256/S$ compensates for the scaling under the assumption,

that the same scale factor S has been applied to all channels, while the factor of 2 corrects the division before the 3-pixel trigger patch sums are sent to the trigger cards. The trigger gain G_{trigger} is either taken from the calibration itself, or can be calculated according to eq. 2.16 from the simulation input parameters (`fadc_amplitude` and pulse shape responses).

2.5 Simulation configurations

Three major adjustments to the simulation configuration in `sim_telarray` have been made, which involved the measurement and analysis of PMT characteristics, namely the afterpulsing spectrum, the pulse shape and the single-photoelectron spectrum. The afterpulsing behaviour of the 7- and 8-dynode PMTs was analysed by Stefan Eschbach [15].

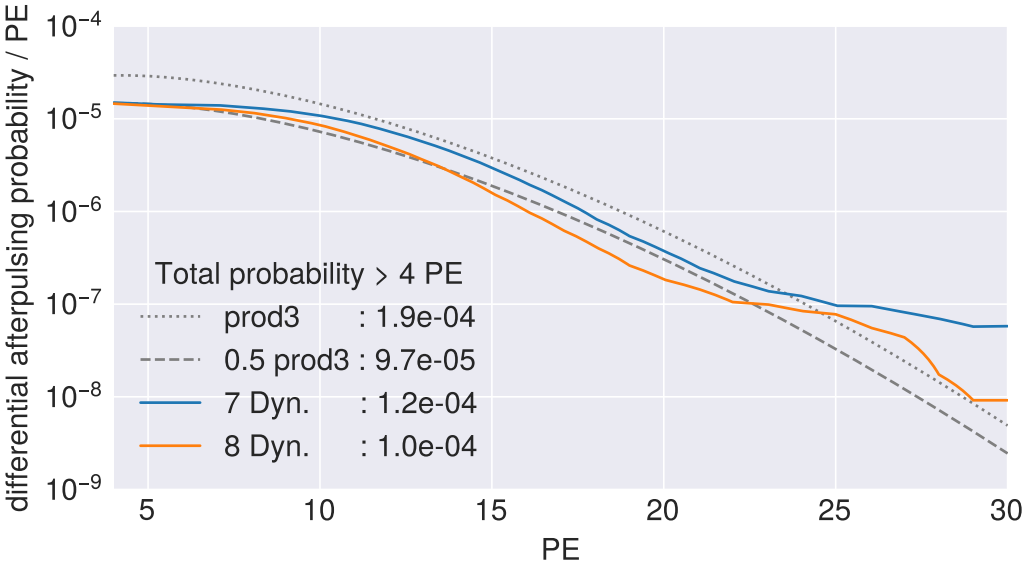

Figure 2.15: The measured differential afterpulsing probability of the 7- and 8-dynode PMTs used in the FlashCam prototype. The grey dashed line shows the afterpulsing spectrum previously used as the simulation input parameter up to the third large-scale CTA simulations ("`prod3`". The dashed line shows the same spectrum scaled by half, providing a placeholder for the later updated (measured) configurations.

PMT after pulsing The type of afterpulse, that is most influential on the camera trigger rate, is generated from photoelectrons ionising residual gases inside the PMT cavity. These positively charged ions travel back to the photocathode, inducing additional photo electrons, which traverse the PMT amplification process producing a voltage signal, similar to that of multiple signal photoelectrons, with a delay (with respect to the original photoelectron) of a few hundred nanoseconds (up to microseconds), depending on the mass-to-charge ratio of the ion and the high-voltage between the photocathode and the first dynode of the PMT. This

process is therefore most relevant for the background camera trigger rate estimation (induced by night-sky background photons), where the continuous stream of incoming photons produces a constant rate of afterpulses. The Cherenkov signals are mostly unaffected due to their short arrival-time interval.

The differential afterpulsing probabilities of one incoming photoelectron producing an afterpulse are presented in figure 2.15. The figure shows the afterpulsing spectrum between 4 PE and a maximum charge of 30 PE, which has been extracted as a median afterpulsing spectrum for each PMT type from the analysis results of a larger set of original afterpulsing measurements. Also displayed is the original afterpulsing spectrum used in the simulations in the full CTA simulation productions (up to `prod3`) (labelled "prod3" in figure 2.15). The integrated probability for the new measurements of the 7- and 8-dynode PMT afterpulsing is $\sim 10^{-4}$, approximately a factor of 2 smaller than initially estimated. The version labelled "0.5 prod3" in figure 2.15 represents an artificial configuration used in the simulations in this work, where the influence of the afterpulsing on the camera trigger rates had been studied by scaling the "default" spectrum . The simulations using the "0.5 prod3" version had been found to agree better with measurements and used as a proxy until the full analysis of afterpulsing measurements had been completed (see section 3.4.6).

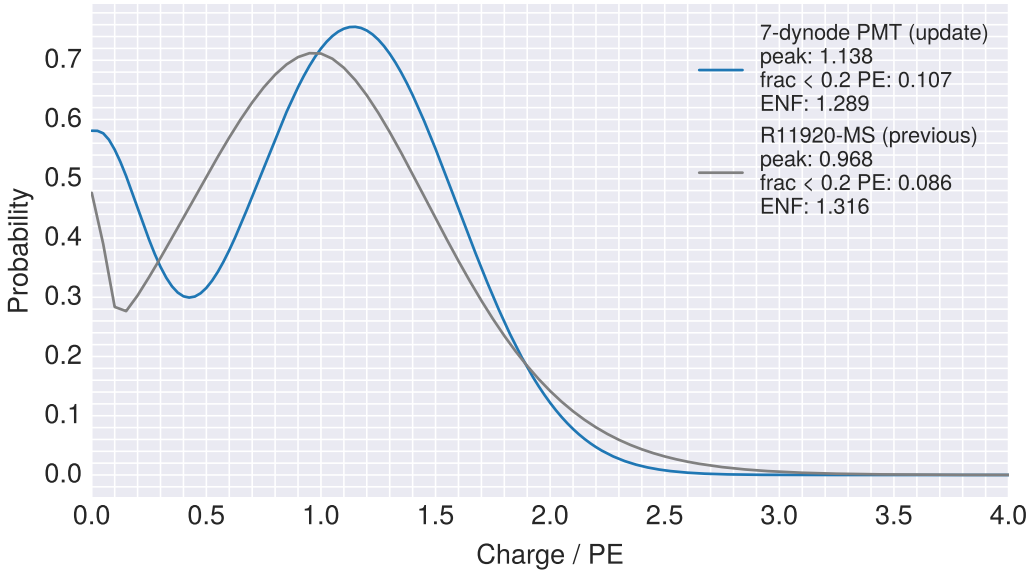

Figure 2.16: The measured single photoelectron spectrum of a 7-dynode PMT. The updated simulation configuration is shown in blue, while the previous spectrum used is shown in grey. The mean of the distributions is used to provide the conversion of 1 PE to hardware units in the simulations (`fadc_amplitude`-parameter in `sim_telarray`).

PMT single photoelectron spectrum The updated configuration file for the simulations has been extracted from measurements of the single photoelectron spectrum (SPE spectrum) of a 7-dynode PMT, equipped with a pinhole-mask

in front of the photocathode, reducing the intensity of the incoming light. The measurement was performed then using the laser of the calibration unit, setting the filter wheel to a an attenuation level such that the mean photoelectron charge per pulse detected by the masked PMT was on the order of ~ 0.1 PE, reducing the probability of detecting ≥ 2 PE per event to $\sim 10^{-4}$. The high-voltage was set to 1400 V instead of the normal operation voltage (~ 900 - 1000 V), increasing the signal-to-noise ratio. The excess noise due to the amplification chain of the dynode stages of the PMT is dominated by the amplification of the first stage (1st dynode). The PMTs used in FlashCam operate with a fixed voltage between the cathode and the first dynode, which minimises the change in the excess noise between normal operation and this measurement. The resulting dataset consists of $60 \cdot 10^6$ events and the analysis evaluated the amplitude of the pulses at a fixed position relative to the laser reference pulse.

The excess noise factor given in figure 2.16 is calculated with $\sqrt{1+\sigma^2}$ (σ the standard deviation of shown the distribution).

The calibration of the conversion factors, i.e. conversion of digitised hardware units (LSB) into photoelectrons is sometimes performed by measuring the single photoelectron spectrum and using the mean or the most probable value as the fixed point to determine the calibration of the charge reconstruction. For FlashCam the calibration is done using photon statistics in the ~ 30 PE intensity regime by adjusting the high-voltage until a target gain conversion (LSB to PE) is reached (see section 2.4)) and relies on the excess noise factor which has been extracted from the shown distribution (for this work).

The influence of the updated single photoelectron spectrum on the night-sky background camera trigger rates is discussed later in section 3.4.7.

PMT pulse shape The pulse shape previously used in the `sim_telarray` simulations has been updated with separate version for the 7- and 8-dynode PMT configurations. The pulse shapes have been extracted from a dataset, which has been produced by flashing the camera with the laser pulses, resulting in a mean charge of ~ 120 PE per pulse and pixel. The individual events were then phase aligned by using the centroid of the reference pulse (on which the camera was triggering). The raw readout traces were then sorted into a fine-binned histogram (0.1 ns bin width) and the median value for each time-bin was extracted, resulting in shape for each pixel. The normalised reference pulse shapes used in the simulation configurations have been picked from these extracted pulse shapes and are presented in figure 2.17A and 2.17B for the 7-dynode and 8-dynode PMTs respectively.

One of the major factors in understanding the trigger system, is the form of the single photoelectron pulse response (the pulse shape) of the photomultiplier tubes. The charge reconstruction used in the reconstruction chain of FlashCam traces involves an upsampling and smoothing step and then a pole-zero correction

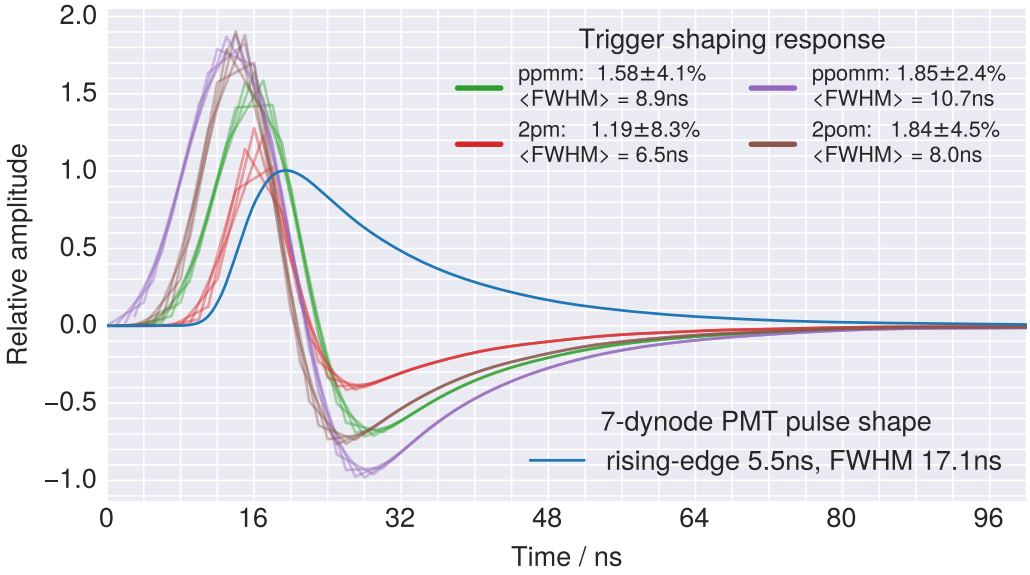

(A) The reference pulse shape of the 7-dynode PMT used in the simulations (blue line).

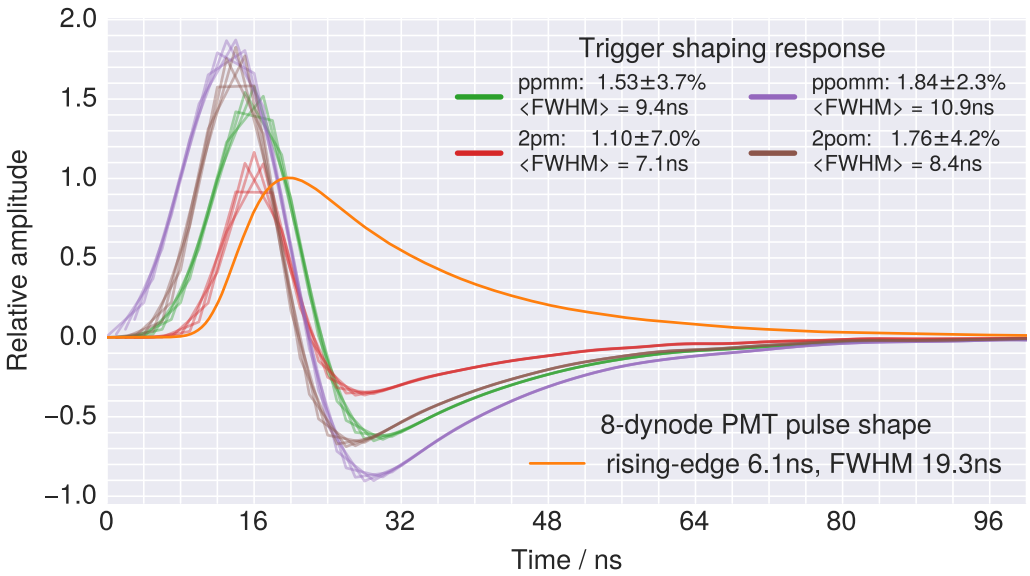

(B) The reference pulse shape of the 8-dynode PMT used in the simulations (orange line).

Figure 2.17: Panel (A) and (B) display the 7- and 8-dynode PMT pulse shapes used in the `sim_telarray` simulations of the camera. Also shown are 4 exemplary trigger response shapes (of the 40 possible) for each trigger filter. The overall trigger amplitude response resolution of the 7-dynode PMT is worse than the 8-dynode variant, while the width of the 7-dynode is smaller. This is a direct consequence of the shorter rising-edge of the 7-dynode PMT pulse shape.

of the raw traces, thereby increasing the resolution of the reconstructed charge, as well as the time resolution. This procedure is unfortunately too processing-heavy to be implemented in the current FlashCam ADC boards, so a simplified approach has been taken, by using a differentiation filter. The response of these filter is shown in figure 2.17, by applying the filters to the reference pulse shapes of both PMT types. The reference pulse shapes are given in units of 0.1 ns, providing

an oversampling of 40, compared to the sampling rate of the readout system itself (4 ns/sample).

Each filter has its the advantages and disadvantages, where the trade-off between a better amplitude resolution and a wider pulse shape (larger overlap with neighbouring samples) has to be made.

The `2pm` and `2pom` filters are both purely differentiating filters, with the difference being the no-operation sample for the latter filter. While the 2-sample wide variant provides a sharper response to the rising edge of the original pulse, the 3-sample wide variant provides an overall larger response and less variance in the resulting amplitudes, due to the larger overlap with the minimum and maximum values of the rising-edge of the original pulse. The `ppmm` and `ppomm` filters take 2 samples for each addition and subtraction operation into account, providing an additional running average (smoothing) of the neighbouring samples, resulting in a better amplitude resolution than the 2-sample variants. This additional smoothing makes both filters more resilient towards additional fluctuations, e.g. electronic noise, which are not included in figure 2.17.

The absolute response of the filter is of minor importance, as the scaling step in the trigger chain makes adjusting the trigger filter responses possible. Taking into account the mentioned effects, the `ppmm` has been chosen as the default for later operation.

Chapter 3

Trigger Verification

Characterising the trigger behaviour and performance of the FlashCam prototype is a crucial task before the eventual deployment of the camera in the field. The trigger system operates as a fully-digital system on the raw readout traces and behaves like a fast signal reconstruction system. Compared to previous generations of Cherenkov cameras, this digital approach provides multiple advantages:

- The input to the trigger is recorded and can be re-analysed using software.
- The trigger is based on the well-understood signal path used in the "normal" event reconstruction.
- The behaviour (through the trigger settings) can be reconfigured consistently for all readout channels and trigger patches. This is in principle possible during runtime.
- The detector simulations can implement the same trigger logic as the firmware, giving precisely the same response.

These facts provides the unique opportunity to cross-check the expected behaviour of the camera, using the software implementation of the trigger logic. Additionally, the output of the photomultiplier tubes (PMTs) which make up the photon detection modules of the FlashCam camera need to be understood for both the reconstruction- and trigger signal processing chain characterisation. An equally important task, which is closely connected to the characterisation of the trigger system, is reaching an adequate description of the camera with the full Monte-Carlo simulation chain. The software used in CTA and by the FlashCam team is the `sim_telarray` package [8], which provides a full telescope array simulation, starting with the cherenkov photons emitted from air showers, the detection of these photons by the telescope and the camera and the full processing of the photon detectors, the analogue to digital conversion of the PMT pulses, the triggering and the final readout. The unavoidable background light from the night sky and stray light, is also taken into account in all simulated readout.

An important part of this work has been to provide and verify updated configuration parameters for `sim_telarray`. The verification has been carried out by simulating the measurement set-ups as close as possible.

3.1 Bias and resolution of the trigger path

The signal path of the trigger system is based on raw traces sampled by the ADC boards and read out by the data acquisition (DAQ). In this sense, the trigger is just a specific way to analyse the samples, matched to the restrictions imposed by the FPGA. Due to the trigger patch summing, the trigger acts as a coarse grained observation of the light intensities in those pixel-sums. To compare both these signal paths, multiple dataset have been taken with different laser intensity and levels of background illumination. The charge reconstruction in the event reconstruction has been performed by using the peak of the pedestal subtracted and upsampled traces, then applying the pixel-wise gain calibration coefficients and summing up the charges from the pixels in each trigger patch (in this analysis the 9-pixel trigger patches have been chosen). This provides an estimate value of the light intensity in each master trigger patch. The same data has been passed through the FCTriggerSim framework producing the trigger signals, as the camera hardware would produce. These trigger signals have been extracted by searching for the peak maximum in an interval of 3 samples around the expected sample position in the trigger traces. The conversion from hardware units (TLSB) to reconstructed photoelectrons uses equation 2.17 with trigger gains applied as the mean of the pixel-wise trigger gains for each trigger patch.

The results of this analysis are shown in Figure 3.1. The relative bias of the trigger signals (T) and mean reconstructed photoelectrons ($\langle I_{9pix} \rangle$) is shown for increasing laser intensities and for 0, 417 and 1383 GHz,PE pixel background light illumination. Additionally the error bars show the standard deviation of the ratio over the all master trigger patches populated with either pure 7- or 8-dynode PMTs.

The increase of the relative bias in figure 3.1 for lower intensities is due to the zero-truncation after the differentiation stage of the trigger, producing only positive signals, while the charge reconstruction is still sensitive to downward fluctuations of the background. This bias sets in at higher light intensities for higher background illuminations. The drop of the ratio with higher intensities is due to the difference in range of possible values between the trigger traces and readout traces. The 9-pixel sum may have a maximum value of 381 LSB, which converts to $\sim$330 PE for the used trigger settings (scaling parameter of 42) and trigger gain settings of the PMTs ($\sim$7.0 LSB). Defining a maximum value for normal signals is not as straightforward, as the digitised signals exhibit a non-linear response above a certain pulse height, which sets in at around 100-120 PE per pixel. In any case, this is beyond the clipping range of the trigger signals, leading to the expectation that the values of $\langle I_{9pix} \rangle$ are linear in the shown ranges. Due to the Poissonian nature of background illumination, the deviation from a value of one of the relative bias is expected to set in earlier with higher NSB levels, as the distribution of the trigger signals close to the maximum value is skewed

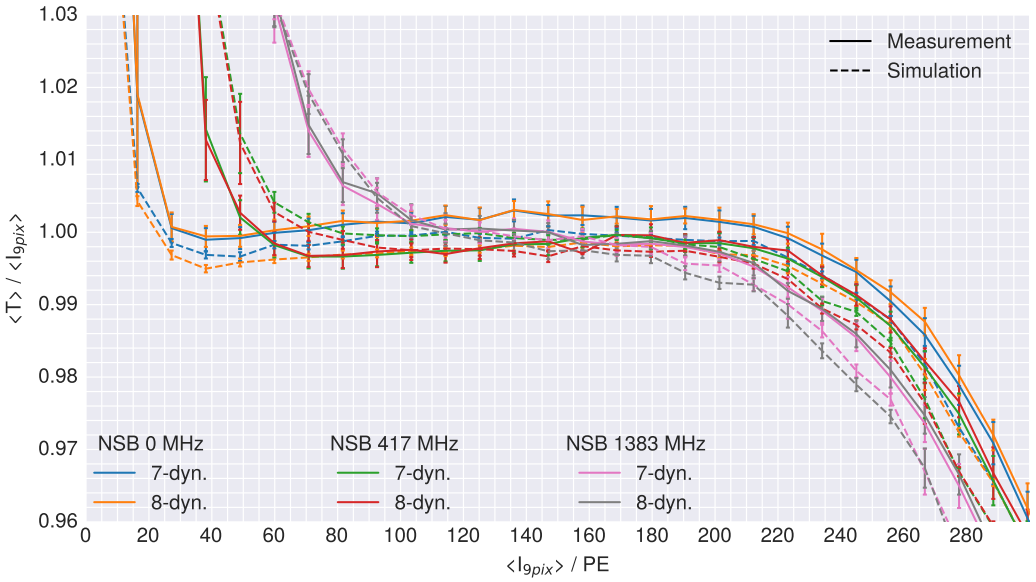

Figure 3.1: The relative bias between the reconstructed charge per laser flash, between the normal signal reconstruction $\langle I_{9pix} \rangle$ and the trigger signal reconstruction T. The solid lines show the results from the laboratory measurements, while the dashed lines show the simulations of the same set-up. Separate results are shown for trigger patches, where all contained pixels are of the same PMT type (7- or 8-dynodes) and for three sets of background illumination. The error bars give the standard deviation of the relative bias for all fully-equipped master trigger patches in the camera.

due to the truncation of the amplitudes. This behaviour can be seen in the top row of figure 3.2 where the excess noise figures of the signals and trigger signals are compared. The excess noise factor (ENF) is calculated as follows:

$$\mathrm{ENF} = \frac{\langle (I - \langle I_{9\mathrm{pix}} \rangle)^2 \rangle}{\langle I_{9\mathrm{pix}} \rangle} \tag{3.1}$$

where $I = I_{9\mathrm{pix}}$ or $I = T$ for the reconstructed charges and trigger signals respectively. Taking the square root of the ENF would result in the relative resolution of both signal types. The trigger signals experience are compressed due to the trigger signal truncation (close to the maximum), which reduces the variance of the trigger signal distribution. This quenching sets in at the intensity where the bias due to the truncation starts to set in (upper and lower left panel of figure 3.2). As the laser intensity increases beyond the range of the possible trigger signals, the resolution (and the ENF) continuously worsens relative to the absolute difference.

Note on signal and trigger resolution To understand the behaviour of the trigger and signal resolution in figure 3.2 one needs to dissect a few dominant contributions to the total noise, which depend on the signal shaping and reconstruction methods used in both paths. The different components relevant here are shown

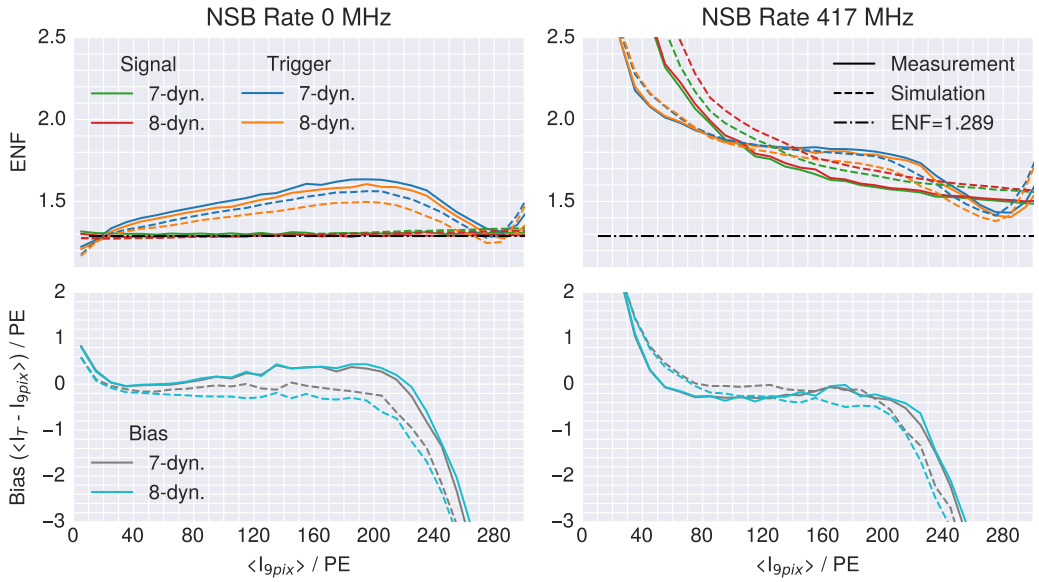

Figure 3.2: The upper two plots show the excess noise (ENF) for the signal and trigger signal measurements and simulations. The dash-dotted line shows the expected limit due to poissonian statistics and the excess noise factor of the PMTs as reference.

in the following equation:

$$\sigma^2_{\text{total}} = N_{\text{PE}} \cdot \text{ENF} + \sigma^2_{\text{el.}} + f_{\text{NSB}} \cdot \tau_i + (a_i \cdot N_{\text{PE}})^2 \tag{3.2}$$

The first contribution originates from the usual poisson statistics (incoming photons) increased with the excess noise factor of the PMT. The electronic noise is listed here, but is mostly negligible (on the order of 0.1 PE). The noise from the background illumination depends on effective integration width of the pulses. The effective width of the upsampled pulse shape is wider than the effective width of the trigger signal (which is using the differentiating `ppmm`-filter). This results in a larger $\sigma_{\text{NSB}} = \sqrt{f_{\text{NSB}} \cdot \tau_i}$ for the charge reconstruction versus the trigger signal reconstruction. In other words, the probability to pile-up background photoelectrons with signal photoelectrons is larger for wider pulse shapes (for fixed background rates). On the other hand, a differentiated signal is more sensitive to changes to the phase between sampling time and arrival time (a small shift in arrival time versus sampling time results in a larger amplitude difference). This means for larger input pulses (more photoelectrons arriving at the same time), this uncertainty on the amplitude increases also. This is often called phase error and reflected in the last term $a_i \cdot N_{\text{PE}}$, with i depending on shape of the reconstructed pulse. One can observe this effect in the top-left panel of figure 3.2, where the trigger resolution gets worse with increasing intensity, while the signal resolution stays close to the expected ENF value of 1.289. In the top-right panel, the measurement is shown with an NSB rate of 417 MHz PE, where the trigger resolution is better for low intensities, but crosses the signal resolution while increasing the

laser intensity, until the clipping point of the trigger is reached.

3.1.1 Discussion and comparison to simulations

The 7- and 8-dynode pixels have been simulated with separate full camera simulations, and otherwise same set-up as the measurements, taking pixel-wise NSB levels and gain corrections into account. The results are shown as separate lines in figures 3.1 and 3.2. Both simulations and measurements have a relative bias <1% between reconstructed charge and trigger signals in the range with sufficient signal-to-noise and below the truncation regime. The bias curves show an excellent agreement between simulations and measurements within 1% in the same regime, with deviations <2% otherwise. The homogeneity of the trigger reconstruction of across all fully-equipped master trigger patches (patches at the edges may only have 3 or 9 pixels) is shown to be within 1%. The residual differences can be attributed to the remaining systematic uncertainty on the understanding of the PMT parameters and the NSB values used in the simulations. As the trigger gain and the gain are dependent on each other, a change in the gain parameter in the simulations also influences background due to the effective integration width of the individual pulses, which translates to a shift of the simulated curves to the left or the right in figure 3.1.

3.1.2 Influence of the scaling parameter

The fact, that the trigger algorithm is implemented in integer arithmetics subjects each step of the computation to truncation effects. The application of the trigger gain coefficients and the back-calculation using equation 2.17 takes the truncation effects of some of the division operations into account by adding an average offset. A smaller effect still remains, which depends on the value of the scaling factor S, as well as the actual trigger pulse height in hardware units (TLSB).

Figure 3.3 shows the results of a scan of the scaling parameter for 4 levels of measured laser intensity with no background illumination. The displayed curves are obtained by taking the ratio of the patch-wise calibrated mean trigger signal ($\langle T \rangle$) and the mean reconstructed charge ($\langle I_{\text{pixel}} \rangle$) for each dataset and then averaging over all full 9-pixel patches in the camera. The average trigger gain in this dataset is $\sim 7.0\,\text{TLSB/PE}$, although the pixel-wise trigger gain values have been applied during the reconstruction.

The maximum value of the trigger amplitudes transmitted by an individual channel is $\lfloor \frac{85}{2} \rfloor = 42\,\text{LSB}$, with the effective maximum (the clipping value) depending on the trigger gain and the scaling parameter. This clipping effect can be observed in the relative bias of the mean trigger amplitude, where the ratio starts to drop off from unity. The onset of the drop-off shifts to lower values of S for higher input light intensities. Similarly, setting the scaling to very low values, effectively cuts of the contribution of low numbers of individual photoelectrons to

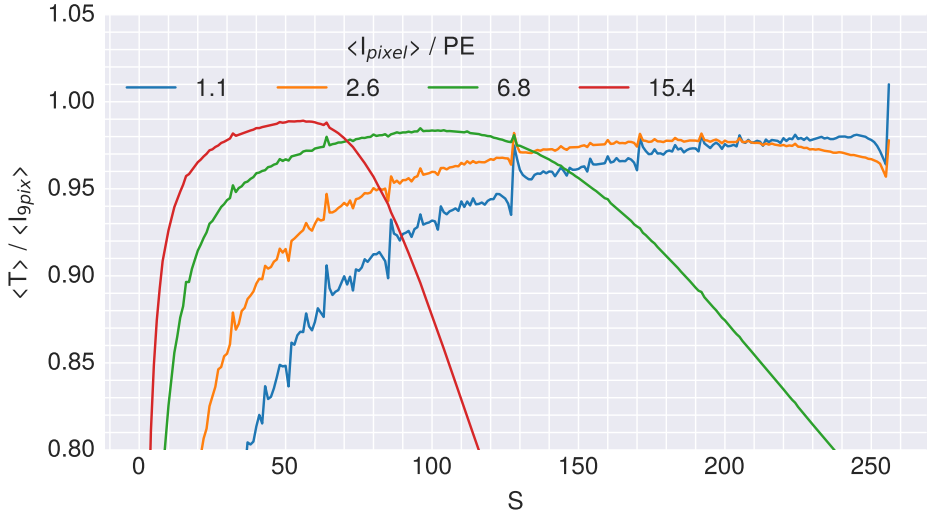

(A) Mean relative bias between trigger signals and charge reconstruction *without* digitisation effects reversed.

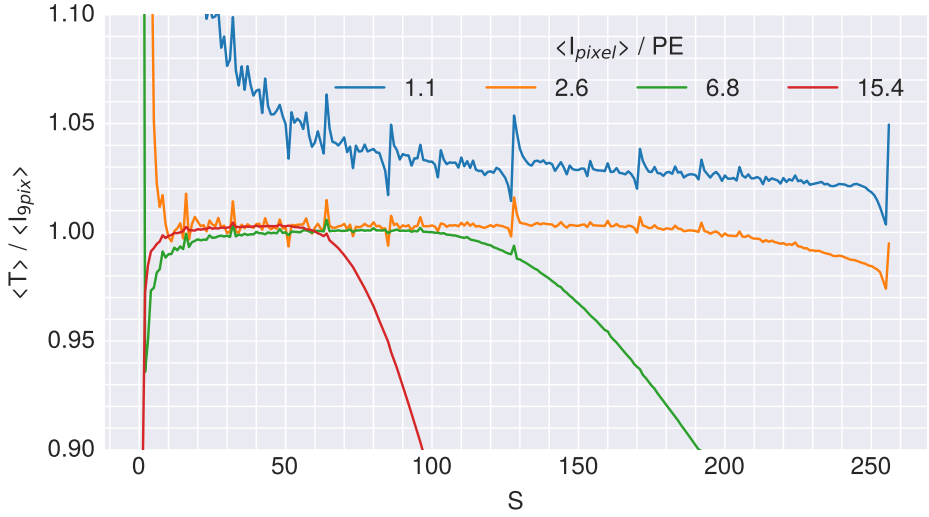

(B) Mean relative bias between trigger signals and charge reconstruction *with* digitisation effects reversed.

Figure 3.3: The mean relative bias between trigger signals and charge reconstruction of all 9-pixel trigger patches are shown depending on the scaling parameter S (for the `ppmm`-filter). Curves are shown for four levels of laser intensity, resulting in a mean pixel charges between 1.1 and 15.4 PE. The measurements have been made without background illumination. Panel (B) shows the ratios with trigger signals reconstructed using eq. 2.17, while panel (A) has been reconstructed omitting the offset aimed at reversing the digitisation effects.

the trigger sum, e.g. a trigger gain of 7 TLSB/PE and a scaling parameter of ≤ 36 would result in an effective trigger amplitude per photoelectron of < 1 TLSB/PE. This is especially pronounced for low light intensities (cf. fig 3.3A). Taking an additional patch-size dependent offset into account, the average truncation loss can be corrected independent of the trigger pulse amplitude (cf. fig 3.3B). This correction seems to overestimate the truncation loss for very low light intensities

(and lower signal-to-noise ratios), as additional biases may play a role, namely the biases due to the peak search methods used for both trigger and charge reconstruction, as well as the fact, that the negative trigger signals after the filter stage are zero-truncated, resulting in a small positive bias.

Distinctive spikes can be observed in the relative bias curve for low laser intensities, where the trigger operates in a regime, where individual photoelectrons can be resolved and the granularity of the possible trigger amplitudes is coarse. These effects get smeared out with increasing average pixel-intensity.

The influence of all these effects is small in any practical region of the trigger settings, but it can be concluded, when interpreting the mean intensity value $\langle I_{\text{pixel}} \rangle$ in terms of a trigger threshold, that the optimal value of S for intensities > 2 PE pixel can be found, where relative bias is close to unity (as large as possible).

3.2 Trigger efficiency

This section reports the study of the trigger efficiency as a function of illumination level and trigger configuration measured with one master trigger patch on the central PDP module, equipped with 7-dynode PMTs. The efficiency is measured by setting a fixed trigger threshold and scanning the laser illumination levels resulting in the so-called turn-on curve. The turn-on curves have been measured in the self-triggered and externally-triggered mode and compared to simulations of the measurement set-up. As the camera does not report, which trigger patch was above the trigger threshold, all trigger patches in the camera would have to be measured separately in the self-triggered mode, therefore a representative trigger patch was chosen, confirming the agreement with `FCTriggerSim`.

Verification of self-triggered trigger efficiency

For each setting of background illumination three representative trigger thresholds have been chosen, which would result in accidental camera trigger rates of ~ 1, 3 and 10 kHz. Then the intensity of the laser flashes was increased step-by-step scanning the trigger responses for each given trigger threshold. An event is classified as true or false positive based on the presence of the electrical laser trigger signal at its expected position (also possible in high NSB or low signal-to-noise ratio regimes). When this external pulse was found at the correct time stamp, the event was counted as a true event, otherwise it was classified as a false trigger, originating from background fluctuations. The laser was set to an emission rate of 1.5 kHz and data was taken for ~ 7 seconds, resulting in $\sim 10{,}500$ potential true positives. The exact measured time for each run was calculated by taking the Δt between the first and last recorded event in each run. The ratio of true triggers versus all laser flashes for each intensity step results then in the trigger efficiency (turn-on curves) shown in figures 3.4-3.6.

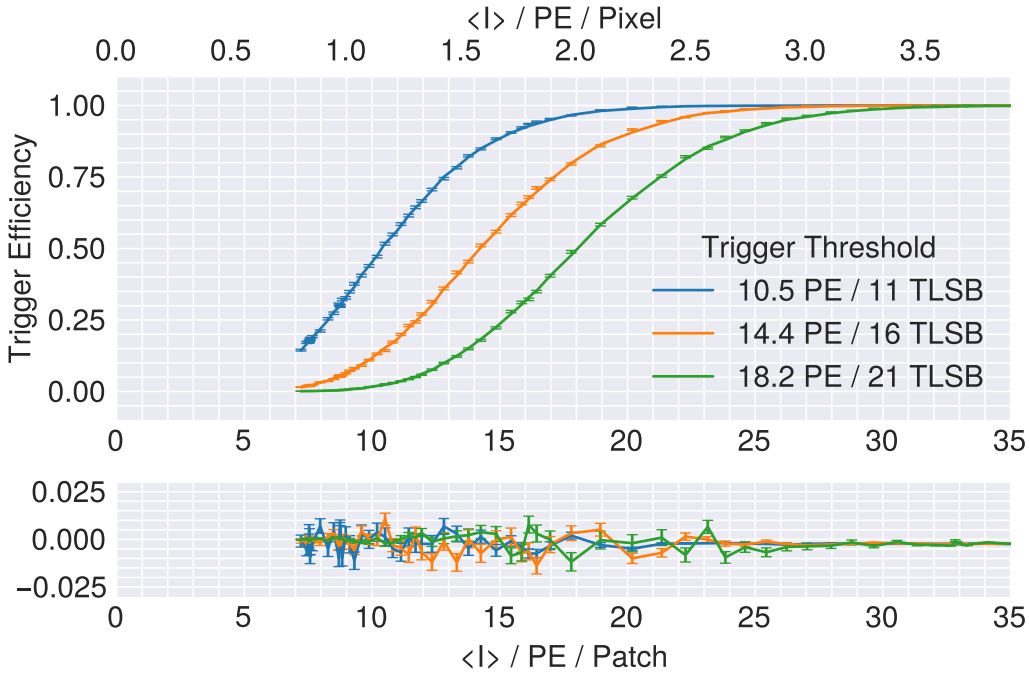

Figure 3.4: Trigger efficiency measurement with no background illumination and 10,000 events per setting in self-triggered mode (data points with error bars showing the statistical error) and externally-triggered mode (solid lines) for three trigger thresholds resulting in accidental camera trigger rates of 1, 3 and 10, kHz. The bottom figure shows the relative deviation between self-triggered and externally-triggered measurements.

The same measurement settings were then kept and an additional data taking run performed, but triggering the camera on the external laser pulse, and taking exactly 10,000 events. These events were processed with FCTriggerSim and events with a trigger signal above the same trigger threshold, as in the previous measurement, were counted as true triggers. The results of this analysis are also shown in figures 3.4-3.6. The results show a good agreement between the self- and externally-triggered analysis (within statistical uncertainty), and an overall agreement between the 50% intensity of the turn on curves and the set trigger threshold with the largest discrepancy in the turn-on curves without background illumination.

Comparison of simulations & externally triggered trigger efficiency

The externally-triggered measurements have been analysed in steps of 10 PE of the trigger threshold by choosing the closest corresponding value in hardware units (cf. figure 3.7 and 3.8). Shown are background rates of 417 MHz PE and 828 MHz PE for one setting of the scaling parameter (S=43, Clipping=~ 35 PE). The Poissonian model additionally shown in the figures has been obtained by a simple toy Monte-Carlo PMT model of the amplification at the first dynode. This model assumed a gain $G = 7$ the gain at the first dynode and the fraction of under amplified photoelectrons at 10%, with a relative amplitude of 1/6. The

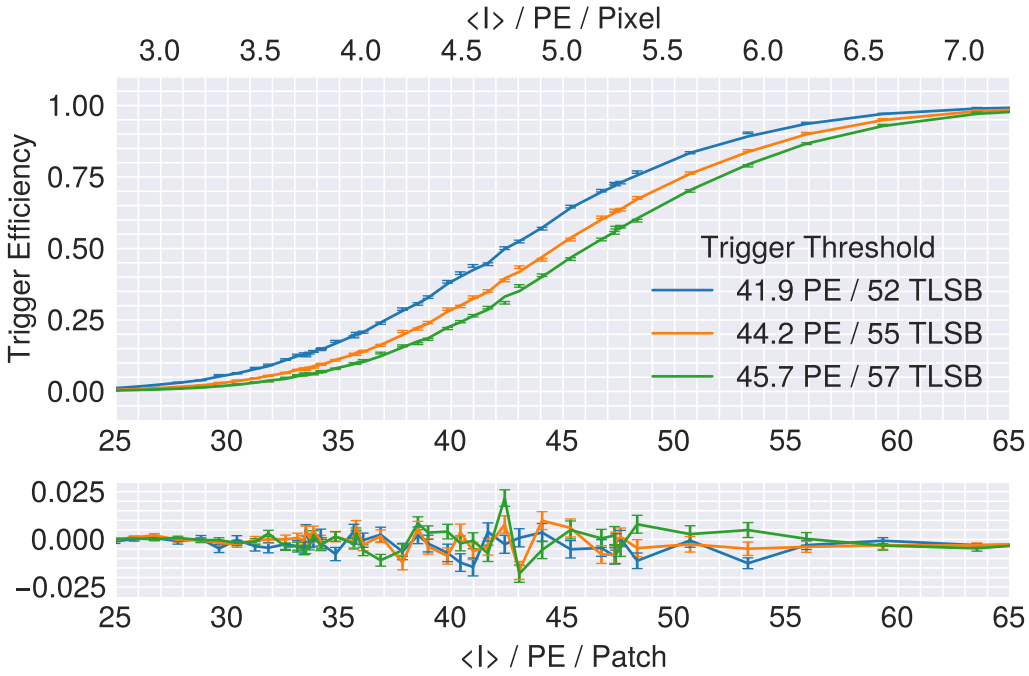

Figure 3.5: Trigger efficiency measurement with 417 MHz PE illumination and 10,000 events per setting in self-triggered mode (data points with error bars showing the statistical error) and externally-triggered mode (solid lines) for three trigger thresholds resulting in accidental camera trigger rates of 1, 3 and 10, kHz. The bottom figure shows the relative deviation between self-triggered and externally-triggered measurements.

background illumination was modelled using a normal distribution with zero mean and a width of $\sigma = \sqrt{f_{\mathrm{NSB}} \cdot \tau_{\mathrm{trigger\_width}} \cdot n_{\mathrm{pix}}}$, with $\tau_{\mathrm{trigger\_width}} = 8 \cdot 10^{-9}\, ns$ and f_{NSB} the expected rate of background photoelectrons per pixel.

$$A(k, \sigma) = 0.9 \frac{\mathcal{P}(G \cdot k | \mu = G)}{G} + 0.1 \frac{\mathcal{P}(6 \cdot G \cdot k | \mu = G)}{G \cdot 6} + \mathcal{N}(\mu = 0, \sigma)$$

with $\mathcal{P}$ the Poissonian probability mass function and $\mathcal{N}$ the normal distribution probability density function, and k the expected number of photoelectrons in the trigger patch. Using this equation a sufficient number of amplitudes have been produced, populating the cumulative distribution of A. The results of the mode, the full `sim_telarray` simulations and the measurements agree within 3% at the 50%-intensity point, except for very low intensities and trigger thresholds.

Emulation of time-gradient in arrival time

Cherenkov flashes from air showers may exhibit a time gradient from pixel to pixel up to one ns, mainly dependent on the impact parameter. To study this effect, this time gradient has been emulated by offsetting the sampling phase of individual pixels in the measured trigger patch. The relative sampling phase between all channels in a ADC card can be shifted up to 32 ns in steps of 1 ns; intended to compensate delays between the readout channels. This has been used

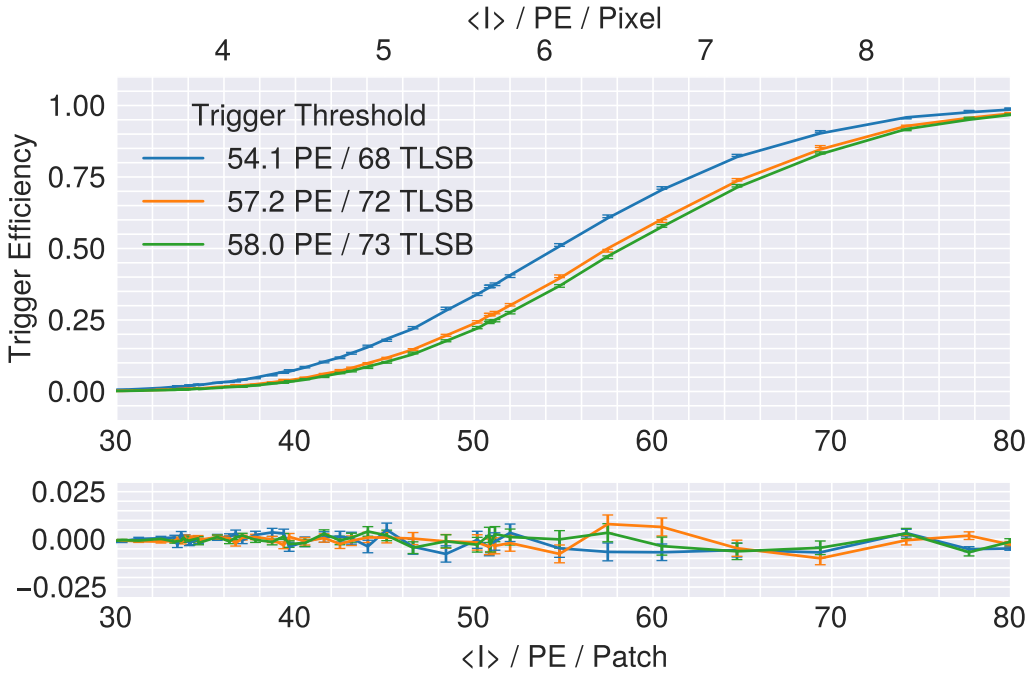

Figure 3.6: Trigger efficiency measurement with 828 MHz PE illumination and 10,000 events per setting in self-triggered mode (data points with error bars showing the statistical error) and externally-triggered mode (solid lines) for three trigger thresholds resulting in accidental camera trigger rates of 1, 3 and 10, kHz. The bottom figure shows the relative deviation between self-triggered and externally-triggered measurements.

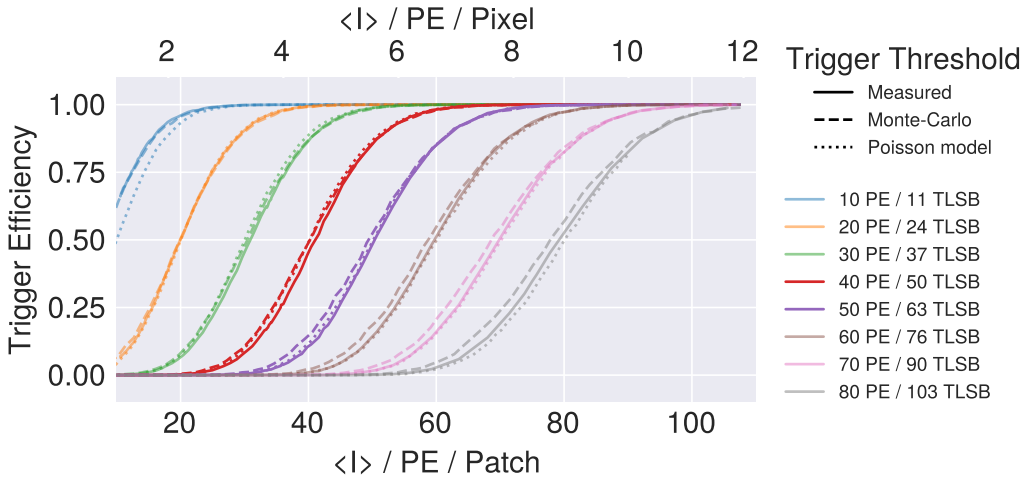

Figure 3.7: Trigger efficiency measurements as solid line, simulated data as dashed lines for a range of trigger thresholds. The background illumination was at 417 MHz PE. The lines with 40 and 50 PE trigger threshold result in accidental camera trigger rates in the range of 1-10 kHz. The dotted lines show the trigger shapes due to poissonian statistics and excess noise of only one dynode.

in the measurement set-up to delay pixels contributing to the trigger patch along the up-down axis of the camera in steps of 1 ns (cf. 3.11). The resulting trigger efficiency curves are shown in figures 3.9 and 3.9 for two levels of background illumination levels (417 and 828 MHz) respectively and compared to the undelayed

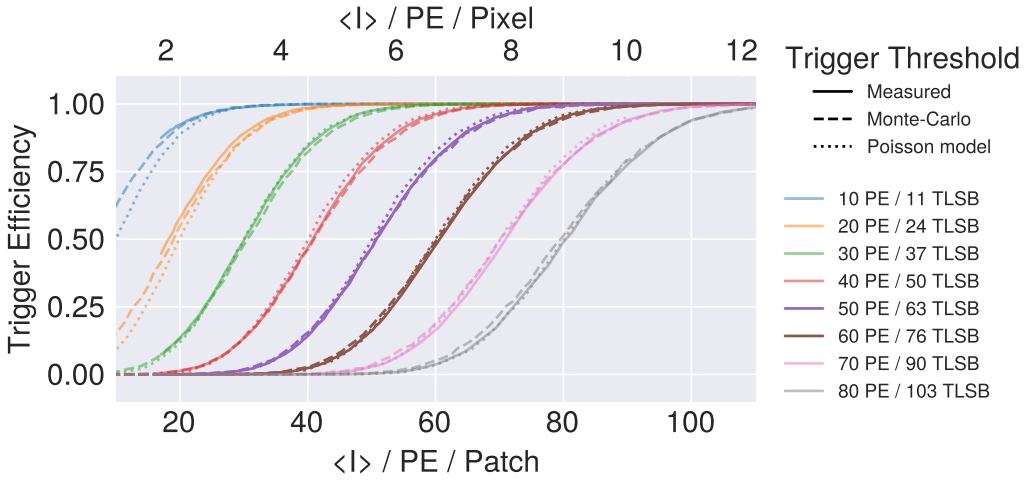

Figure 3.8: Trigger efficiency measurements in solid line, simulated data in dashed lines for a range of trigger thresholds. The background illumination was at 828 MHz PE. The lines 50 and 60 PE trigger threshold result in accidental camera trigger rates in the range of 1-10 kHz. The dotted lines show the trigger shapes due to poissonian statistics and excess noise of only one dynode.

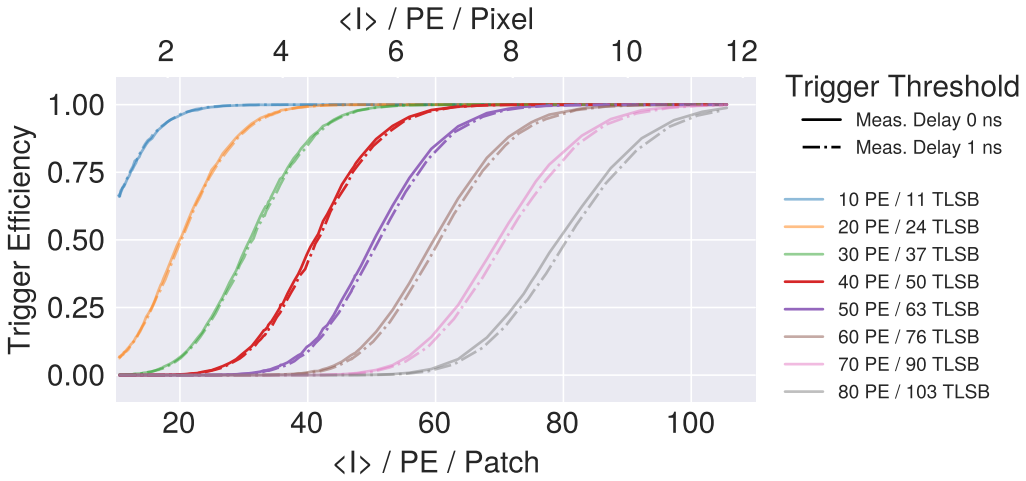

Figure 3.9: Trigger efficiency measurements for no time-gradient and a 1 ns time-gradient pixel-to-pixel with 417 MHz background illumination. Results show a shift of the 50% point of about 1-2%.

measurements. Figure 3.12 shows the shift of the 50% intensity for all studied trigger thresholds to be between 0.5% and 2.0% for measurements with night-sky background but moderate trigger thresholds and between 1% and 2% for higher thresholds, where the probability for accidental trigger decreases rapidly. As the trigger threshold is applied to the sum of the trigger signals from individual pixels this behaviour can be expected, namely contributions to the sum stem not from the maximum of the pulse, but slightly offset from their rising or falling edge. This effect is also modelled by the Monte-Carlo simulations.

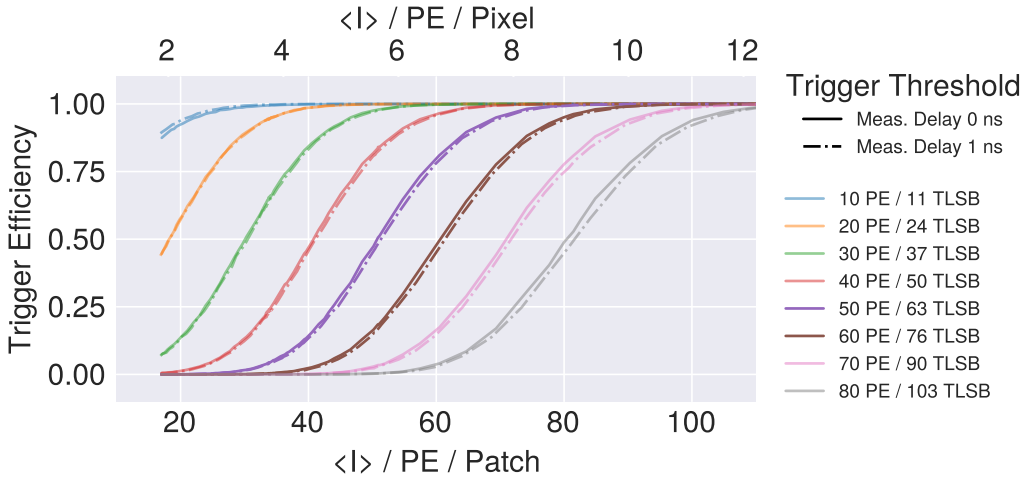

Figure 3.10: Trigger efficiency measurements for no time-gradient and a 1 ns time-gradient pixel-to-pixel with 828 MHz background illumination. Results show a shift of the 50% point of about 1-2%.

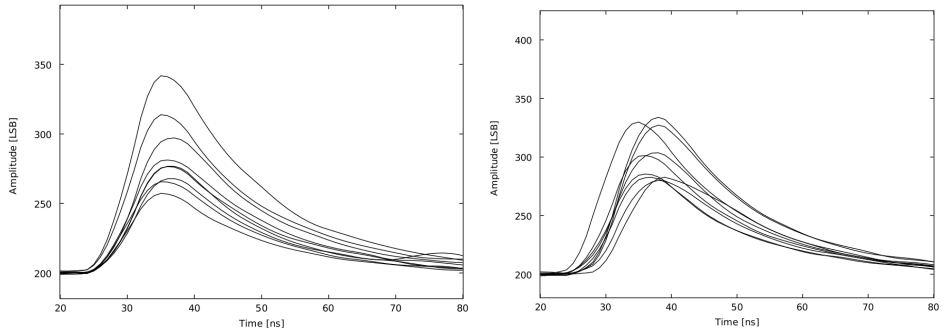

Figure 3.11: Measured pulses in 9 pixels of two exemplary events. The left panel shows the phase aligned set-up, whereas the right panel highlights the phase-delay of 1 ns between horizontal pixel rows in the camera. The pixels per row are grouped in a 1-3-3-2 pattern.

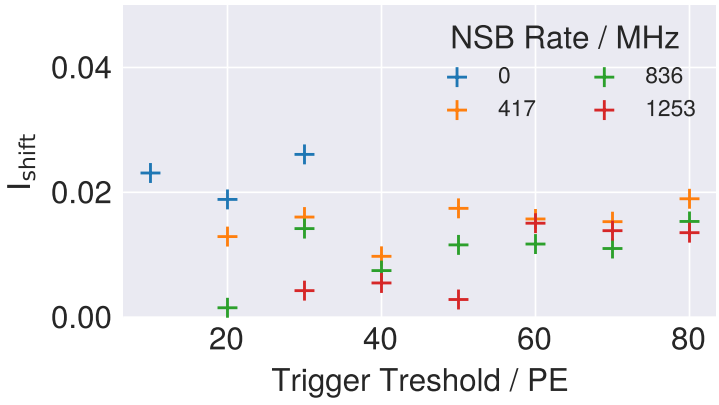

Figure 3.12: The relative increase (shift) of the intensity at the 50%-efficiency due to 1 ns delay (pixel-to-pixel) depending on the trigger threshold. The overall shift can be estimated to be between 1 and 2 %.

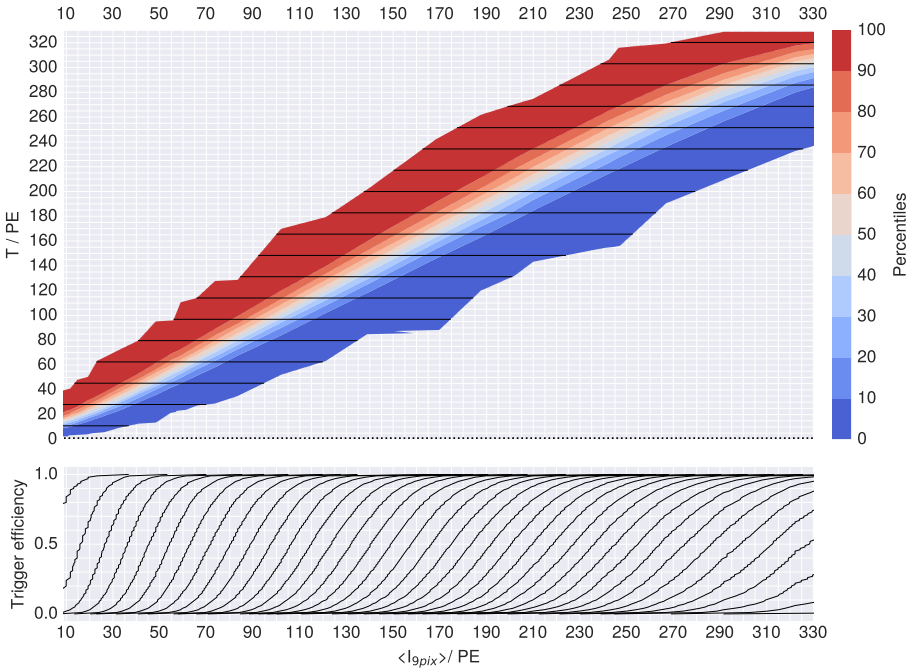

(A) Trigger signal distribution (T) as function of mean light intensity $\langle I_{9pix} \rangle$.

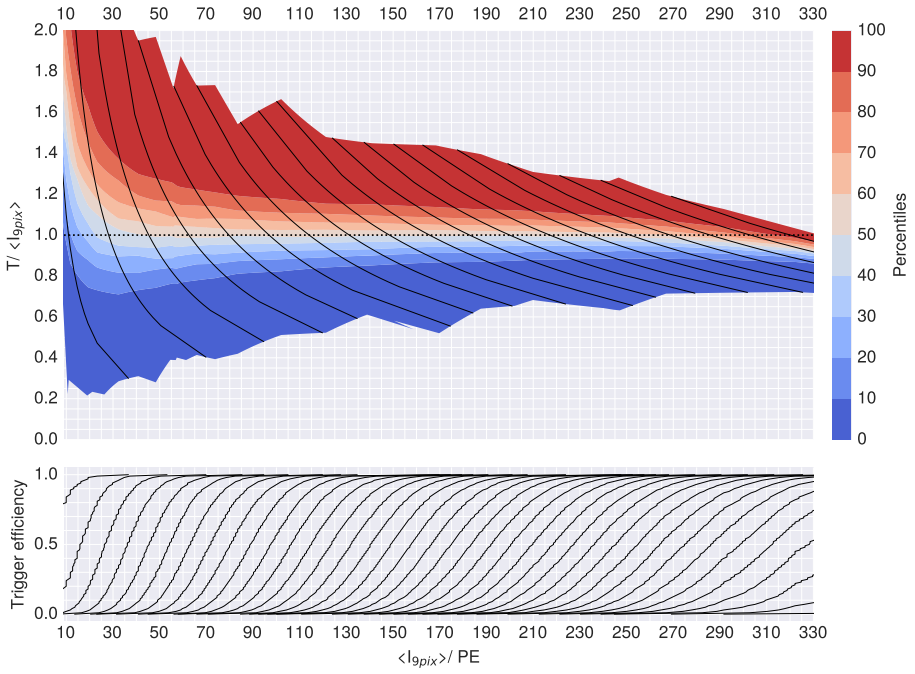

(B) Relative trigger signal distribution $T/\langle I_{9pix} \rangle$ as function of mean light intensity $\langle I_{9pix} \rangle$.

Figure 3.13: The black lines show a trigger threshold increasing in steps of 10 TLSB. The bottom figure shows the crossing points of the distribution with the trigger threshold resulting in the turn-on curves for each given trigger threshold.

3.3 Camera trigger uniformity

The previous section 3.2 has detailed the study of the trigger efficiency for one trigger patch, including the results of the self-triggered turn-on measurements. To study the 50% intensity points at the camera scale, the trigger sharpness and the uniformity across the camera, the externally triggered datasets containing all master trigger patches in the camera have been analysed for different levels of night-sky background light. Figures 3.13A and 3.13B show an intermediate step of the analysis for one trigger patch. The upper panel in figure 3.13A shows the trigger signal (T) distribution, for a mean reconstructed charge in a master trigger patch (per laser setting), while figure 3.13B gives the relative distribution. The black lines show the trigger thresholds in steps of 10 TLSB.

The crossing points between the percentiles points and the trigger threshold lines represent then the mean light intensity, at which the trigger patch has a trigger efficiency value of the corresponding percentile and trigger threshold. The lower panels of 3.13 are identical and show the resulting turn-on curves for the corresponding trigger thresholds.

This analysis has been performed for all 588 trigger patches in the camera and the distribution of the 50%-point of the turn-on curves are shown in figure 3.14. The bands show the 5-95th percentile distribution over all camera trigger patches, giving an estimate of the uniformity of the trigger threshold across the camera.

The value of T_{PE} is derived from the trigger threshold in TLSB by application of equation 2.17 and using the an average trigger gain. The ratio of the trigger signal T_{PE} to the I_{50} then represents the relative bias between the expected intensity (due to the value of trigger threshold) and actually reconstructed charge.

The median bias for all measured levels of background light (up to $\sim 2\,\mathrm{GHz}$) and the full range of possible trigger thresholds is shown to be within 1%.

The uniformity of the 50% point across all trigger patches is shown by the shaded bands (5-95 percentiles) in figure 3.14 and can be estimated to be within ±1% for the relevant regions of background light and signal intensities.

The trigger sharpness is shown in figure 3.15 by determining the spread (10- and 90%-points) of the light intensities measured for a given trigger threshold. This spread increases with more background light and scales with the trigger threshold. The measured results are compared to the expected 10-to-90% spread of a Poisson distribution scaled with the known excess noise factor of the FlashCam PMTs, which shows a very good agreement with the measured spread.

$$\sigma_{90-10} = \mathcal{P}_{\mathrm{PPF}}(0.9|\mu) - \mathcal{P}_{\mathrm{PPF}}(0.1|\mu) \tag{3.3}$$

$$\mu = \mathrm{T_{PE}} + \mathrm{B_{PE}} \tag{3.4}$$

$$B_{\mathrm{PE}} = \mu_{\mathrm{NSB}} \cdot \tau_{\mathrm{effective}} \cdot \mathrm{n_{pix}} \tag{3.5}$$

with $\mathcal{P}_{\mathrm{PPF}}$ the Poisson percent point function evaluated at the 10 and 90 percentile points.T_{PE} is the trigger threshold in units of photoelectrons, while B_{PE} is the effective number of background photoelectrons. This effective number scales the mean number of background photoelectrons per sample and pixel with an effective integration window (the width of the pulse shape $\tau_{\mathrm{effective}} = 8ns$) and the number of pixels in the trigger patch ($n_{pix} = 9$).

The distribution across the trigger patches of the camera are again shown as shaded regions (5 and 95th percentile). The spread increases for high trigger thresholds, as the clipping is applied channel-wise and downward fluctuations may still produce trigger signals, which are below the threshold even if the mean intensity in the trigger patch is larger than the trigger threshold. The 90% point on the other hand reaches the trigger maximum earlier and continues to increase with increasing laser intensity.

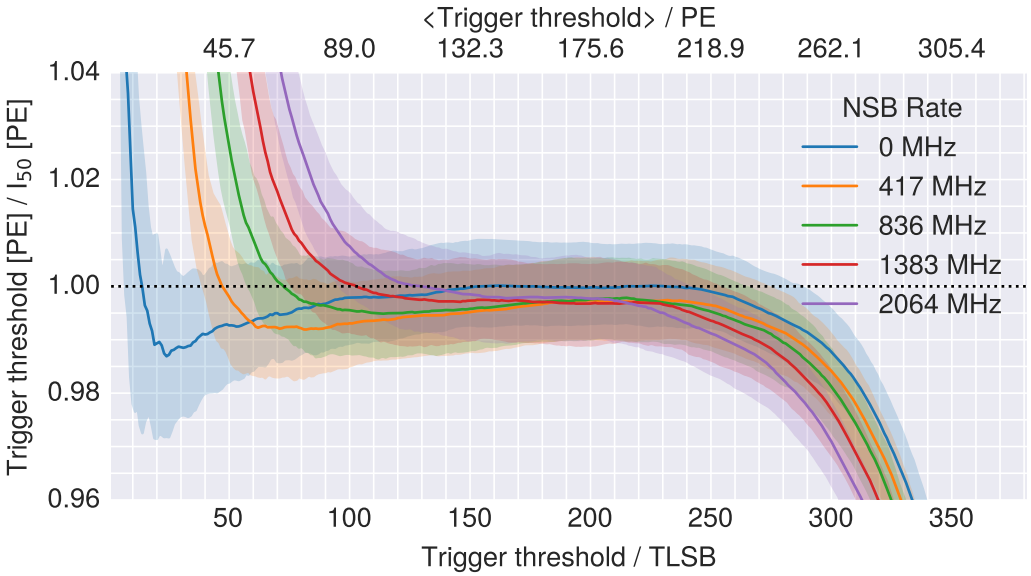

Figure 3.14: The relative bias of the expected value of the trigger threshold (using eq. 2.17 the 50 percent point of the turn-on curve is shown as a function of of the trigger threshold in TLSB. The distribution for all trigger patches in the camera is given by showing the median as the solid line, while the shaded regions give the 5 and 95 percentile of the distribution. The colours show the same analysis for increasing levels of background illumination. The relative bias is within 1%, while the homogeneity of the camera is within 1.5%. The curve for no background illumination shows the largest deviations, but this setting is not expect to occur in the field. The drop of the bias for higher thresholds is due to the clipping of the individual channels. The upper axis shows the mean trigger threshold in units of photoelectrons.

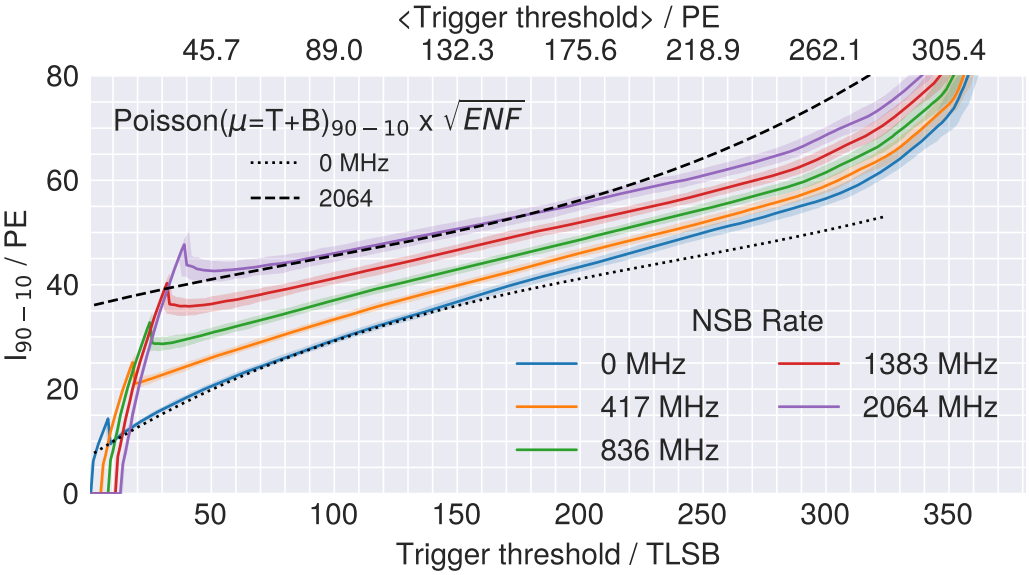

Figure 3.15: The spread of the turn-on curves is estimated by the absolute difference in light intensity of the 10 and 90 percent trigger efficiency values (I_{90-10}) as a function of trigger threshold. The median of the distribution over all trigger patches in the camera is shown as a solid line, while the 90% of the distribution are given by the shaded regions. The spread is given for increasing levels of background illumination. The Poisson limit (widened by the excess noise of the PMTs) is shown as the dotted line, with T the trigger threshold and B the number of expected background photoelectrons added to the trigger signal (cf. eq. 3.3). The upper axis shows the mean trigger threshold in units of photoelectrons.

3.4 The night-sky background

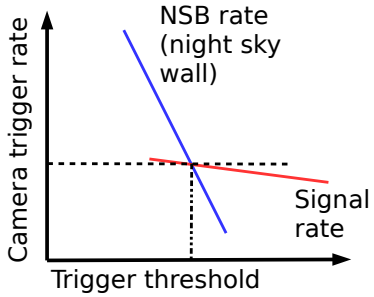

Figure 3.16: Depiction of the camera trigger rates due to night-sky background (the night sky wall) and signal trigger rates. The signal rates include air showers.

Two sources of background dominate the camera trigger rate: for high thresholds, air showers of non γ-ray origin present a nearly irreducible background because of very similar topologies as γ-rays [1]. However, for low thresholds, the main source of accidental or background triggers is light originating from the night sky. The expected rate of background light is estimated to vary between 300 MHz and 1500 MHz of photoelectrons per pixel for a FlashCam camera mounted on an MST. The variation in the background illumination levels depends mostly on the region of the sky the telescope is pointing towards. The choice of the actual trigger parameters in operation has to take the observation conditions into account — the galactic plane and nebulae such as that surrounding the Eta Carinae γ-ray source present diffuse backgrounds factors of three to five times brighter than the extragalactic background light. A coincidence condition between multiple telescopes in a telescope array allows to efficiently discard these background triggers. It is nevertheless important, that all telescopes are operating with minimal deadtime, otherwise a signal trigger may be missed, giving an upper limit to the allowed trigger rate of a single telescope. When setting the threshold too close to the so called night sky wall, one has to keep in mind that a small change of background illumination level will result in a considerable change in the camera trigger rate (cf. 3.16). Understanding the background response of the trigger system and its settings is therefore crucial. This task has been performed by using the Monte-Carlo simulation framework, where the trigger response of the system could be studied by changing individual PMT parameters artificially. The valid ranges of the trigger settings have been studied by scanning parameters space, also in ranges of artificial observation conditions, which are not expected to occur in the field (e.g. a wider range of background illumination levels).

[1] The compact 9-pixel trigger of FlashCam is the configuration most sensitive to γ-rays [priv. comm. K. Bernlöhr]

3.4.1 Methods to analysing background trigger rates

The laboratory set-up detailed in section 2.3 has been used to take data with the FlashCam prototype illuminated with different levels of continuous background light, in a range between 300 MHz and 4 GHz photoelectrons per pixel. The camera was taking data in two different modes during the measurement campaigns. First in self-triggered mode, a coarse scan of the available trigger parameter space was performed while reading out only the minimum possible two samples per event, determining the trigger rates of the camera. Second, using an internal trigger from the readout system, reading out the maximum number of samples, effectively taking 15.6 µs snapshots of the digitised background illumination. The datasets obtained in the second mode were used to recompute the trigger rates from the digitised data offline on the MPIK computing cluster.

3.4.2 Simulation set-up

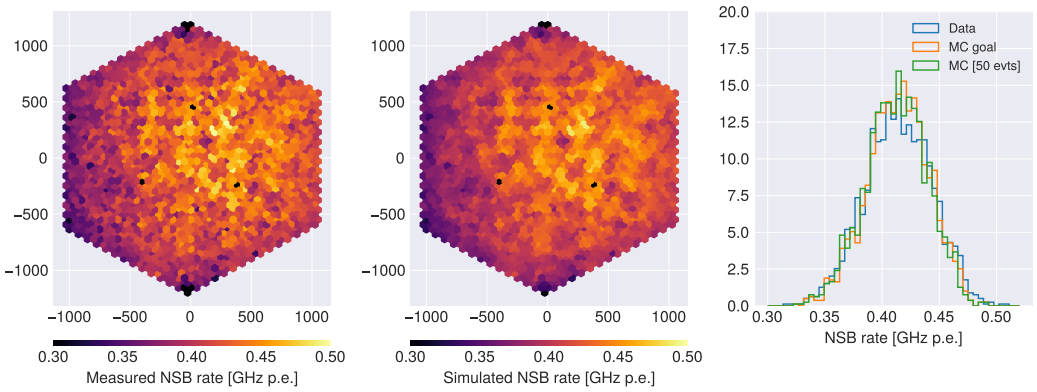

Figure 3.17: Pixel-wise background illumination rates of the measured dataset with an average illumination level of 417 MHz PE per pixel (exemplary for all measured illumination levels). The left panel shows the measurement, which has been used to extract a reference map of the laboratory conditions. This map was used to set the pixel-wise NSB levels in the simulations (middle panel). The right panel compares the distribution of the measured and simulated data with the Monte-Carlo goal (the reference map).

The two-fold approach of this work has been to measure the various trigger characteristics and tune and update the Monte-Carlo simulation description with the gained knowledge, and in turn study the influence of the uncertainty associated with these parameters using simulations. The simulated datasets have been produced using the PMT configurations presented in section 2.5 and the intricacies of setting the gain (`fadc_amplitude`) in the simulations (detailed in section 2.4) have been taken into account. Additionally the simulations replicate the inhomogeneities of the LED illumination in the laboratory. Figure 3.17 presents the background light measured in the laboratory and replicated in simulations. Both 7-dynode and 8-dynode PMT variants have been simulated separately, taking the respective gain values and change of the gain with increasing NSB into account.

3.4.3 Validation of FCTriggerSim & self-triggered camera trigger rates

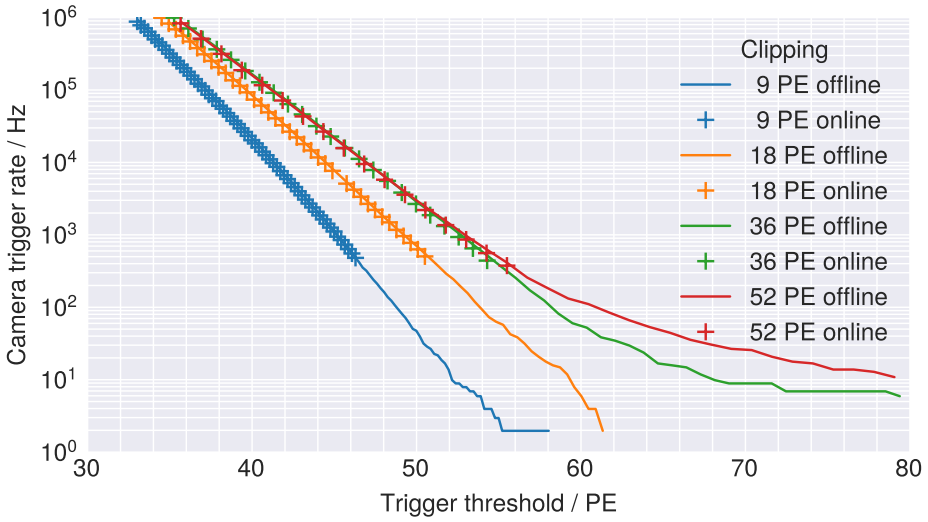

Figure 3.18: The camera trigger rates due to background illumination of 417 MHz PE measured in self-triggered mode (online) are compared to the calculated camera trigger rates (offline). Four settings of clipping values are shown. Both measurements match and justify the use of FCTriggerSim for furthers studies.

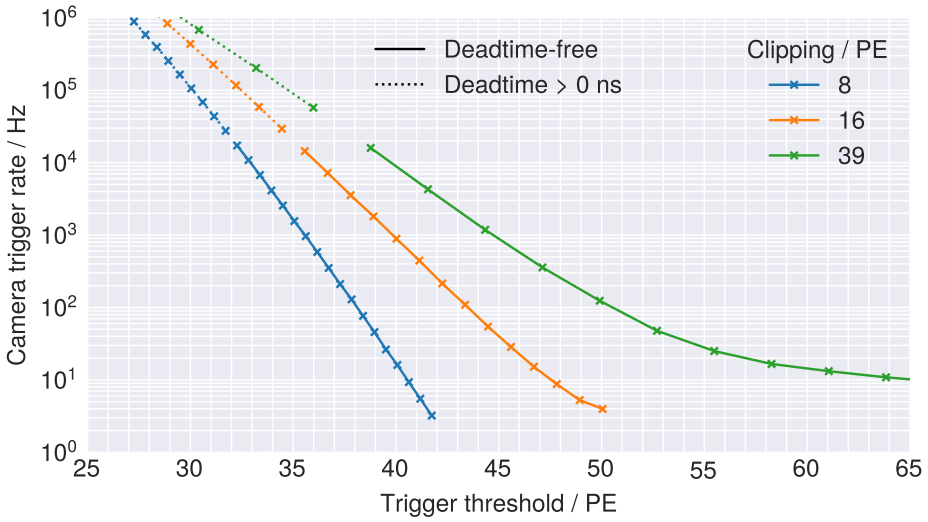

Figure 3.19: Self-triggered measurements of the camera trigger rates. Dotted line connect measurements, where the camera readout exhibited deadtime, while the solid lines show deadtime-free measurements. This confirms the expected maximum readout rate to be ~ 20 kHz.

The full camera trigger rates induced by homogeneous background illumination (417 MHz PE) have been measured in self-triggered mode to confirm the correct implementation of FCTriggerSim. Figure 3.18 shows the comparison of both measurements taken in sequence to minimise the effects of temperature changes of the LED source and the camera. Each data point shown (labelled "online" in fig. 3.18) has been measured separately with a relative statistical error of 1%. The self-triggered measurements have been measured down to trigger

rates of ~hundred Hz here and hence took up to a minute per data point. In the externally-triggered mode, the dataset amounts to 10,000 events, with 3900 samples, resulting in 15.6ms of data. Both measurements are in very good agreement, confirming the match between the firmware and the implementation of FCTriggerSim and allowing its application in the further studies.

A dedicated measurement, checking the expected deadtime-free readout rates ~20 kHz, has been performed and is presented in figure 3.19. The trace length of the read out events was set to 6 samples.

3.4.4 FCTriggerSim in floating point

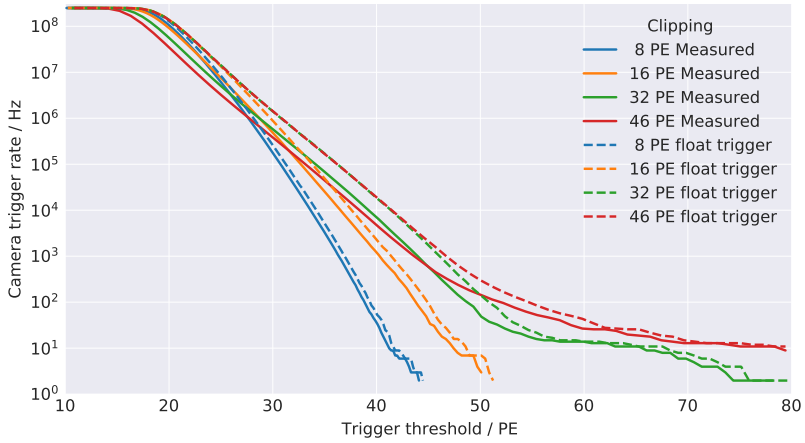

Figure 3.20: Camera trigger rate computed in floating point (labelled "float trigger") and integer numbers (labelled "Measured") from measured datasets. The unit conversion from TLSB to PE has been applied *without* the digitisation effects taken into account.

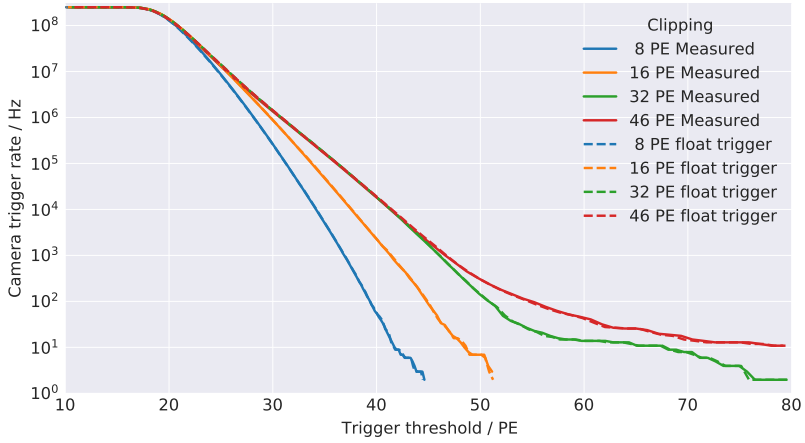

Figure 3.21: Camera trigger rate computed in floating point (labelled "float trigger") and integer numbers (labelled "Measured") from measured datasets. The unit conversion from TLSB to PE has been applied *with* the digitisation effects taken into account (cf. eq. 3.6).

The trigger path in the firmware and consequently the software reimplementation FCTriggerSim is calculated in integer numbers. There are two steps involving a division. The first step is the application of the scaling parameter, where a division by 256 (bit shift by 7) is applied after the multiplication with the scaling parameter. The second division operation divides the 3-pixel sum by 2 (bit shift 1), before it is sent to the trigger cards. The effect of these truncations has been studied by implementing the FCTriggerSim logic with 32-bit floating point logic and applying the FCTriggerSim to the same NSB dataset.

An average correction for these truncation effects improves the accuracy when converting trigger signals or trigger threshold from TLSB to PE. The resulting relation is

$$T_{\text{corrected}} = T_{\text{TLSB}} + 0.5 + 0.25\, n_{\text{pixel}} \tag{3.6}$$

where n_{pixel} is the number of pixels in each master trigger patch. The difference between uncorrected and corrected trigger signals can be observed in figure 3.20 and 3.21 respectively. The influence of the truncation is most pronounced for high clipping settings, where the absolute values in the trigger path are smaller, and the relative influence of the truncation is large.

3.4.5 Absence of correlated signals in the background

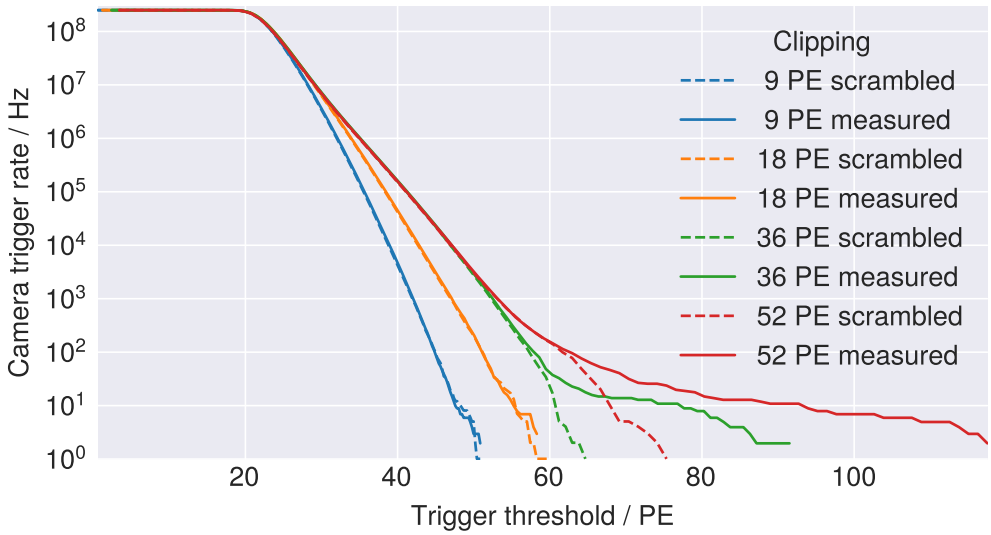

Figure 3.22: Comparison of measured trigger rates with an artificial dataset, where the pixel traces have been scrambled in time and space, cross-checking for correlated background signals. The camera trigger rates have been calculated for a range of clipping values. The scrambled and unscrambled trigger rates (solid and dashed lines respectively) show no deviation for trigger rates $> 100Hz$.

The contributions to the background light in the camera trigger rates considered so far are assumed to be from electronic noise, continuous illumination (NSB) and afterpulsing. These sources are expected to be uncorrelated between

individual pixels, i.e. the accidental trigger rate is expected to be mainly due to fluctuations in the number of background photons. The afterpulsing rate is dependent on the night-sky background intensity per pixel, but due to the uniform distribution in arrival times of the photons, the induced afterpulses will be distributed equally in the readout traces.

The electronics may exhibit correlations nevertheless due to cross-talk between channels, or artificial pulse-like signals, which may get picked up by the trigger. The contribution to the overall camera trigger rate of any signal of this type has been checked by analysing the internally-triggered datasets with FCTriggerSim, but scrambling the raw readout traces of each pixel. More specifically, the events of the dataset have been loaded into an intermediate buffer in chunks of 1764 events (the same number as the number of pixels in the camera) and then constructing new events, by first randomising the position of the pixels and then picking raw traces at random from the buffer, with the added condition that no two traces originate from the same original event. This algorithm ensures, that no trace in the newly assembled event has an overlap in the recorded time interval with any other trace and that groups of pixels which may be subject to a constant higher light intensity are distributed equally over the camera.

The results of this cross-check are presented in figure 3.22. The unscrambled and scrambled trigger rates show no significant deviations for trigger rates above 100 Hz confirming that these regions are dominated by uncorrelated background. The tails in the 36 and 52 PE clipping curves must therefore originate from sources producing simultaneous pulses in two or more pixels in a master trigger patch. A likely explanation for these signals are muons passing through the PMTs or the glass of the camera window.

In any case the contribution to the camera trigger rates, compared to the expected hadron and electron induced shower background rates in later operation ($\sim$ 2-3kHz) are less than 1%.

3.4.6 Influence of the afterpulsing

The influence of the afterpulsing on the camera trigger rates has been studied by varying the configurations in the `sim_telarray` simulations. Initial studies of the FlashCam team had shown, that the FlashCam PMTs would be better described with a spectrum, whose integral probability above 4 PE is of the order or $1 \cdot 10^{-4}$. For this reason, the original configuration file with an integral afterpulsing probability of $2 \cdot 10^{-4}$ has been scaled by factors of 0.5 and 0.25 used in this comparison. The later studies of the afterpulsing spectrum of the FlashCam PMTs confirmed the results of the initial studies (results are shown in section 2.5). The simulations presented here had been completed before the final update to the simulation parameters had taken place. Nevertheless, the spectrum with a total probability of $1 \cdot 10^{-4}$ is the more realistic description of the PMTs and provides a reference value in the comparisons in figure 3.23. The simulations, where

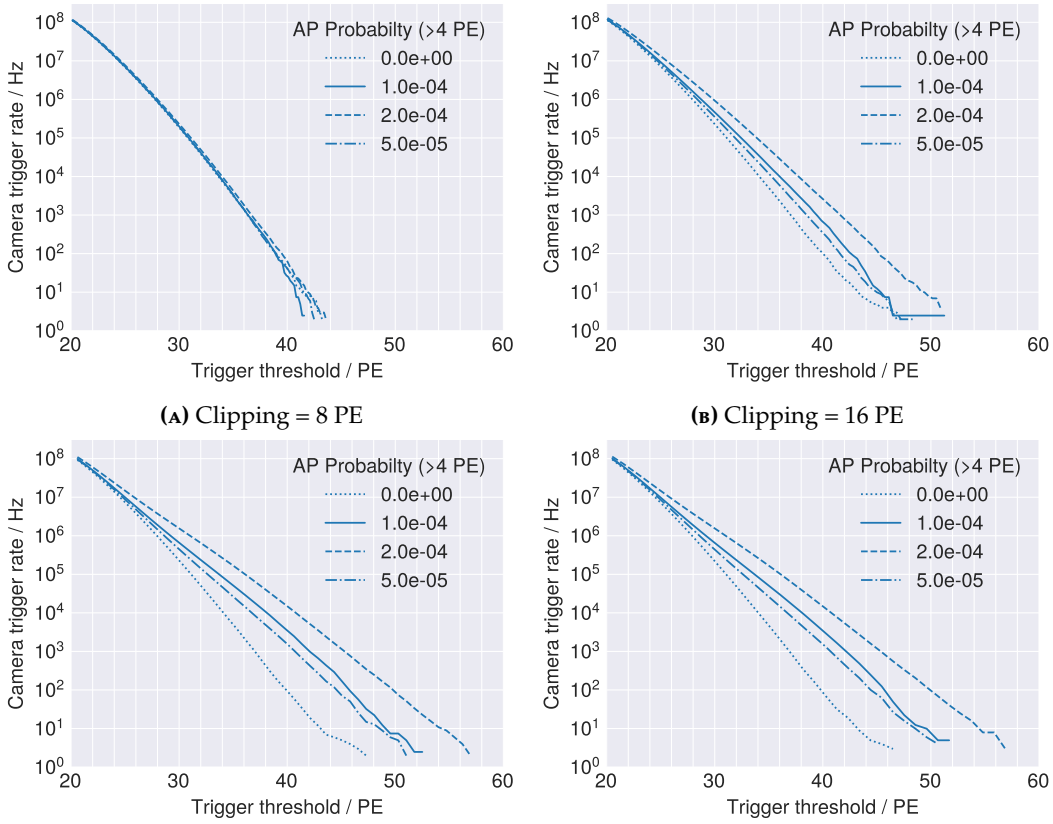

(A) Clipping = 8 PE

(B) Clipping = 16 PE

(C) Clipping = 32 PE

(D) Clipping = 44 PE

Figure 3.23: Camera trigger rates of Monte-Carlo simulations with four levels of afterpulsing and a night-sky background rate of 300 MHz · PE. Panels (A)-(D) show the analysis of the same dataset with increasing levels of the clipping parameter. While the influence of the afterpulsing is suppressed for a small clipping value (8 PE), the contribution to the overall trigger rate increases up to higher clipping values (32 PE), where it levels off. This is due to the fact, that the afterpulsing probability in the simulations is defined up to 30 PE. However, comparison with the measured afterpulsing spectra shows that this range is sufficient.

the PMTs exhibit no afterpulsing, act as a baseline comparison to estimate the influence of the afterpulsing on the trigger threshold. The increase of the trigger threshold due to the afterpulsing for a fixed camera trigger rate (between 10^3 and 10^4) for a high clipping (>32 PE) setting can be estimated to be between 5% and 15%. This confirms the assumption, that the camera trigger rate in the relevant range is dominated by individual afterpulses combined with upward fluctuations of the background photoelectron distribution and in turn making the scale factor (due to the implied change of clipping threshold) an important parameter to tune this contribution.

3.4.7 Influence of the single-photoelectron spectrum

As with the study of the influence of the afterpulsing on the camera background trigger rates, dedicated simulations have been produced with both the new and old single photoelectron spectrum configuration file. The results are presented in

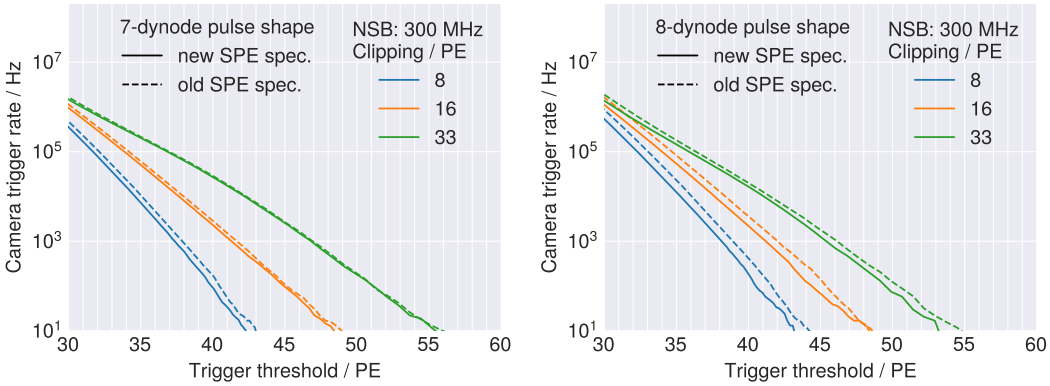

(A) (B)

Figure 3.24: Comparison of simulated camera trigger rates highlighting the difference between the old and new single photoelectron spectrum configuration for combinations of 7- and 8-dynode pulse shape with 300 MHz PE background illumination levels. Each simulated dataset has been analysed with three settings of the clipping parameter (8, 16, and 33 PE).

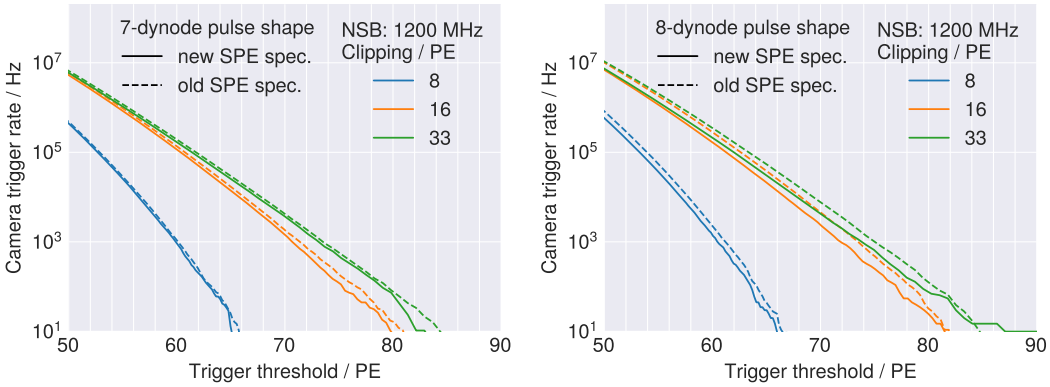

(A) (B)

Figure 3.25: Comparison of simulated camera trigger rates highlighting the difference between the old and new single photoelectron spectrum configuration for combinations of 7- and 8-dynode pulse shape with 1200 MHz PE background illumination levels. Each simulated dataset has been analysed with three settings of the clipping parameter (8, 16, and 33 PE).

figure 3.24 and 3.24, with dedicated simulations using the 7- and 8-dynode PMT configuration (including their respective afterpulsing spectra), and two settings of the night-sky background rate (300 and 1200 MHz PE). The trigger settings in this comparison used the 9-pixel sum trigger, the `ppmm`-filter and three settings of the scaling parameter resulting in clipping values of 8, 16 and 33 PE. The variation of the clipping (as shown before) tunes the influence of the afterpulsing and therefore the relative influence of the night-sky background fluctuations and the induced afterpulsing in the 300 MHz PE simulations (cf. figure 3.24A, 3.24B).

The actual shape of the single photoelectron spectrum has the strongest influence in the night-sky background (low clipping or high NSB) dominated regime, as the pulse heights of the detected photoelectrons are sampled from the SPE distribution, while the afterpulsing spectrum did not change.

Attributing the size of the shift of the trigger threshold between both input configurations to a specific feature in the single photoelectron spectrum would require detailed studies, varying the input spectrum artificially and studying the single- and multi photoelectron response of the trigger filters on a single readout channel level instead of the full camera trigger level. An interpretation of the shown behaviour would be, that the wider effective integration window of the 8-dynode PMT trigger filter responds stronger on a change of the pulse height distribution width (as the new SPE spectrum is slightly narrower, and has a smaller excess noise factor). In other words, the reduced variation in the neighbouring samples of the trigger response peak has a stronger influence on wider input pulse shapes.

The maximal shift in trigger threshold for the presented parameter variations is of the order of 3% for 8-dynode PMT and less for the 7-dynode PMT.

3.4.8 Number of pixels in master trigger patch

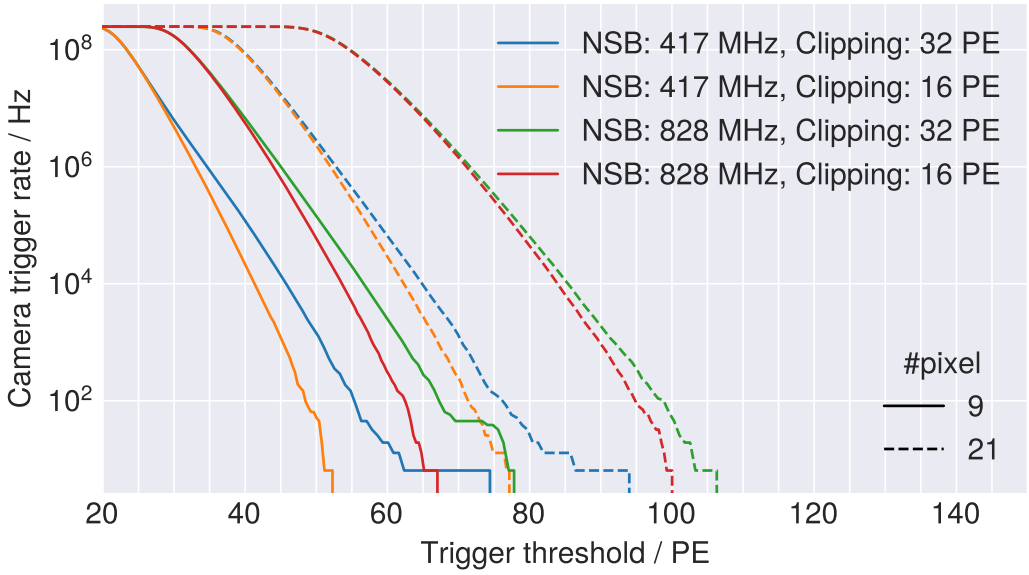

Figure 3.26: Comparison of measured camera trigger rates with 9- and 21-pixel trigger patches. Additional variations shown are for two levels of NSB and two settings of the clipping parameter.

The trigger system may be configured with a variable number of 3-pixel patches contributing to each final master trigger patch sum. The trigger sum is expected to behave similar to an increase in background illumination or an increase in number of pixels contributing, as the signals from each pixel are uncorrelated (as long as the background illumination matches the respective change in the number of pixels). This is demonstrated in figure 3.26, where the measured camera trigger rates with 9- and 21-pixel sums are shown for two levels of background illumination and two settings of the clipping parameter. The clippings have been chosen to allow for the full contribution of the afterpulsing (32 PE)

	FWHM of trigger signal	
Shaping Filter	7-dynode PMT	8-dynode PMT
2pm	6.5 ns	7.1 ns
2pom	8.0 ns	8.4 ns
ppmm	8.9 ns	9.4 ns
ppomm	10.7 ns	10.9 ns

Table 3.1: Effective width of the filter response pulse shapes (7- and 8-dynode PMTs), derived from the median full-width at half-maximum of the input pulse shapes, subsampled in steps of 0.1 ns.

and a cut-off of the afterpulsing (16 PE), while still allowing the full range of the fluctuations of the NSB in both settings. The increase in NSB reduces the gap between the two clipping curves of the 9-pixel trigger sum, which is expected as the background fluctuations are dominated more by the pile-up and the effect of the afterpulsing is less pronounced. The comparison to the 21-pixel curves at the same NSB level shows a similar effect as the NSB increase for the 9-pixel sum, while an increase in the NSB rate for the 21-pixel sums moves the camera trigger rates further into the pile-up dominated regime. Naturally, for a fixed camera trigger rate and a fixed level of background illumination, the trigger threshold will be shifted towards higher levels, when switching from 9- to 21-pixel sums.

3.4.9 The trigger shaping filters

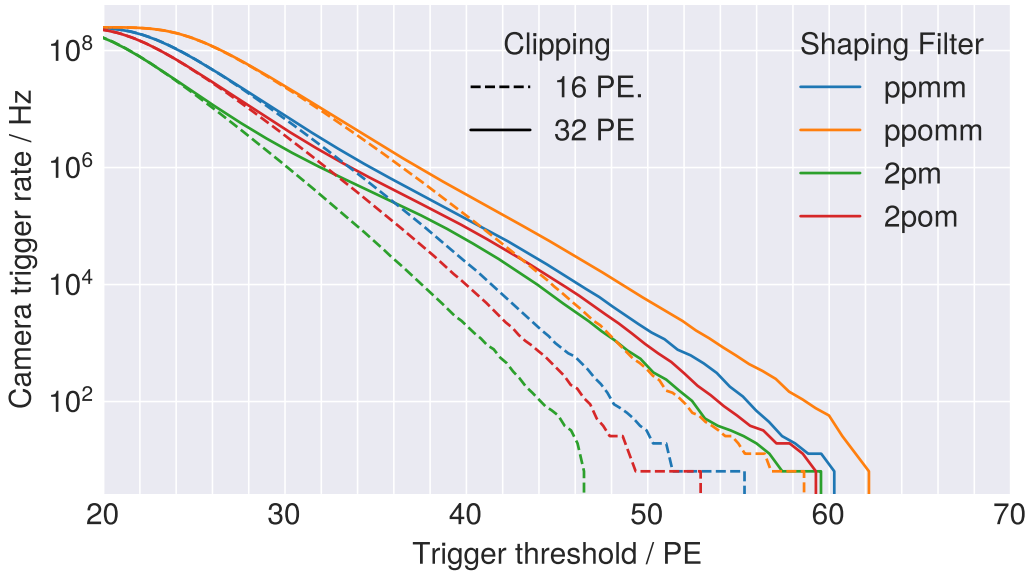

Figure 3.27: Comparison of the 4 available shaping filters, for one setting of background illumination at 417 MHz PE and 9-pixel patches. Comparisons are shown for two levels of clipping (16 and 32 PE). The trigger rates are computed from 7-dynode PMT simulations.

The responses of the 4 available trigger shaping filters applied to the pulse shape have already been discussed in section 2.5 and the effective integration widths of the trigger shaping filters are given in table 3.1. Figure 3.27 shows the difference in the camera trigger rates due to the different effective integration times.

The difference between the filters is more pronounced in the lower clipping setting, where the influence of the night-sky background fluctuations dominate and the effective integration window plays a larger role. In the high clipping setting the higher afterpulses are allowed to contribute more and the ratio of afterpulse height to average background pulse height gets larger, reducing the influence of the night-sky background and therefore reducing the influence of the effective integration windows of the trigger shaping filters.

For the low clipping settings, the difference between the shaping filters is up to 20% for a fixed camera trigger rate. The difference of the trigger threshold for a high clipping in the relevant camera readout rates (< 20 kHz) is on the order of 10% between all filters, reducing to ~ 5%, when disregarding the `ppomm` filter, which has the widest trigger response shape.

3.4.10 Comparison of measurements and Monte-Carlo simulations

The results regarding the input parameters and trigger parameter variations so far presented have been derived from Monte-Carlo simulations of the camera. An extensive comparison of the latest Monte-Carlo description for the 7- and 8-dynode PMTs variants with the measurement set-up are presented here. Figure 3.28 highlights the variation of clipping parameter, while figure 3.29 reports the results for the full range of the evaluated night-sky background levels (0-4 GHz PE).

The per-channel dynamic range in units of photoelectrons of the trigger system depends on the scaling parameter (S). The clipping value depends inversely on the scaling parameter and limits the contribution to the total trigger sum. This limit influences mainly the contribution of the PMT afterpulsing to the background trigger rates, which has been shown to dominate the camera triggers in the region of dead-time free readout (cf. 2.5) and night-sky background rates < 1 GHz PE. The contribution of the afterpulsing is less pronounced in the pile-up dominated regime with higher levels of background illumination (cf. 3.28c), as the sum of expected number of photoelectrons due to the NSB is notably larger than any contribution of an afterpulse [2]. Lowering the clipping further will reduce the contribution of the afterpulsing substantially, but also reduce the dynamic range of the system. For increased levels of NSB, this might truncate the per-channel NSB fluctuations, suppressing any signal contribution. Increasing the clipping to very

[2]This can be seen by the smaller relative shift in trigger threshold for a fixed camera trigger rate (~ 5% at 1 kHz) between clipping values of 15.5 and 31.5 PE, while the effect of the clipping is more pronounced for lower night-sky background rates (~ 15% and ~ 8% for 417 and 828 MHz PE respectively).

high values (decreasing the scaling) beyond 30 PE shows no notable difference, as the probability for such high afterpulses is negligible ($< 10^{-7}$). Additional results for higher levels of NSB (up to ~4 GHz PE) are presented in figure 3.29, while the shift of the trigger threshold with increasing NSB for fixed camera readout rates is shown in figure 3.30. Both results show that a clipping of ~8 PE starts to truncate the trigger amplitudes at ~1 GHz PE and a clipping of ~16 PE will show an influence at ~2.5 GHz PE.

3.4.11 Discussion of the Monte-Carlo simulations

The final set of simulation parameter updates had been incorporated into the simulations shown in figures 3.28, 3.29 and 3.30. For all simulations and measurements shown, the `ppmm`-filter and a trigger patch size of 9 pixels have been used. Four scale factors were chosen (34, 48, 96 and 191), and variations of the background illumination for a range of 0-4 GHz PE. The simulations additionally were using the respective 7- and 8-dynode PMT descriptions, namely the pulse shape, afterpulsing spectrum for both cases, and the single photo electron spectrum of the 7-dynode PMT. As the measurements were taken with a flat fielding on the trigger gain, taking the different pulse shape responses of the PMT types into account, the simulations were using different gain values (`fadc_amplitude`) between the 7- and 8- dynode PMT variants. This should in principle yield comparable clipping values when setting the scaling factors (in TLSB).

Comparing the differences between the simulated and the measured camera trigger rates over the studied parameter space, shows an excellent overall agreement. The notable difference in the camera trigger rates in specific regions of the parameter space will be discussed in the following.

Comparing the curves for the 8.0 PE clipping in figure 3.28 with increasing night-sky background rates, a shift in the trigger threshold of $\pm 5\%$ can be observed. While this is an excellent agreement over a broad range of the parameter space, the remaining subtleties will be studied in the following.

The simulations overestimate the camera trigger rates for low illumination levels, as the cut-off due to the clipping sets in earlier in the high illumination region. An overestimation of the camera trigger rate can also be observed for the curves applying the clipping at ~16 PE and ~31 PE in the regime of higher background illumination (828 MHz PE), where the afterpulsing is expected to be less influential. On the other hand, the simulations agree with the measurements in the regime were the afterpulsing is more dominant (NSB rates 417 and 828 MHz PE and > 31 PE clipping).

This effect can be best observed, by comparing the change of the difference of the trigger threshold for the ~16 PE clipping curve with increasing night-sky background rate (cf. figure 3.29в). For low illumination levels, the trigger rate is dominated by the afterpulsing and in good agreement between measurement and simulations, while an increase of the NSB levels leads to a small overestimation

of the trigger rates and finally to the reverse trend between the 2016 MHz PE and 2662 MHz PE simulations, where the clipping value starts to influence the upward fluctuations of the background light distribution.

An additional subtle difference between the 7- and 8-dynode simulations shows up when comparing the camera trigger rates in figure 3.28. The 7-dynode PMT simulations result in a higher camera trigger rate (or higher trigger threshold) than the 8-dynode PMT simulations for low illuminations and high clipping values, while this behaviour switches with increasing NSB rates or lower clipping values (cf. figure 3.28A). As the total afterpulsing probability is higher for the 7-dynode PMTs than the 8-dynode PMTs ($1.2 \cdot 10^{-4}$ compared to $1.0 \cdot 10^{-4}$) the 7-dynode camera trigger rate simulations are expected to exhibit a higher camera trigger rate (or trigger threshold) in a regime where the afterpulsing is dominant. On the other hand, the effective trigger width for the 8-dynode PMTs is larger, expected to lead to higher camera trigger rates, where the night-sky background is dominant. The combination of both influences leads then to the observed switch-over between the camera trigger rates of the 7- and 8-dynode PMT simulations.

The PDP modules in the camera prototype have been installed in alternating patterns aiming for a homogeneous distribution of the PMT types in the camera (cf. A.1). The master trigger patches in the camera consist of patches with either a pure 7- or 8-dynode PMT composition (for the 9-pixel patch trigger setting) and mixed patches, due to the overlap of the trigger sum. If one would assume a perfect Monte-Carlo simulation description of the camera, one would expect the measured trigger rates to follow simulations of both PMT types in their respective dominant regime, while being bounded by the simulations in between. This is only true for parts of the parameter space, where no relevant truncation of the trigger amplitudes (either due to NSB fluctuations or afterpulsing) occurs. The parts of the parameter space where the description starts to deviate represent the extreme regions of the system, where even small uncertainties of the input parameters emerge. In general, the camera is slightly better described by the 7-dynode PMT simulation parameters, although the largest difference between both simulation types and the measured camera trigger rates is on the order of 5% in trigger threshold in the deadtime-free camera readout rates < 20 kHz.

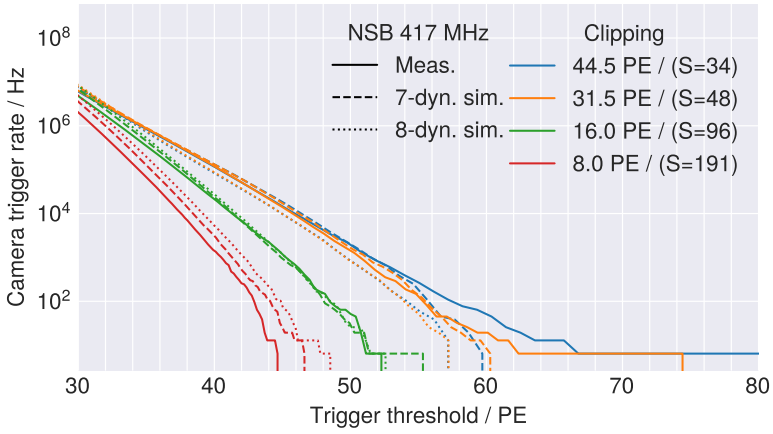

(A)

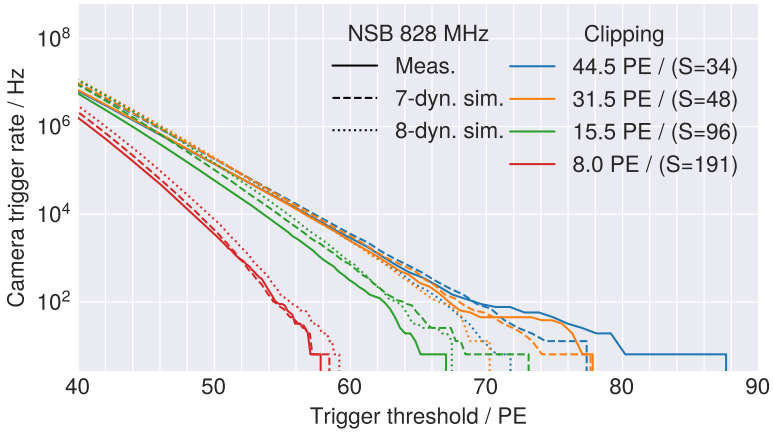

(B)

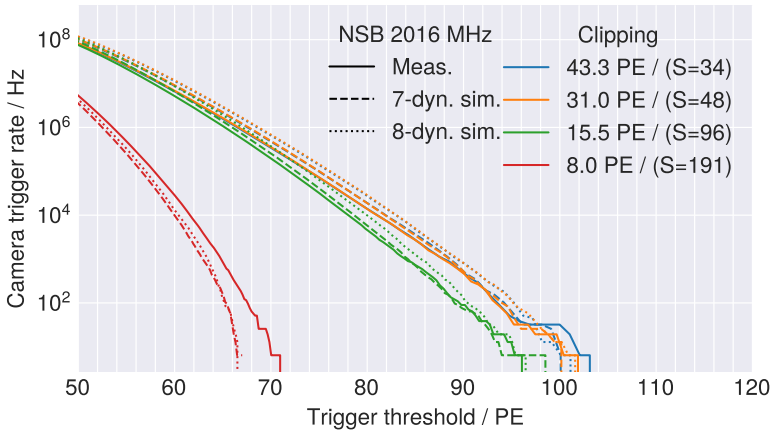

(C)

Figure 3.28: Camera trigger rate measurements and simulations are shown in panel (A)-(C) with increasing levels of background illumination (417-2016 MHz·PE). Trigger rates have been computed for four settings of the scaling parameter. 7- and 8-dynode PMTs were simulated separately and are shown as dashed and dotted lines, while camera measurements are shown in solid line. Trigger threshold for the simulations were converted to PE by applying the trigger gain computed from the `trigger_loss` of their respective pulse shapes, while the measurements were converted by using the trigger gain from the live system calibrations.

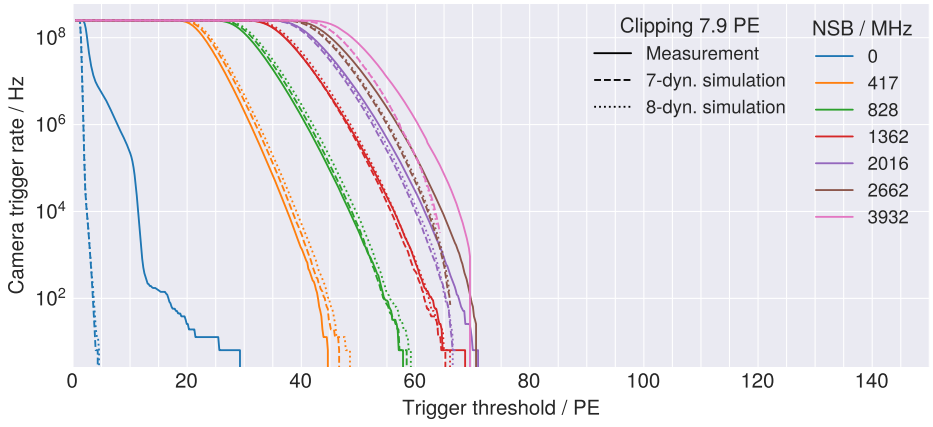

(A)

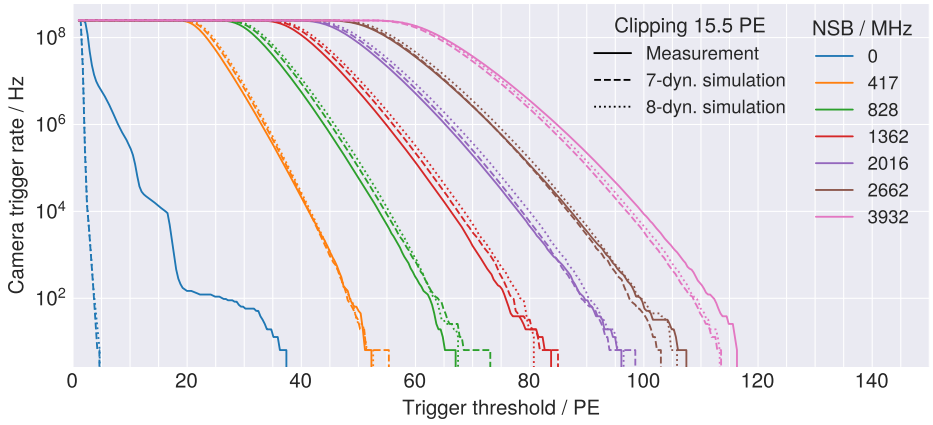

(B)

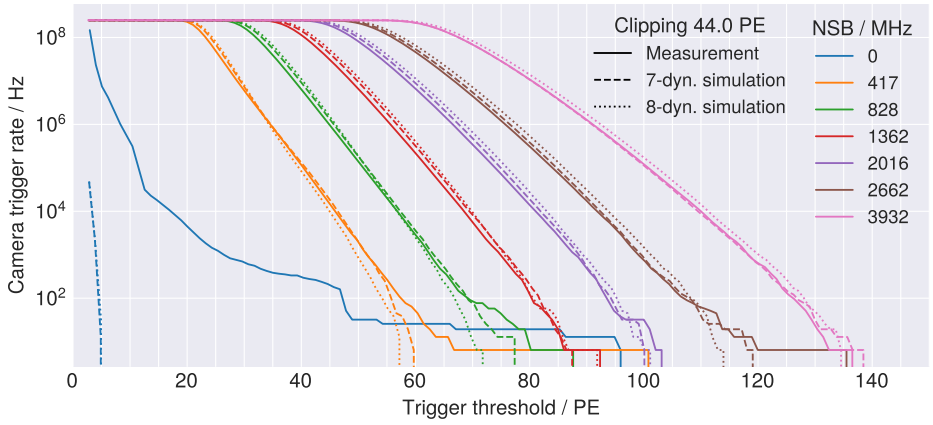

(C)

Figure 3.29: Camera trigger rates computed from measured and simulated data. 7- and 8-dynode PMTs have been simulated separately (dashed and dotted lines), while the measured datasets are shown as solid lines. Panels (A)-(C) show the datasets computed with increasing clipping values (decreasing scaling parameter).

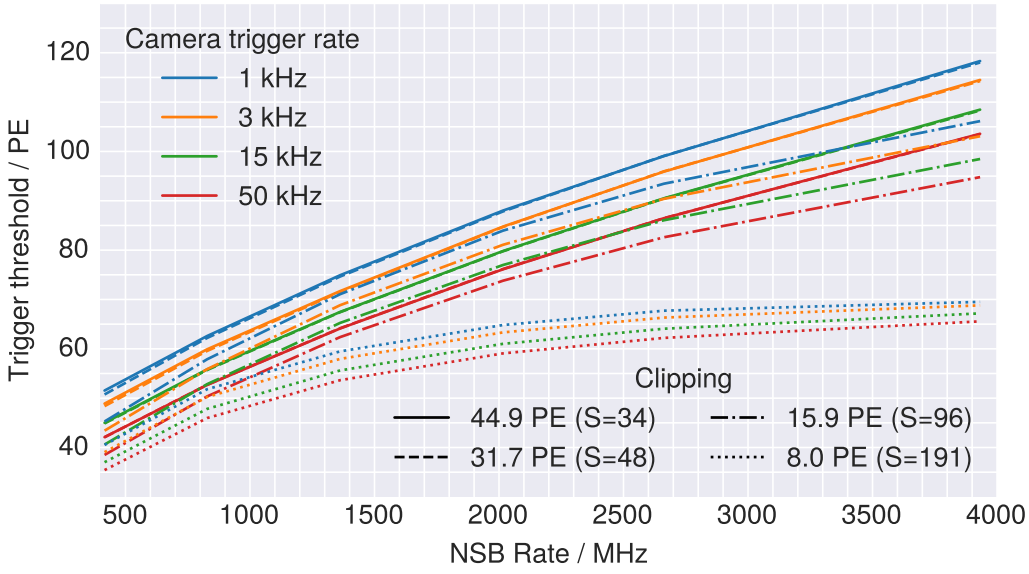

(A)

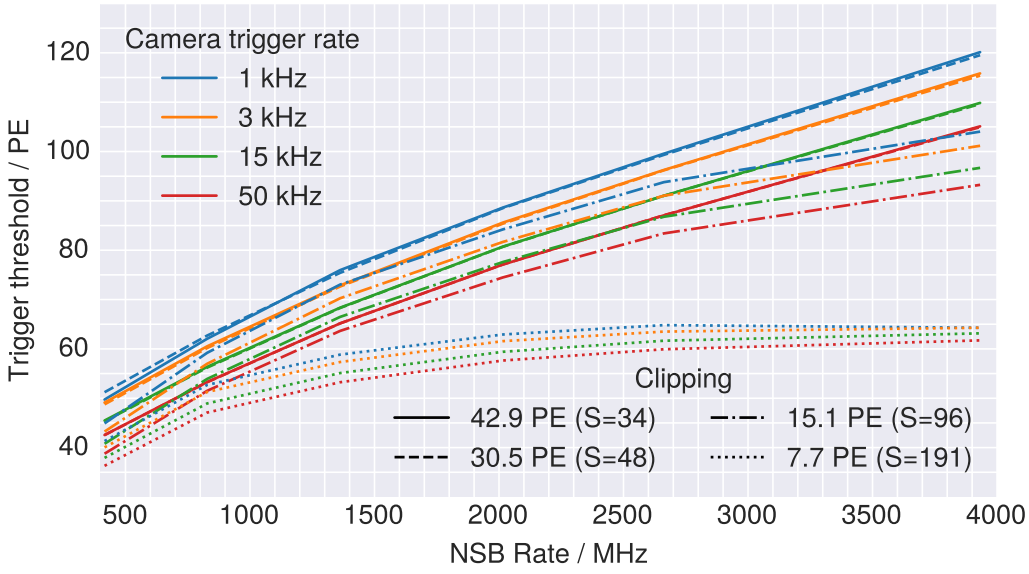

(B)

Figure 3.30: The change of the camera trigger threshold with increasing levels of night-sky background rate are shown for fixed camera trigger rates, for 4 levels of clipping. Panel A shows results from measurements, while panel B shows the results from simulations of 7-dynode PMTs. Clipping values are calculated from the measured trigger gain for the measured datasets, while the clipping values for the simulations use the trigger response values derived from the measured pulse shape.

3.5 Summary & the choice of the trigger settings

This study has shown that the fully-digital trigger system of FlashCam operates as expected and can be successfully emulated using a software implementation of the same logic. It has been shown that the systematic characteristics of the trigger system can be fully understood and applied equally to the Monte-Carlo simulations, demonstrating the advantages over camera systems with a separate analogue trigger path. The largest sources of uncertainty in the description of the camera have been traced back to the description of the photomultiplier tubes.

Comparisons between the charge reconstruction and the trigger signal computation show an excellent agreement within 1% when assuming an average pulse shape for each of the two PMT types. Equally the comparison between the expected trigger threshold and the measured light intensities agrees within 1% with a spread over all camera trigger patches of $< 1.5\%$. The turn-on characteristics of the trigger threshold have been shown to operate close to the Poissonian limit and scale as expected with increasing night-sky background illumination.

The simulation description of the camera and the trigger system have been improved in the context of this work, achieving a similar agreement of 1% in the signal dominated trigger regime, while the accidental camera trigger rates due to the background illumination have shown to exhibit a shift less than 5% in trigger threshold between the simulations and the measurements.

It is worthwhile to note that due to the digital nature of the camera, all advances in understanding the detector response simultaneously improve the description of the trigger as well as the signal reconstruction of air shower images.

The choice of the trigger settings

The results regarding the individual trigger parameters are collected and discussed here with the aim to present a possible strategy regarding the choice of the trigger settings.

Trigger filter The implementation of the four possible trigger filters has been detailed in sec. 2.2, the pulse shape dependent response in sec. 2.5 and the difference between the four variants has been studied using simulated datasets in sec. 3.4.9. The trade-off between the properties of the filters results in a choice between a better trigger amplitude resolution and a worse effective integration window for night-sky background induced trigger signals as well as a wider trigger timing window. As both aspects have been deemed equally important, the middle-ground has been chosen with the `ppmm`-filter, which has the additional averaging effect, compared to the `2pom`-filter.

Size of the trigger patches The influence of the size of the trigger patches has been discussed in section. 3.4.8. A direct consequence of an increased trigger patch

size is the increased collection of additional photoelectrons from the night-sky background into the trigger sum. This shifts the trigger threshold to higher values for the same level of background illumination. Reducing the trigger threshold as low as possible, resulting in a lower energy threshold of the experiment is desirable, which favours a smaller patch size. However, the final decision is dependent on the size and light distribution of the Cherenkov images. Dedicated simulations have been performed using air shower simulations, resulting in the choice of the 9-pixel master trigger patch size as the default. These simulations used a fixed safe threshold close to the night-sky wall for both 9- and 21-pixel trigger patch sizes, and compared the minimum energy of hadronic air showers still detectable at the given trigger threshold.

Scaling / Clipping The scaling parameter turned out to influence a multitude of aspects of the trigger system. The dynamic range of the channel-wise trigger amplitudes is set by this parameter, with special caveats for the low trigger amplitude regime, where the coarse-grained nature of the possible values of the trigger amplitude leads to quantisation effects (cf. section 3.1.2). For the high trigger amplitude regime, the maximum value of each channel leads to a clipping effect, limiting the contribution of each channel to final trigger sum. The clipping is most influential on the contribution of afterpulses, allowing to limit their contribution to the final trigger sum. The influence of the afterpulsing has been discussed with dedicated simulations in section 3.4.6 and the resulting comparison between measurements and simulations, as well as the change of the resulting camera trigger rates, when going from lower night-sky background intensities to more pile-up dominated regimes, have been discussed in section 3.4.10.

The clipping should be set such that one pixel may not trigger a camera readout by itself (e.g. due to an afterpulse and the usual upward fluctuations of the night-sky background), but allowing fluctuations in the individual pixel contributions. Limiting these contributions by setting a low clipping value would in that sense defeat the purpose of a sum trigger, as the light content (due to the limited range) allowed per pixel would act more as a coincidence trigger than a sum trigger. It is this flexibility of the sum trigger regarding the varying shape of the Cherenkov image, which lead to the implementation of the sum trigger in the first place. This implies a clipping value smaller than, but close to the trigger threshold.

Trigger threshold Using the aforementioned settings for the trigger settings, i.e. a scaling factor between 30 and 50 for an average trigger gain of 7.0 TLSB, results in clipping values between ~ 30 and 45 PE. The desired accidental camera trigger rate must be chosen (e.g. 3 kHz) and the trigger threshold set dependent on the worst-case night-sky background conditions one wishes to support (cf. figure 3.30). Due to the steepness of the night-sky wall, additional safe margins on the threshold could be desirable, as the readout rate could be driven beyond its

maximum readout rate by upward fluctuations in the NSB rate. The minimum threshold for an NSB rate of 300 MHz PE (around the nominal night-sky background for a FlashCam-MST at CTA south) would be at ∼45 PE, increasing to ∼55 PE for double the nominal rate and shifting to ∼75 PE for 1.5 GHz PE.

At this stage, practical considerations have to be taken into account. On the one hand, as the observatory operates with an additional array wide trigger, triggered events are handed over to a central trigger system, accepting only coincidences between telescopes and thus filtering the accidental triggers. This allows the cameras to operate closer to the night-sky wall and at a lower threshold.

On the other hand, the data processing and the central trigger system must be able to handle the incoming data rates of the individual cameras safely. Saturating the processing power of the central trigger, due to individual telescopes firing at high trigger rates, would paralyse the whole array of telescopes, rendering the benefits of a lower trigger threshold moot. Additionally, parts of the analysis rely on Monte-Carlo simulations giving accurate results regarding the trigger threshold, e.g. the computation of the effective area of the observatory, which is required to determine the flux of a source. Depending on the desired accuracy of the simulations, this implies dedicated simulations for different levels of night-sky background *and* their respective trigger settings. This parameter space grows quickly, where the extra overhead may prove very time-consuming and costly.

A possible strategy is then to pick a scaling value and a trigger threshold for a range of night-sky background levels for which the camera is operating deadtime free and switching to the respective next set for observation conditions which require a higher trigger threshold.

An additional viable strategy for dealing with high night-sky background observation conditions should be mentioned here. For conditions, where the dynamic range of the channel-wise trigger values is not sufficient and the scaling parameter would need to be set to very low values, the trigger gain could be decreased by reducing the gain (the high voltage) of the photomultiplier tubes itself. This has the additional benefit of reducing the ageing the PMTs due to the reduction in anode currents.

Chapter 4

Fluorescence light detection capabilities

The fluorescence emission of air showers has been successfully used to study cosmic rays cosmic rays incident at earth at energies >10^{17}eV with small (<10m^2) but wide field of view ($\sim 30°$) telescopes. For IACTs, this emission has mostly been regarded as contamination in the detection of the Cherenkov emission. However, the isotropic emission of the fluorescence light and the large mirror sizes of the MSTs planned in CTA bear the potential to extend the detection area of γ-rays beyond the light cone of the Cherenkov emission. The limited field of view of IACTs presents a significant challenge in the detection and reconstruction of the fluorescence emission. In this chapter, the use of multiple telescopes detecting the fluorescence emission of air showers in stereoscopy is studied by using the 25 MST baseline CTA-south observatory telescope array with FlashCam camera mounted telescopes. The digital, reconfigurable trigger system of FlashCam is used to derive a hybrid trigger system, that may detect both the fast Cherenkov light as well as the much slower signatures of fluorescence emission. The aim of a possible trigger system would be to implement a second trigger path parallel to the existing Cherenkov trigger, enabling the detection of slower time signature signals from air showers in a non-disruptive way.

The successful implementation of the trigger logic allows then to the study the effective area the CTA-South MST sub-array would have, using the slow trigger algorithm. The detection power of the fluorescence emission of air showers produced by γ- and hadronic induced air showers above 1 PeV has also been studied, taking into account two pointing strategies. To asses the differential flux sensitivity on PeV γ emitting point sources, a shower axis reconstruction algorithm has been devised, determining an estimate of the angular resolution of the MST array. The simulations used in this work, were produced with the CORSIKA [24] and sim_telarray [8] simulation packages [1].

[1]The fluorescence light emission implementation in CORSIKA was kindly provided by D. Morcuende [47]

4.1 Trigger design & event selection

The design of a trigger algorithm, which is able to detect the isotropic fluorescence emission of air showers has to take the spatial distribution and arrival time structure of the incoming photons into account. The fluorescence photons may arrive over a large time interval (up to $\sim \mu s$) due to the side-on observation of the shower and the variable impact distances still observable (up to $\sim$ km, depending on the energy of the primary particle). Due to the small angular field of view of the FlashCam pixels mounted on an MST (pixel FOV = 0.179°, flat-to-flat), not too distant showers may be visible in more than one pixel along the line of the shower axis. For example, 80% of the lateral spread of a vertical shower with a 5 km impact distance would cover $\sim 1.4°$ of the field of view of a telescope pointing 30° from zenith, resulting in a 7-9 pixels width of the shower detected in the camera. The trigger strategy presented in this work has been developed with the goal to determine the detectable parameter space of the incoming shower observables (energy of the primary particle, impact distance and orientation of the shower axis relative to the array pointing). Compared to the Cherenkov trigger, the photoelectrons of the incoming fluorescence photons are distributed over a much wider time interval (μs) across the camera, despite the fine pixelisation the photon emission of different parts of the shower along the line of sight of a pixel may still be up to hundreds of nanoseconds, mainly because a pixel observes a volumetric slice of the shower development.

Because of the large mismatch between the sampling rate (the natural timebase for the trigger) and the signal time scale, a decimation step is needed to improve the signal-to-noise ratio of the trigger signal. The aim of the design presented here is to increase the signal-to-noise ratio within a channel by using a moving average (named compression in this work) on the raw readout traces, with an compression width optimised for the time structure of the faintest images. The number of photoelectrons detected depends on the primary energy and the distance to the shower core in the FOV of the pixel. An additional correlation between neighbouring pixels within the compression window of the raw sampled traces is needed to increase the SNR to detectable levels. This neighbouring pixel correlation makes use of the same averaging technique, and has been named the smoothing parameter in this work (to distinguish from the compression parameter).

This smoothing takes places along the three major axis of the pixel lines in the camera, averaging the signals in neighbouring pixels at the same time slice.

It shall be noted here, that these averaging operations may not be transferable fully into a firmware trigger design on the ADC and trigger boards of the existing FlashCam hardware (due to limitations of the FPGA). An averaging of the samples within a readout channel is an easily implemented operation (compression), but the correlation of the neighbouring pixels (smoothing) would have to use the existing trigger patch summing technique of the already implemented Cherenkov

trigger.

The combined application of the compression and smooth adds up the detected photoelectrons from photons emitted within a certain volume (depending on the respective width parameters) of the shower and if above a fixed trigger threshold, produces a trigger signal of a master trigger patch. This is the first stage of the proposed trigger logic, which may be implemented in similar form using the ADC and trigger boards of FlashCam.

A second-level trigger to reduce accidental trigger due to night-sky background fluctuations is the detection of the shower track within an appropriate time frame. A minimum number of trigger patches triggering along a line in the camera coordinates would be needed to determine a track direction. In this work, the track detection of the second stage has been implemented by setting requirements on distribution of all triggered pixels in the camera within the simulated time window.

The computational capabilities regarding a track detection algorithm in the firmware of the master card in the FlashCam camera is limited, but a minimum working solution would be, to use a high enough trigger threshold of the first stage triggers so that the readout rate due to accidental triggers would be sufficiently low to allow the track detection to be performed on the readout server of the camera. As will be reported later in section 4.2, a reasonable upper limit on the mono-telescope event trigger rate is ~ 2-3 Hz. The default trace length per event of the readout system would be fixed for both trigger paths and be set according to the requirements of the Cherenkov trigger, but within 20-128 samples. The individual triggers of the master patches due to a shower passing through the field of view would trigger a readout of these shorter events and be merged on the readout server. Assuming a short readout trace length of ~ 20 samples and a long fluorescence event with up to 512 samples (as the "worst-case"), the average trigger rate would be ~ 75 Hz. The FlashCam readout system is able to process event rates up to 20 kHz (or more, depending on the set trace length).

The accidental trigger rate of the first stage is determined by the number of pixels above the threshold within each simulated event. With a trigger threshold leading to a mean of one per ~ 2 μs, this requires an additional selection criterion in the camera hardware, which can be addressed with a simple gating technique, with the gate width set by the maximal expected time a track is visible within the camera field of view (<1μs). Assuming a minimum number of 5 pixels within 256 samples to trigger a camera readout the expected accidental trigger rate amounts to ~ 14 Hz. This reduction of first level triggers is addressed by the second stage implementation in this work.

4.1.1 Algorithm

The reconstruction algorithm implemented in the `fc-utils` fluorescence event reconstruction consists of two stages, which could be comparably mapped to the capabilities of FlashCam hardware with a combination of the camera trigger system and a second stage using the readout server. A short overview of the individual steps of the algorithm are given here, where the first stage works on the raw sampled traced of the camera, while the second stage is applied to the already reconstructed peaks of the read out camera traces. An overview of the individual steps of the algorithm are given in the following.

First stage - raw trace processing

Simple moving average The shaping filter in the reconstruction implementation is a simple moving average applied two times, forwards and backwards on the the channel readout trace to cancel phase delays, with variable number of total applications (in this work, always set to two) and variable width w. The algorithm computes the moving average with a shift of w of the samples in the index of the input array on the forward application and again with the same shift on the backwards application, leaving the centroid of the trace at the same sample. The following equation details the iterative steps, with i starting from 0 up to $n-w-1$ and n the total number of samples.

$$y_i = y_{i+w} + \frac{x_{i+w} - x_i}{w} \text{ with } i \in [w, n] \tag{4.1}$$

This leaves the edges of the input array unprocessed and would result in an output array of size $n - 2 \cdot w$. The implementation used in this work applies a linear interpolation to the sample values between the left edge of the output array and the average of the $w - 1$ unprocessed samples of the input array.

$$y_i = S - (S + y_w)\frac{i}{w} \text{ with } i \in [0, w-1] \text{ and } S = \sum_{i=0}^{w-1} \frac{x_i}{w} \tag{4.2}$$

The right edge is treated similarly with inverted indices in the above equation. Compared to other methods like zero-padding the input, ringing effects are reduced by the linear interpolation.

Compression - time component To increase the signal-to-noise ratio (SNR) of the read out traces, the simple moving average is applied to each readout channel (pixel). To distinguish the operation from the hexagonal smoothing, this variable parameter in the image reconstruction has been named the compression parameter. The default as the optimal parameter for this reconstruction method with a width parameter $w = 14$ samples (56 ns).

Hexagonal smoothing - spatial component The spatial smoothing makes use of the hexagonal layout of the pixels in FlashCam by defining a hexagonal coordinate system, which defines three axes orthogonal to the rows of edge connected pixels. This allows the application of the moving average along each line of pixels, for all three directions, resulting in a symmetric smoothing, leaving the centroid of the image intact. The moving average is applied with a width w of 2 pixels along each line of pixels. This is performed for each sample of the already compressed event.

The trigger threshold The compressed and smoothed readout traces are subjected to a threshold and all local maxima above said threshold are counted as triggers (later also used as reconstructed peaks, with a corresponding amplitude and time). The threshold used for the peak search has been determined relative to the noise level of the compressed and smoothed images, as the threshold in hardware units (LSB) depends on values of both parameters. The minimum possible pixel threshold determined in this work has been found to at $4.5\,\sigma_{\mathrm{noise}}$.

Second stage - image selection

Principal component analysis A principal component analysis (PCA [35]) of the spatial distribution of the reconstructed peaks in the camera coordinate system has been used to find a track like object from the reconstructed peaks. The algorithm determines the axis of maximal variance of the spatial peak distribution, resulting in a *length* and a *width* of the distribution (the standard deviation along the major and minor axis) [2]. The data points used in the PCA are weighted with the amplitude of the reconstructed peaks, decreasing the influence of low amplitude outliers. As the PCA does not take the time structure of the reconstructed peaks into account (distributed within hundreds of time samples) additional selection criteria on the distribution of the peaks have been set.

1. criterion: A minimum of 15 pixels inside the rectangular area spanned by the length and width of the PCA components are required. This sets a minimum on the size of the image.

2. criterion: A minimum of 50% of the pixels inside the rectangular area must contain a reconstructed peak (containment ratio of 0.5). This ensures a minimum compactness of the image, as the second stage does not account for the time structure and far away individual accidental triggers result in a large size of the rectangular area spanned by the PCA components (which is not selected against by the first requirement).

[2] This is similar to the Hillas reconstruction technique used in the reconstruction of Cherenkov images [27].

4.1.2 Determination of the trigger parameters

The aim in determining the optimal trigger parameter settings was to avoid a significant trigger rate due to accidental night-sky background, as the fluorescence trigger mode is envisioned to run in parallel to the fast Cherenkov trigger and should not impede the normal operation. The presented parameters of the trigger algorithm have been determined by application of the trigger logic to events from a simulated dataset using 1000 unique 10 PeV γ-ray induced air showers[3], with a repetition parameter of 10 (CSCAT in CORSIKA), distributing the same simulated air showers 10 times uniformly over the simulated area. The simulated area was $5\,\mathrm{km} \cdot 3\,\mathrm{km}$ with the centre of the rectangular simulation area 3 km away from the centre of the array (25 telescopes), and the longer edge of the simulation area along the pointing direction of the array. The directions of the incoming primary particles were distributed equally over the sky-dome spanning shower zenith angles between 0° and 60°.

The fluorescence emission from each air shower, was processed with 11 separate telescope pointings with zenith angles between $0°$ and $60°$ (and fixed azimuth angle) and no night-sky background [4].

Additional night-sky background simulations with 300 MHz PE/pixel were performed producing the same number of events and therefore noise traces as the signal simulations. The trace length in both set-ups was 512 samples (2.048 μs), chosen such that the resulting photoelectron distribution would be contained within the simulated time frame and the `FAKE_TRIGGER` parameter was used in sim_telarray, such that a single photoelectron would already trigger a readout.

The traces from the night-sky background simulations were then added to signal traces, producing the final signal dataset. The initial separate simulation of signal and background allows the exact comparison and determination of the signal response compared to the noise response of the trigger. For the purpose of this study, the individual telescopes were treated as independent, as the aim was to determine the trigger parameters on a camera level.

Results - first stage The compression parameter was scanned between values of 2 and 20 in steps of 2 samples and the trigger threshold in steps of 0.5 σ_{noise} between 0 and 10. The trigger threshold is expressed in units of background noise levels, due to the change of the pulse heights of the reconstructed pulses in absolute hardware units (LSB) with changing compression and smoothing parameter.

[3] Initial studies during the development of the trigger logic had shown that 10 PeV γ-rays provided a safe minimum energy to fine-tune the trigger settings. The achievable minimum trigger threshold for a spectrum of simulated shower energies is presented in sec. 4.2 later in this chapter.

[4] A similar set-up but with more optimised boundaries is described in more detail in sec. 4.2 on the effective area. The relevant property of the dataset used here to determine the trigger parameters is the good coverage of image variations of the air showers (due to the finely spaced telescope zenith angles).

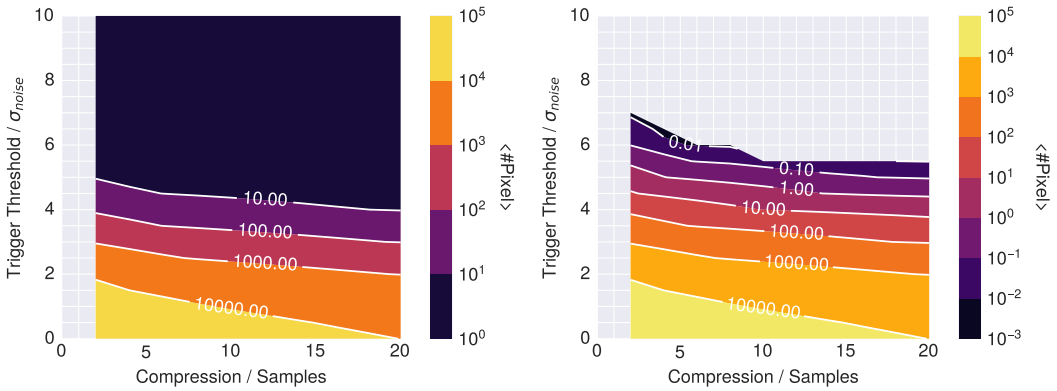

(A) Mean number of pixels above the threshold of all triggered events in the signal+background dataset.

(B) Mean number of pixels above the threshold of all triggered events in the pure background dataset (300 MHz PE).

Figure 4.1: Comparison of the mean image size (number of pixels above the threshold) of the pure night-sky background (300 MHz PE) dataset and a dataset using fluorescence emission of 10 PeV γ added to the same background dataset. The average number of pixels (per event) above the threshold are shown as a function of the compression parameter and the trigger threshold.

Figure 4.1A shows the average number of pixels above the threshold as a function of the compression parameter and trigger threshold of the signal dataset, while figure 4.1B shows the same parameter space for the background dataset. The background subtracted trigger regime is shown in figure 4.2, where all events of the signal dataset which had also triggered in the background dataset have been discarded as false positives. The optimum value in the scanned parameter region for a background-free trigger settings within the uncertainty of the number of simulated noise events has been estimated at a compression parameter of 14, and a trigger threshold of 4.5 σ_{noise} noise equivalent units. The largest average number of pixels per 10 PeV shower above the threshold is ~ 6.5. The hexagonal smoothing width has been determined to 2. The variations of this parameter showed, that no smoothing shifted the trigger threshold to such high levels, no suitable compression parameter could be found, while a smoothing of ≥ 3 reduced the valid range of the trigger thresholds to a very small range dynamic range in hardware units (LSB) under the requirement of suppressed accidental trigger rates ~ 1 Hz.

Results - second stage An additional scan of the parameter space with reduced variation of the compression parameter (between 12 and 18 in steps of 2) has been performed, using the full trigger logic with a minimum PCA region size of 15 pixels and a containment ratio of 0.5 (half of the pixels inside the PCA region must contain a peak above threshold). The fraction of true triggered events (without background contamination) as a function of compression and trigger threshold is shown in figure 4.3A. The maximum could also be found at $\sim 4.5\ \sigma_{\mathrm{noise}}$ and compression 14. The trigger fraction decreases with lower threshold and lower compression due to the increase in background induced triggers.

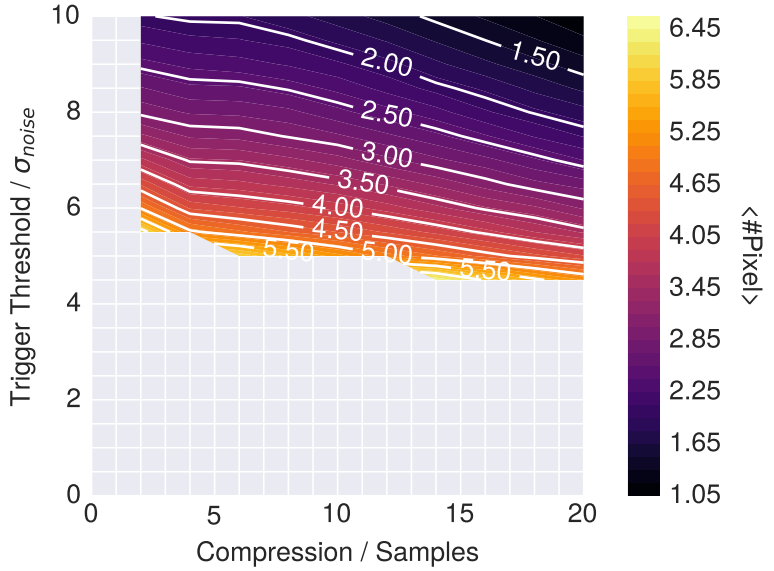

Figure 4.2: The average image sizes of true positive events are shown as a function of the compression parameter and trigger threshold. The point with the lowest trigger threshold and largest image size can be observed at a compression of 14 samples and a trigger threshold of 4.5 σ_{noise}.

The background trigger fraction has has been used to compute the average expected background trigger rates (fig.4.3B). The expected trigger rate due to accidental triggers for the default settings (compression 14, trigger threshold 4.5 σ_{noise}) is $\sim 1\,\mathrm{Hz}$. This is an acceptable level, considering that no stereoscopic trigger requirement has been set yet. The trigger rate was determined by counting any event with any pixel above the threshold as triggered within the full time interval of all simulated events (5.632 s). This assumes that no two triggers occur with the same 512 samples of an event, which is a valid assumption in this low trigger rate regime.

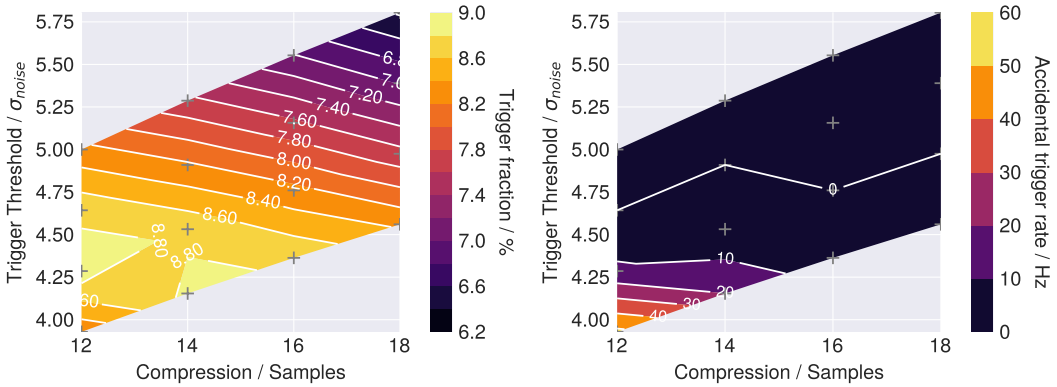

(A) Fraction of true positive events (trigger fraction) as a function of compression and trigger threshold. The trigger fraction shown is the average over all telescope zenith angle simulations (10° - 60° in steps of 5°) each with 10,000 events, of the 10 PeV γ-ray array simulations.

(B) Accidental telescope trigger rate estimate due to fluctuations of the night-sky background as a function of the compression and the trigger threshold. The trigger rate has been estimated from the pure night-sky background dataset with a total simulated time of 5.632 seconds.

Figure 4.3: Trigger fraction of true triggered events and accidental trigger rates due to night-sky background at 300 MHz PE. The grey markers show the parameter combinations with which the reconstruction was performed, while the contour bands show the interpolation in between.

4.1.3 Triggered images

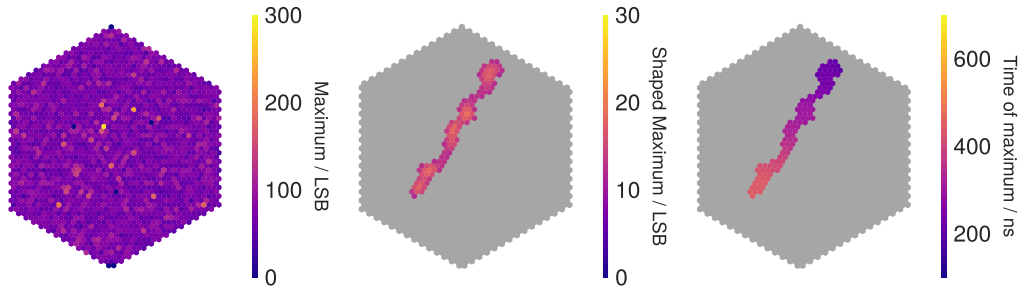

(A) Telescope 13 (X = 0m, Y = 325m) pointing at azimuth 0°, zenith 30°

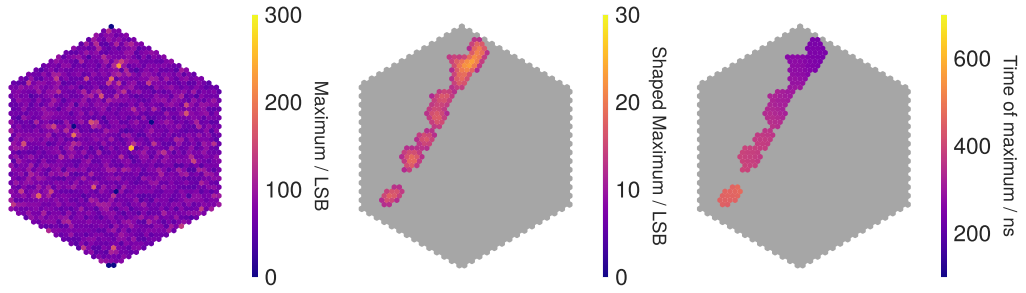

(B) Telescope 19 (X = 291m, Y = 450m) pointing at azimuth 0°, zenith 30°

Figure 4.4: Exemplary camera images of the fluorescence emission of a simulated γ shower seen in two telescopes with primary energy at 3 PeV, the direction of origin from azimuth 107°, zenith 19° and an impact point at 1.3km north and 1.0km west of the array centre. The left panel shows the maximum in each channel in the simulated time interval of 512 samples (2048 ns). The middle panel shows the triggered and reconstructed peak amplitudes after application of the compression and hexagonal smoothing. The right panel shows the reconstructed time of maximum of the peaks.

To highlight the capabilities of the trigger system, two triggered events are presented here. The first is a $\sim$3 PeV γ-ray shower with an impact distance to the telescope array of $\sim$1.6 km coming from East and a $\sim$19° angle from zenith (cf. fig 4.4). The event is seen in three telescopes, of which two are shown here.

The second a $\sim$23 PeV γ-ray shower coming from South-West, behind the telescope pointing direction (cf. fig. 4.5). The events have been taken as examples from a dataset, with similar simulation boundaries as described before, but using 3000 unique events of γ-induced air showers with an energy spectrum of E^{-1}. The left panels of all three images show the maximum of each pixel within the event length. For the high energy shower (20 PeV) pixel-wise peak search does find already enough bright pixels, demonstrating that the smoothing (in space) used in the first stage is mainly needed in the low energy regime. The middle panels show the reconstructed peak amplitudes and the right panels show the arrival time from the start of the event sampling. The time of arrival in the events with smaller impact distance spans an interval of $\sim$400-500 ns, while the shower

impacting further away (but inclined towards the telescope) shows a time span of ~600 ns.

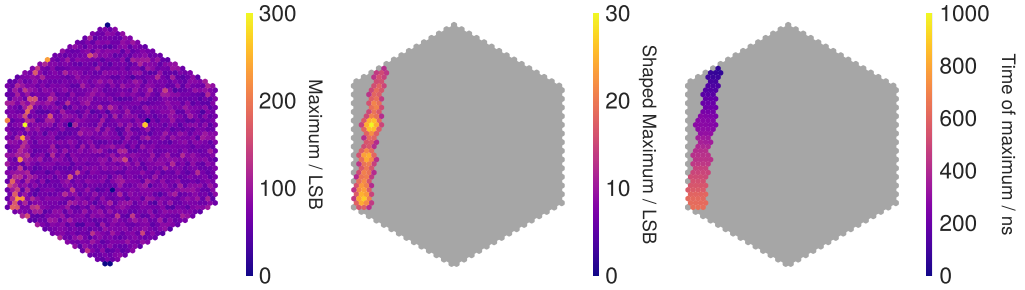

Figure 4.5: Exemplary camera image of the central array telescope of the fluorescence emission of a simulated γ shower (primary energy at 23.7 PeV, the direction of origin from azimuth 165.7°, zenith 18.2° and an impact distance 3535m). The left panel shows the maximum in each channel in the simulated time interval of 512 samples (2048 ns). The middle panel shows the triggered and reconstructed peak amplitudes after application of the compression and hexagonal smoothing. The right panel shows the reconstructed time of maximum of the peaks.

4.2 Effective area & Differential trigger rate

Simulation set-up

The simulation set-up to determine the capability of the 25 MST sub-array of the CTA-South observatory to trigger on the fluorescence photons of air showers will be described in this section. The simulation chain to produce the camera ADC sample traces is comprised of the CORSIKA simulation package using the fluorescence emission implementation and generating the fluorescence photons emitted from the air showers. Sim_telarray traces these photons to each telescope's mirrors and camera, where the full detector simulation takes place. Additionally, the night-sky background is simulated within sim_telarray with a homogeneous distribution over the camera. In this study, a night-sky background rate of 300 MHz PE / pixel has been assumed.

The parameter space of the simulated air showers spanned four primary particle types (γ, proton, nitrogen and iron) and an energy range between 1 PeV and 100 PeV with an E^{-1} spectrum. These showers were distributed randomly across a 5 x 5 km square area (with the edges aligned to the geographic North and West). The directions of origin of all showers were distributed equally over the sky-dome up to a zenith angle of 60° and 360° in azimuth angle. The centre of the telescope array (using the default CTA layout) was placed at the centre of the southern edge of the simulated area (cf. fig 4.8).

For each of the four primary particles, a dataset was simulated producing 8000 unique events. The CSCAT parameter available in CORSIKA was also used and set to 20, randomly distributing the position of 20 simulated arrays within a given range (in this case −2500-2500 m along both coordinate axes) per simulated

unique shower. This reuse of the simulated shower increases the number of events analysed per dataset to 160,000. This simulation strategy reduces the computational effort significantly, although care has to be taken, as using not enough unique events compared to the reuse parameter may introduce statistical artefacts in the direction of origin.

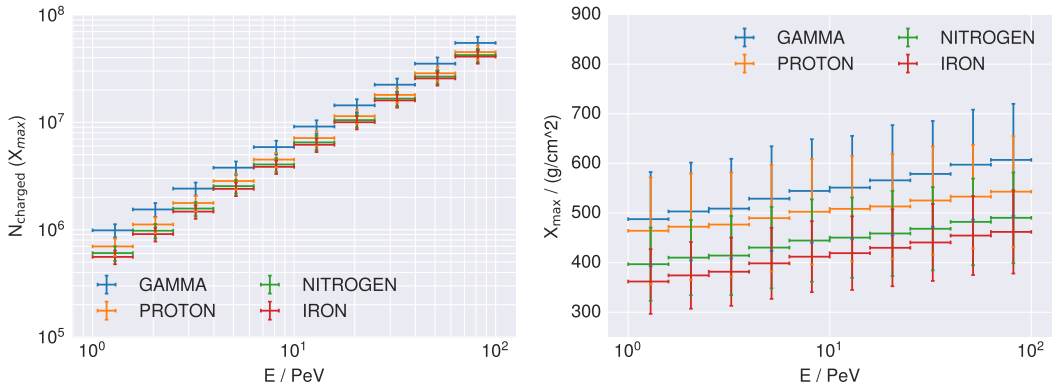

(A) Maximum number of charged particles in the shower

(B) Atmospheric depth of shower maximum as a function of primary energy.

Figure 4.6: The data points show the average of the simulated dataset, with the width set by a binning in primary energy. The vertical error bar shows the standard deviation of the the distribution in each bin.

Due to the large number of charged particles (cf fig.4.6A) in the shower the THIN option of the CORSIKA package has been activated, with a value of $\epsilon_{\mathrm{th}} = 10^{-7}$, with $\epsilon_{\mathrm{th}} = E/E_0$ defining a cut-off energy E relative to the energy of the primary particle E_0. Secondary particles produced in an interaction in the shower development, where the total sum of their energies is below this cut-off energy, are dropped from the shower simulation except one of these secondaries, which is selected at random and given an appropriate weight [5]. The value of the thinning option has been tested between $\epsilon = 10^{-8}$ and $\epsilon = 10^{-6}$ by using a reference shower simulated with the same seeds of the Monte-Carlo state, cross-checking the distribution of the detected photoelectrons in the camera images, showing that any higher levels of thinning than 10^{-7} exhibit a significant change in the image shape and distribution of detected photoelectrons.

Telescope pointing Two pointing strategies have been used in this study, a parallel and a divergent pointing mode. In simulations using the parallel pointing, all telescopes were pointing towards north with four telescope zenith angle settings between 20° and 50° in steps of 10° (cf. fig. 4.7A).

The divergent pointing strategy uses a convergence point of all telescope pointings to determined the orientation of the individual telescopes. This point was set 1 km behind the central telescope (below the observation level) and the pointing vectors of all other telescopes were adjusted accordingly (cf. fig. 4.7B). The mean

[5] Additional information can be found in the CORSIKA manual [10] and [38]

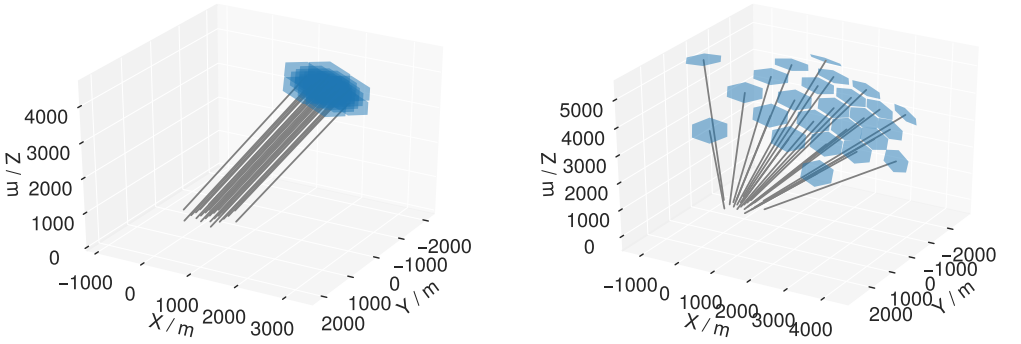

(A) Parallel pointing at array zenith 30°. **(B)** Divergent pointing at array zenith 30°.

Figure 4.7: Exemplary pointing strategies of the telescope array. The grey lines show the vector of the camera centre projected to the sky with a length of 5 km, while the blue hexagons (flat-to-flat radius of 1.5 m in the camera) show the projected field of view of the individual telescopes at that distance.

angular separation in divergent pointing mode between the central telescope pointing and the other telescopes is ∼ 17° with the maximum up to ∼ 35°. The average angular separation between each telescope and its three closest neighbours is ∼ 10°.

Due to the different individual orientations of the telescopes in the divergent pointing mode the overall pointing direction of the central telescope is referred to as the array pointing in the following, as it determines the pointing of the array. The array pointing in the simulations using the divergent pointing have also bin varied between 20° and 50° in steps of 10°.

Detection probability - geometry

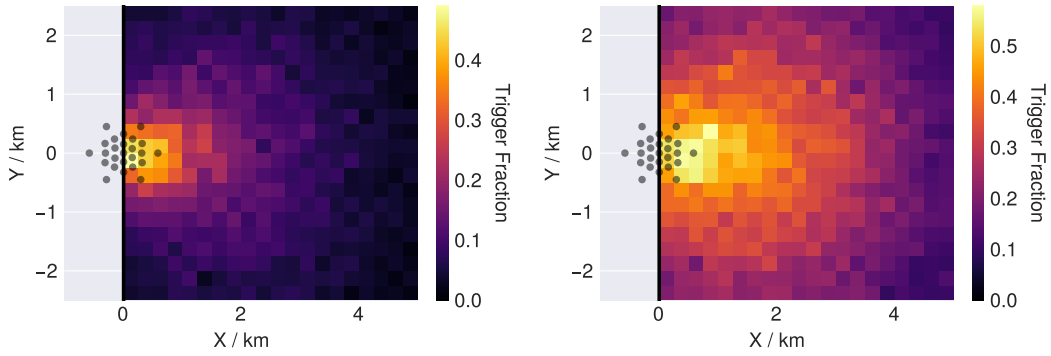

(A) Parallel pointing, array zenith 30°. **(B)** Divergent pointing, array zenith 30°.

Figure 4.8: Triggered showers in detector level plane (primary γ). The black boxes are the boundaries of the simulated area, with X pointing towards North and Y pointing West. The simulation boundaries cover a range of 0 m to 5000 m and −2500 m to 2500 m, resulting in an area of 25 km^2. The 2-D histogram shows the detected fraction of showers in each bin. The grey circles represent the CTA MSTs with mounted FlashCam cameras pointing towards North with a zenith angle of 30°. A telescope multiplicity of 1 to trigger a detection was required.

The trigger algorithm detailed in section 4.1.1 has been applied to the previously described datasets (with variations on the primary particle, array pointing and pointing mode) to determine the detection power in the simulated primary energy range (1-100 PeV). The fraction of triggered events as a function of impact position in the simulated area is shown in figure 4.8 for the divergent and parallel pointings, a γ primary particle and a 30° array zenith angle. The impact distance dependence on the energy of the primary particle is shown in figure 4.9. Both figures show the results with a minimum of one telescope contributing to the trigger decision, the primary particle with the highest trigger fraction over all and a 30° array zenith angle, highlighting the maximum of the achievable detection probability. A clear dependence of the detectable impact distance on the energy of the primary can be observed. Figures 4.8B and 4.9B show that the chosen simulation area truncates the achievable maximum impact distance for the high energy bins (> 30 PeV).

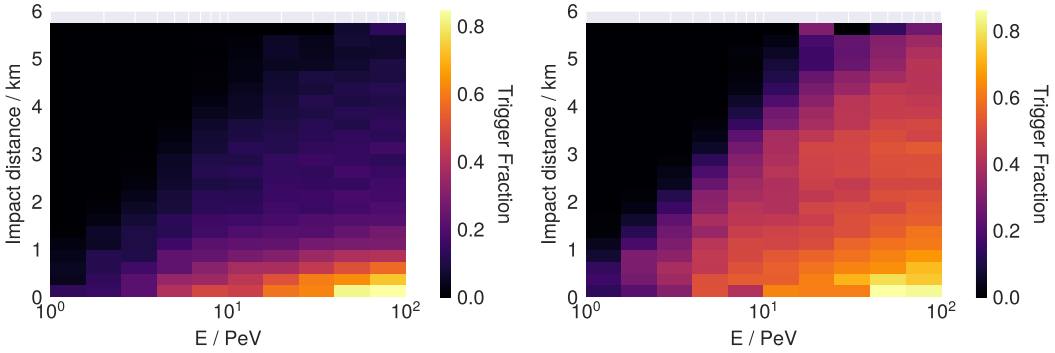

(A) Parallel pointing, array zenith 30°.

(B) Divergent pointing, array zenith 30°.

Figure 4.9: Triggered showers as function of primary energy and impact distance to the array centre. The 2-D Histogram shows the detected fraction of γ showers in mono trigger mode in each bin.

The detection probability as a function of shower azimuth and shower zenith angle is shown in figure 4.10. The parallel pointing mode shows an overall smaller achievable trigger fraction, and a "dead-zone" below the field of view of the telescopes. The divergent pointing mode shows a higher achievable trigger fraction, and due to the spread of the telescopes no large-scale preference in shower azimuth angle.

Detection probability - primary energy & telescope multiplicity

The mean detection probability (trigger fraction) as a function of the primary energy are reported in figure 4.11 for the four simulated particle types, both pointing modes and mono- or stereo-trigger requirements. Restricting the trigger requirement to stereo-trigger in the parallel pointing mode reduced the overall trigger fraction by ∼30%, while the divergent mode trigger fractions drop by a factor ∼1.5 - 3. The increase in detection probability when switching from parallel to

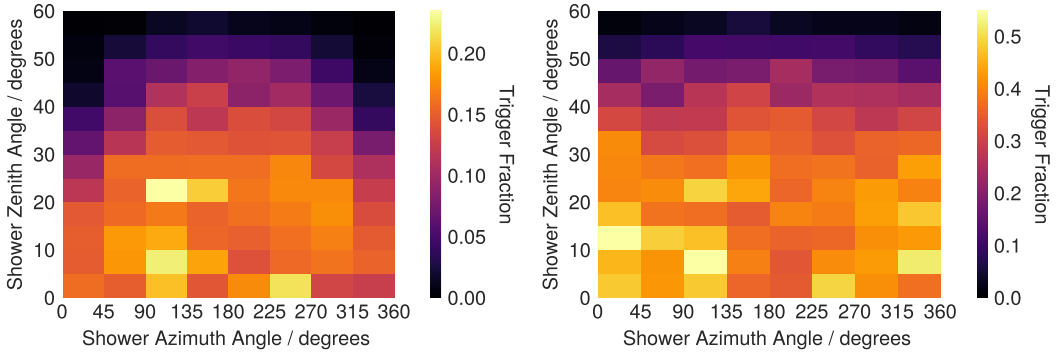

(A) Parallel pointing, array zenith 30°.

(B) Divergent pointing, array zenith 30°.

Figure 4.10: Triggered showers as function of the shower azimuth and zenith angle. The 2-D Histogram shows the detected fraction of γ showers in mono trigger mode in each bin.

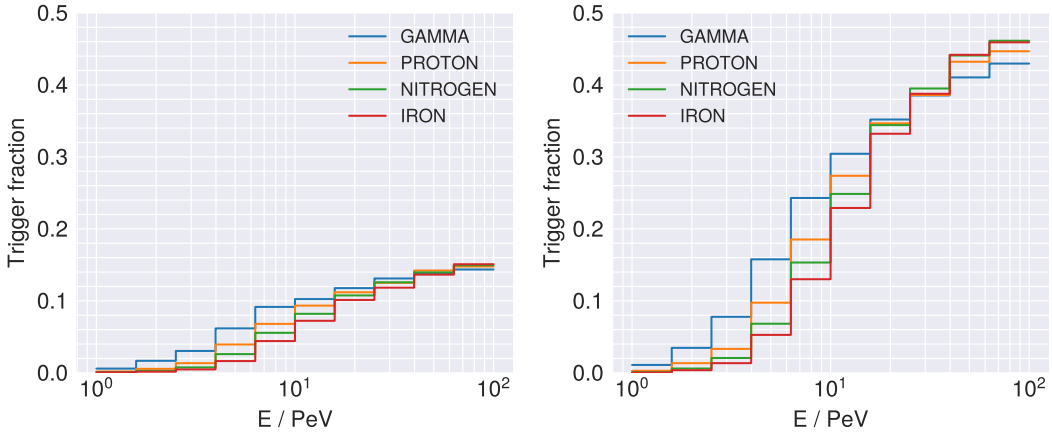

(A) Parallel pointing, minimum mono trigger.

(B) Divergent pointing, minimum mono trigger.

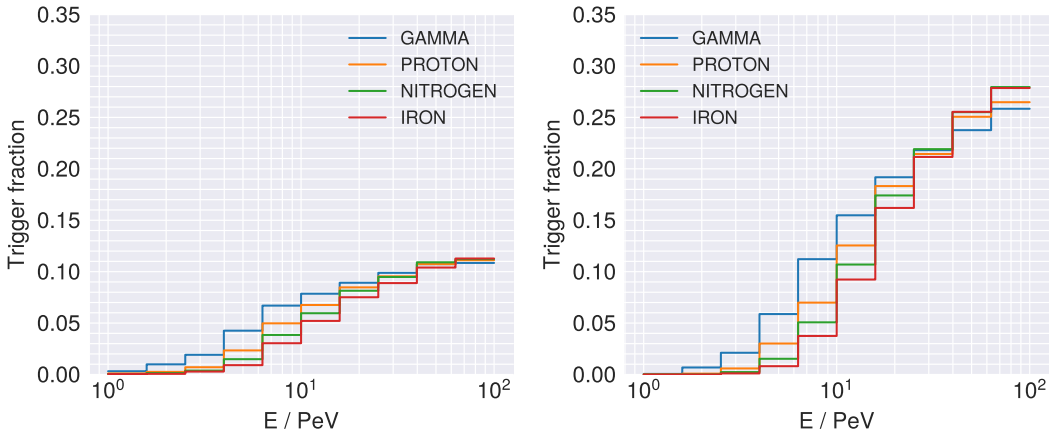

(C) Parallel pointing, minimum stereo trigger.

(D) Divergent pointing, minimum stereo trigger.

Figure 4.11: Trigger fraction (detection probability) for different primary particle types binned by energy. The fraction of detected showers is normalised per energy bin to the total number of simulated showers within that energy bin. The trigger fractions show the average over the four simulated array zenith angles and the full sky-dome up to 60° shower zenith angle. (Note the difference in y-axis scale between the upper and lower row of figures.)

divergent pointing mode (stereo) shows a noticeable increase at ∼5 PeV with a factor of ∼2 and a factor of ∼2.5 for the highest energy bin. γ-showers show an overall higher detection probability due to the larger transfer of primary energy into fluorescence-inducing secondaries and the more compact lateral secondary distribution.

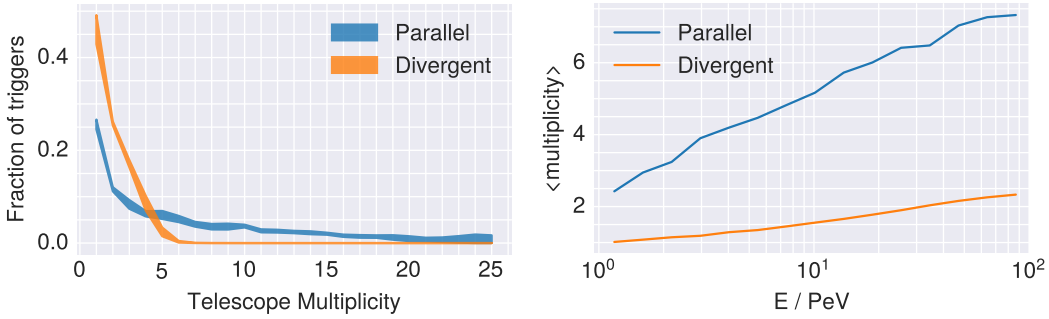

(A) The fraction of triggers as a function telescope multiplicity. The bands show the minimum and maximum values.

(B) Average telescope multiplicity as a function of primary energy.

Figure 4.12: The shown comparisons incorporate four simulations of γ, proton, nitrogen and iron primaries and four array zenith angles (20°-50°) each.

The difference in fraction of triggers as function of the trigger multiplicity between both pointing strategies is presented in figure 4.12A. The divergent pointing mode exhibits a factor of ∼2 larger fraction of triggers in the range between 1 - 3 telescopes taking part in the detection, while the crossover takes place at a multiplicity of 4, where the fraction of triggers in the divergent mode decreases rapidly. The distribution of telescope multiplicities in the parallel pointing mode is much broader, even detecting events where all telescopes participate. Figure 4.12B shows the average multiplicity of triggered events as a function of the primary energy. The very high energy showers are seen in many, if not all, telescopes in the parallel pointing mode.

Angular distribution of triggered events

The distribution of triggered events depending on the orientation of the primary particle in relation to the array pointing is shown as functions of the viewing angle [6] α, the relative azimuth angle ϕ, and the relative zenith angle β (cf. fig 4.13,4.14,4.15). The distributions show the relative fraction of the number of triggered events in minimum stereoscopic trigger mode and with a parallel pointed telescope array for three low energy bins in the 1 to 25 PeV range and the overall distribution up to 100 PeV (averaging over all four simulated primary particle types) [7].

[6] Viewing angle α is defined as the angle between the array pointing and the inverse shower vector, i.e. $\alpha = 0°$ is a shower coming directly towards the telescope and $\alpha = 180°$ would be a shower developing along the line of sight of a telescope.

[7] The distributions of the divergent pointing mode are given in appendix B (figures B.3)

The overall peak of the viewing angle dependence for all simulated energies and array pointings is at ~40° offset, getting smaller with reduced energy with the peak in the lowest energy bin (1-4 PeV) at ~10-15°. The maximum detected viewing angle offset increases from ~45° to ~90° from the lowest energies to the highest energies, increasing the sky coverage considerably. Using the divergent pointing mode, the distributions widen, shifting the peak offset by up to 10° (in the lowest energy bins).

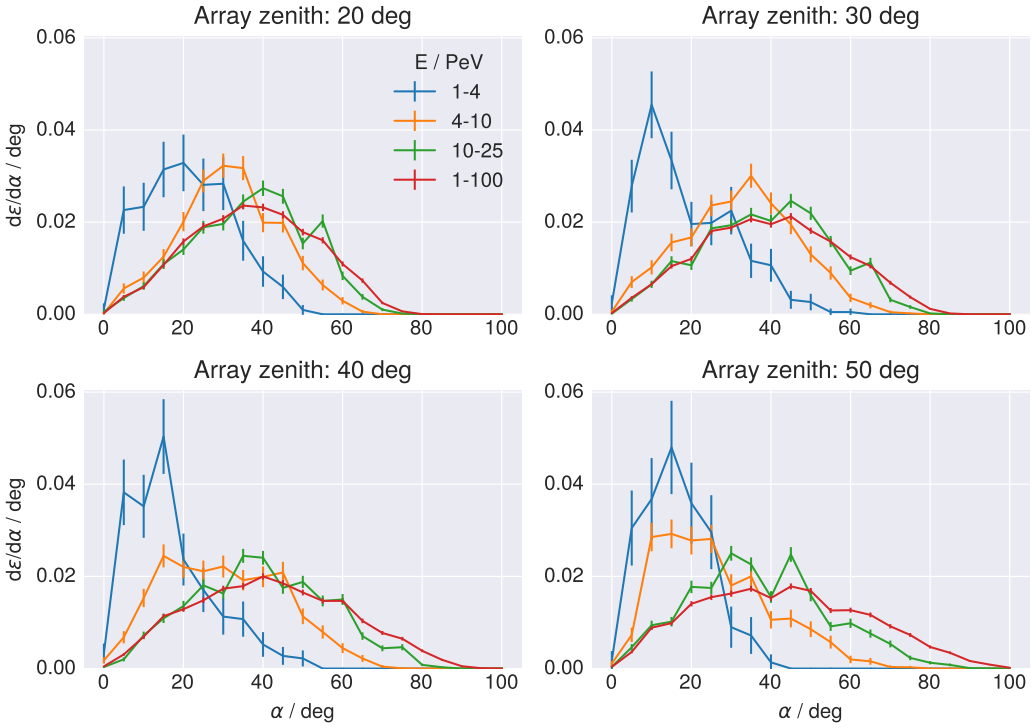

Figure 4.13: Differential fraction $d\epsilon/d\alpha$ of triggered events as a function of the viewing angle α between the air showers and the central telescope for four pointings of the telescope array in parallel pointing mode. The dataset shown contains all four primary particle types and is binned into 4 levels of primary energy. The fractions shown are normalised to the total number of events within each energy bin. A stereoscopic trigger condition was required.

The fraction of triggered events as a function of the relative azimuth angle ϕ between the telescope pointing direction and the azimuth angle of the incoming shower is shown in figure 4.14. The detected showers in the lowest energy bin are originating mostly from an azimuth offset $<45°$ and peaking at 0° relative azimuth for array zenith angles below 20°. For high array pointings (low array zenith) and higher energy bins, the behaviour inverts with the peak at 180° relative azimuth (behind the telescope array) but with an overall more homogeneous distribution, consistent with the wider distribution of the viewing angles. For very low array pointing directions (array zenith 50°), all distributions contract around the telescope pointing direction, due to the lower fraction of triggers for high viewing angles (>50°) and the overall lower fraction of triggers for showers with zenith angle >50%.

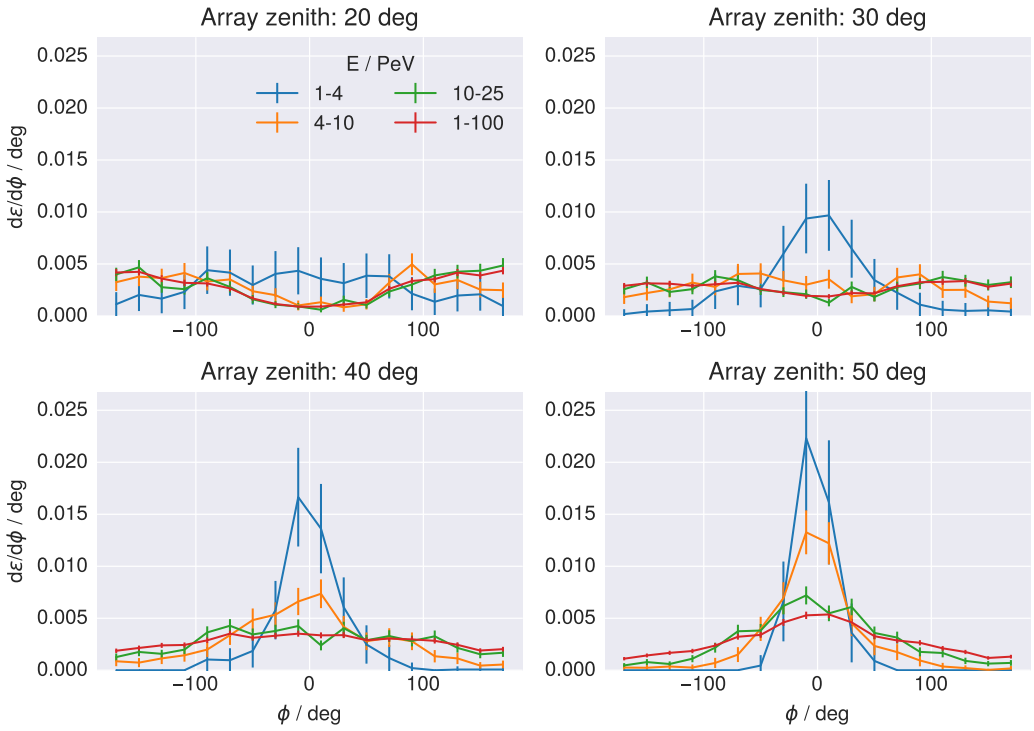

Figure 4.14: Differential fraction $d\epsilon/d\phi$ of triggered events as a function of relative azimuth angle ϕ of the air showers and the telescope array (pointing North) for four pointings of the telescope array in parallel pointing mode. Showers incident from North have a relative azimuth angle of 0, while showers coming from behind the array field of view. The dataset shown contains all four primary particle types and is binned into 4 levels of primary energy. The fractions shown are normalised to the total number of events within each energy bin. A stereoscopic trigger condition was required.

The dependence of the fraction of triggers distribution on the relative shower zenith angles (cf fig. 4.15) shows that the bulk of the triggered events in the low energy bin originate from $\pm 15°$ for high array pointings. For increasing lower altitude pointings (higher zenith) the distributions shift to a higher relative zenith angle β consistent with the overall higher detection fraction for vertical showers. Higher primary energies widen these distributions and detected more showers from a larger zenith angle (lower altitude), consistent with the behaviour of the viewing angle dependent distributions.

Note that the fraction of triggers distributions are normalised to the number of already triggered events, keeping a dependence on the absolute zenith angle (due to the smaller covered solid angle). The trigger fractions relative to the number of *simulated* events per energy bin and angle offset bin (viewing angle, relative azimuth and relative zenith) are given in sec. B of appendix B, highlighting mainly a plateau behaviour in the viewing angle dependence around the array pointing direction up to an offset of $\sim 60°$ for array zenith angles <30° (essentially the full simulated sky-dome) and a shift of this limit to $\sim 40°$ for lower altitude pointings of the telescope array. It is also shown, that the overall highest detection probability is for vertically inclined showers, decreasing with increasing shower

zenith angle.

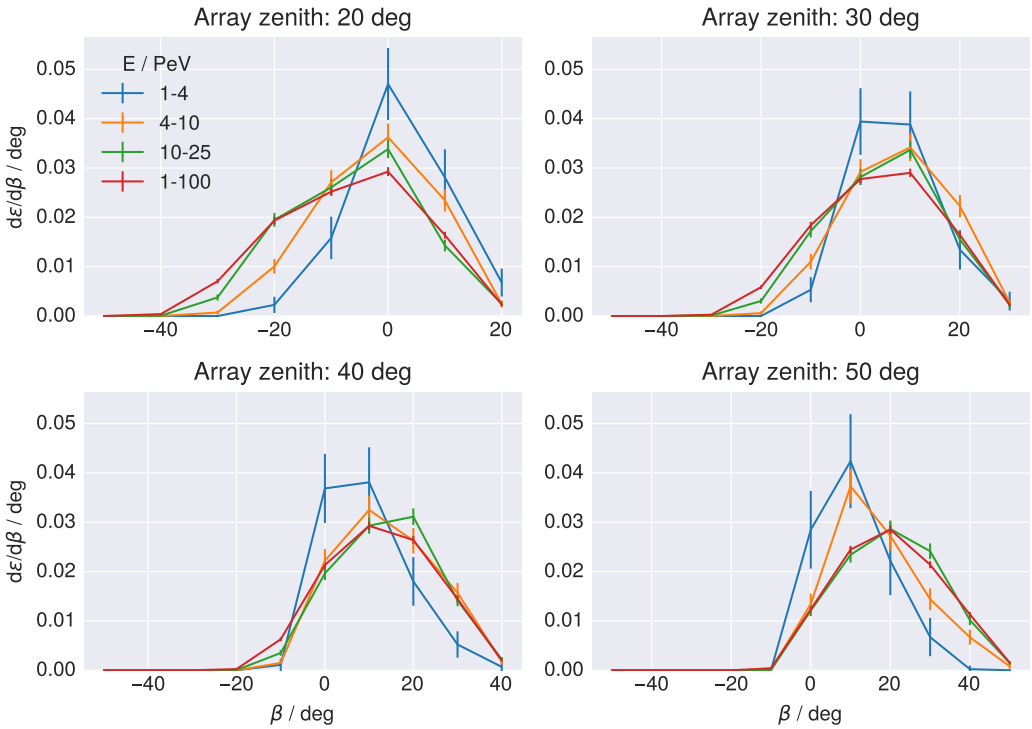

Figure 4.15: Differential fraction $d\epsilon/d\beta$ of triggered events as a function of relative zenith angle ϕ of the air showers and the telescope array for four pointings of the telescope array in parallel pointing mode. Positive values of β represent shower zenith angles from above the array pointing, while negative values represent showers coming lower parts of the sky. The dataset shown contains all four primary particle types and is binned into 4 levels of primary energy. The fractions shown are normalised to the total number of events within each energy bin. A stereoscopic trigger condition was required.

4.2.1 Effective area

The effective trigger area of the fluorescence-detecting CTA-South array has been calculated by using the following relation:

$$A_{\text{eff}} = n_{\text{E}_{\text{bin}}} \cdot A_{\text{sim}} \cdot \Omega_{\text{sim}} \tag{4.3}$$

with $n_{\text{E}_{\text{bin}}}$ the fraction of triggered events in the selected energy bin, the full simulated area $A_{\text{sim}} = 25\,\text{km}^2$ and the covered solid angle $\Omega_{\text{sim}} = \pi$ of the simulated sky-dome (up to 60° shower zenith angle). The effective area for both pointing strategies as a function of energy averaged over the four array pointing settings is shown in figure 4.16 (with a minimum of 2 telescopes participating). The effective area of the parallel pointed telescopes increases from $\sim$0.02-0.2 km^2 sr at the lowest energy bins to $\sim 10\,\text{km}^2$ sr for the highest energy bins. In contrast, the divergent pointing mode shows an increase of the effective area for primary energies > 5 - 10 PeV by a factor of ~ 2, with the trade-off for energies < 3 PeV, where the effective area decreases rapidly. As expected the overall effective area scales with

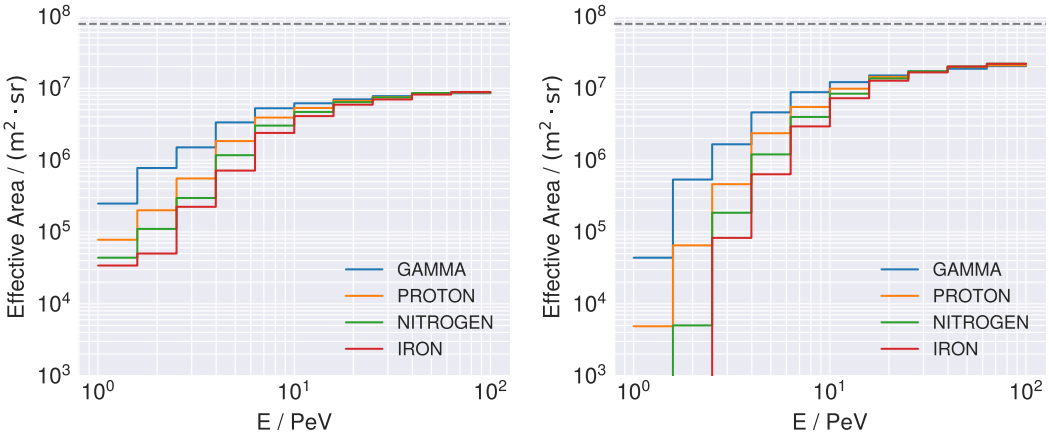

(A) Parallel pointing, minimum stereo trigger. **(B)** Divergent pointing, minimum stereo trigger.

Figure 4.16: Effective area for different primary particle types and energies. The dotted line shows the simulated area. All four simulated array zenith angle settings have been taken into account. A minimum of two telescopes was required to count an event as triggered. The dashed line shows the maximum achievable effective area within the simulation parameters, $\pi \cdot 25\text{km}^2$ sr for a maximum shower zenith angle of 60°.

the type of the primary at a fixed energy, due to the average higher altitude of the shower maximum with increasing atomic number Z of the primary particle (for hadron induced air showers) and the lower average number of charged particles compared to γ induced showers.

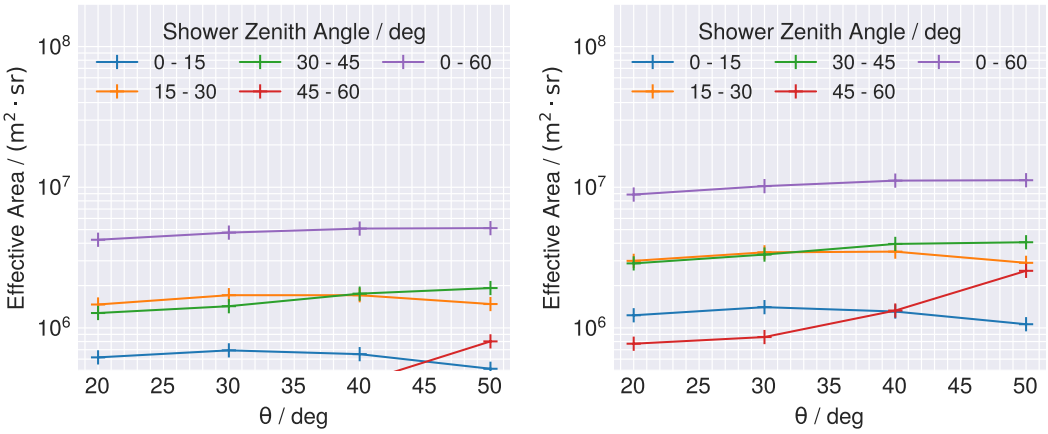

(A) Parallel pointing, minimum stereo trigger. **(B)** Divergent pointing, minimum stereo trigger.

Figure 4.17: Effective area as a function of the telescope zenith angle θ, for five bins of the incoming shower zenith angles. The four simulated primary particles (γ, proton, nitrogen and iron) and the full simulated energy range (1 - 100 PeV) have been taken into account. A minimum of two telescopes was required to count an event as triggered was required.

The dependence of the effective area on the array zenith angle θ has been studied by comparison of selected ranges of shower zenith angle (see fig. 4.17). The shown results average over the four primary particle types and all simulated energies. The full sky effective area in the parallel pointing setting amounts

to ~4-5 km^2 sr, while the divergent pointing mode increases the effective area by a factor of ~2 to ~9-10 km^2 sr. The main contribution to the effective area, dependent on the shower zenith angle, is in the range between 15°-45°, as the vertical shower may have a higher trigger probability, but the larger covered solid angle for larger zenith angles compensates the lower trigger probability at higher zenith angles. The higher zenith angle ranges >45° contribute less due to the low trigger probability (even with a larger sky area).

4.2.2 Cosmic Ray trigger rate

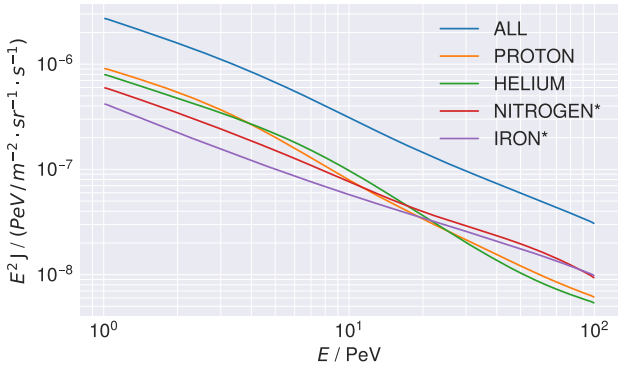

Figure 4.18: Cosmic-ray flux from an interpolated spline model based on composition-dependent cosmic ray data [11]. The shown fluxes are partitioned into proton, helium, and two groups the "nitrogen group" (nitrogen*) taking atomic numbers 3-10 into account and the "iron group" (iron*) 11-28.

The angular distribution of incoming cosmic-rays is assumed to be isotropic over the simulated sky-dome in this study. The differential trigger rates of the array are therefore calculated by using the cosmic ray fluxes independent of the incident angle relative to the telescope pointing direction. Figure 4.18 shows the interpolated splines of the cosmic ray fluxes, with proton and helium and two groups of primary hadronic particles named nitrogen* and iron*, taking atomic numbers between 3-10 and 11-28 into account. The binned differential trigger rate is estimated by using the following relation:

$$\frac{dN_{\mathrm{bin}}(E)}{dE\,dt} = \frac{A_{\mathrm{eff}} \cdot \int_{E_{\mathrm{min}}}^{E_{\mathrm{max}}} J\,dE}{E_{\mathrm{max}} - E_{\mathrm{min}}} \tag{4.4}$$

The results for combinations of the parallel and divergent pointing modes and a minimum requirement of mono- or stereo-triggers for a 30° array zenith angle is shown in figure 4.19.[8] The trigger rates due to helium have been estimated using the effective area for protons.

The peak differential trigger rate in the parallel and mono-trigger mode is in the lowest energy bin at ~1 PeV primary energy with ~0.3 Hz trigger rate, and an

[8] Additional results using an array zenith angle of 40° and 50° can be found in appendix B, figure B.9 and B.10

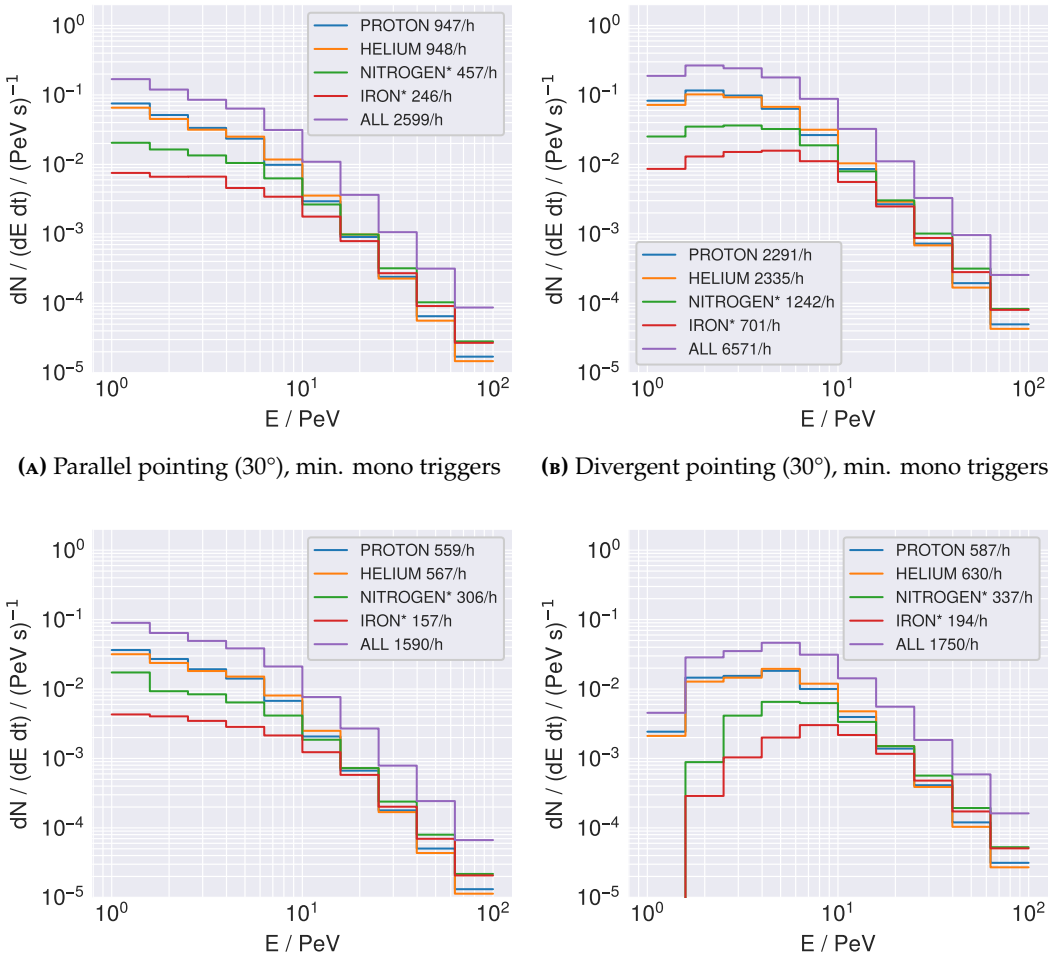

(A) Parallel pointing (30°), min. mono triggers

(B) Divergent pointing (30°), min. mono triggers

(C) Parallel pointing (30°), min. stereo triggers

(D) Divergent pointing (30°), min. stereo triggers

Figure 4.19: Differential trigger rates due to cosmic ray air showers for four sets of primary particle ranges. The array was pointed at 30° zenith angle in parallel and divergent pointing mode. Compared are also the differences between mono and stereo triggers.

integrated trigger rate of ∼0.7 Hz (∼2600/h). Comparison to other array zenith angles and the divergent pointing trigger rates, as well as the effective area result, suggest that the differential trigger rate does not extend with the same magnitude to lower energies, but that the peak must remain around 1 PeV. Divergent pointing increases the mini-trigger rate by a factor ∼2. Requiring a more realistic minimum of 2 telescopes detecting a shower sets the overall trigger rate to ∼1500-1700 events per hour, depending on the pointing strategy. Switching to divergent pointing for stereoscopic triggers shifts the peak of the differential trigger rates to ∼5 PeV for proton, helium and the nitrogen* group, while the iron* group peak is shifted even further to ∼5-10 PeV. Also to note is the sharp drop off at lower energies in the high atomic number groups. The comparison to the other array zenith angle results show, that the integral trigger rates stay similar for an telescope pointed at a zenith angle of 20°, with a slight decrease for the 40° simulations, and a reduction of the integral trigger rate by a factor of ∼2, when pointing to an array

zenith angle of 50°. Additionally, a drop in trigger rate for the lowest energy ranges < 3-4 PeV higher atomic numbers can be observed, due to the fact that the telescopes see only the lower part of the shower below the depth of maximum shower development.

4.3 Charge calibration & time gradient

Charge calibration

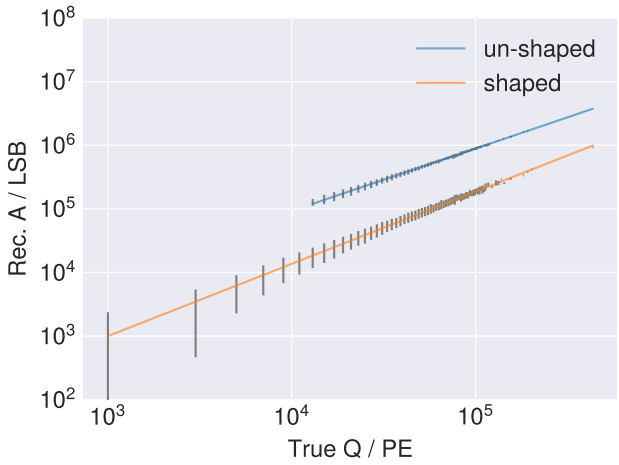

Figure 4.20: End-to end calibration of the reconstructed image amplitude in hardware units (LSB) is shown as a function of the true detected charge Q. The amplitudes are shown for the reconstruction using shaping (compression = 14, smoothing = 2) compared to the reconstruction using no shaping (compression = 0, smoothing = 0). The error bars of the profiles (grey) show the 2σ standard deviation per bin. The orange and blue lines show the results of the best fit of 4.5.

The reconstruction of the charge of an individual peak in the shaped (compressed and hexagonally smoothed) images provides a serious challenge, as the amplitudes of the peaks depend on the neighbouring pixels. This introduces a dependence on the shape of the shower image and the individual light distribution in the camera. To gain an estimation of the charge per peak an end-to-end calibration of the shower images has been performed, averaging over all the possible image shapes in the simulated datasets. The known Monte-Carlo truth of detected photoelectrons at the cathode of the PMTs has been used to calibration the total sum of the peak amplitudes in hardware units (LSB) for shaped and unshaped images. This also includes under-amplified photoelectrons. The following equation has been used to fit the logarithm of average of the sum of reconstructed amplitudes A per image as a function of the logarithm of the binned total charge in the same image (cf. fig. 4.20).

$$y = p_0 \cdot \log_{10} Q + p_1 \quad \text{with} \quad y = \log_{10} A \tag{4.5}$$

Inverting this equation gives a lookup equation for the total image amplitude yielding a reconstructed charge:

$$Q = 10^{(\log_{10} A - p_1)/p_0} = 10^{-\frac{p_1}{p_0}} \cdot A^{\frac{1}{p_0}} \tag{4.6}$$

$$= s \cdot A^r \quad \text{with} \quad s = 10^{-\frac{p_1}{p_0}}, r = \frac{1}{p_0} \tag{4.7}$$

The assumption going into the relation is, that a no The resulting fit parameters for the un-shaped case are r = 1.02 and s = 0.09 and the shaped case r = 0.88 and s = 2.3. The results for the un-shaped case confirm the set peak amplitude per photoelectron in the simulation (`fadc_amplitude` = 10 LSB/PE), with a small dependence on the total image amplitude and a scaling factor of ~ 0.1. The shaped images show an exponent r of <1, i.e. images with a larger true charge show a root-like increase in reconstructed amplitude A. Possible reasons are, that the hexagonal smoothing introduces losses a the edge of the camera and brighter images do not only increase the amplitude per pixel, but also increase the number of pixels above the threshold lateral to the shower axis.

The produced lookups have been cross-checked, by application to the reconstructed peak sums (in LSB) yielding a total image amplitude (in PE) (cf. fig. 4.21). As expected, the reconstructed charges show a good agreement to the true charges, and show a good overlap in the range, where the un-shaped images had pixels above the threshold. The reconstructed charges show a good overlap for lower image amplitudes with the true charges down to 10^3 PE per image. The peak of the distribution is at $\sim 4{\cdot}10^3$ PE per image, with the bulk of the events between $\sim 10^3$ and $\sim 2{\cdot}10^4$ PE.

It must be noted, that using the shaped images to estimate the image charge amplitude may not be necessary also for lower image amplitudes, as more sophisticated methods using the time windows of the shaped image peaks as primers to estimate the charge on a channel-wise basis (using the established reconstruction techniques in the analysis of Cherenkov images) exist.

Time structure of shower tracks

The analysis of the triggered shower images using the principal component analysis parameters allowed to calculate the time interval of the shower track within the field of view of the camera. The 95% separated distance of the major axis was chosen to determine the start and stop of the track and the time interval in between (Δt). The average time the shower spent within a pixel is given in figure 4.22A, showing the expected correlation between impact distance and the time gradient, which was calculated by normalising Δt to the length of the track within the camera. The dependence on the viewing angle confirms the geometric assumptions, that a shower aligned more closely with the viewing direction of the telescope shows a smaller time difference in arrival times, as the photons emitted

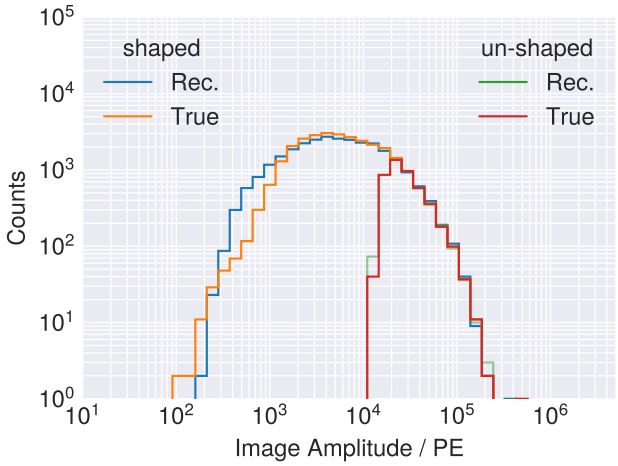

Figure 4.21: Histograms of the reconstructed and true charges for the shaped and un-shaped image reconstruction. The true charges per event are the same, yet the selection due to the trigger condition sets in at $\sim 10^4$ PE. for the un-shaped image amplitudes at $\sim 10^4$ PE.

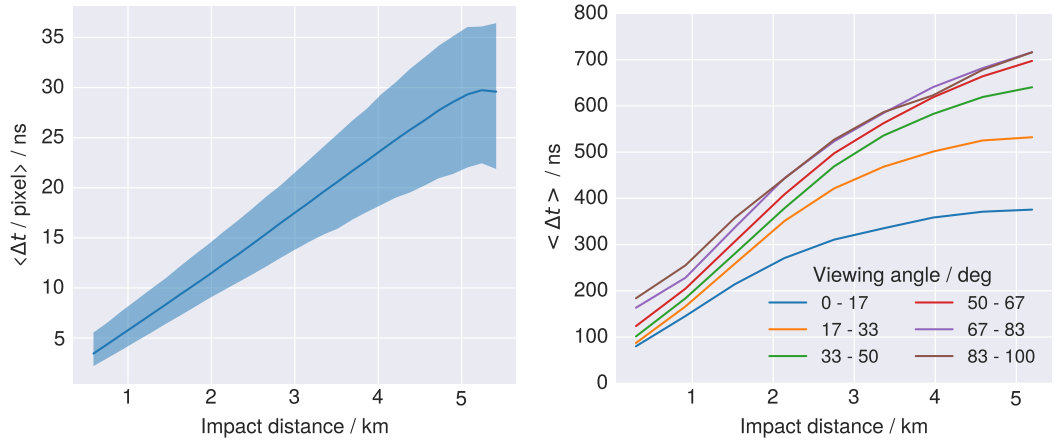

(A) Mean time gradient of shower tracks in the camera as function of impact distance. Shaded regions show the 80% containment.

(B) Mean observed time of shower tracks in the camera as function of impact distance

Figure 4.22: Time gradient and total time of shower tracks as function of impact distance. Included are all primary particle types and energies, as well as four pointing directions (20°-50°) of the divergent pointing dataset, triggered with a telescope multiplicity ≥ 2.

at the end of the visible part of the track are closer to the telescope, and thereby arrive closer in time to the photons arriving first.

4.4 Shower Axis Reconstruction

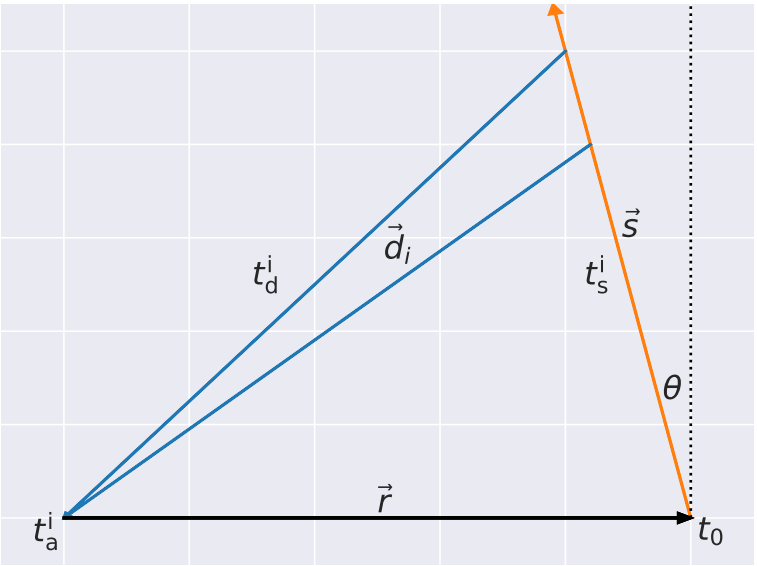

Figure 4.23: Side-on view of the geometry used assumed in the axis reconstruction. The vectors $\vec{d}_i$ originate from the centre of each pixel in the camera, cross the pinhole (focal point) of the assumed pinhole camera and end on the assumed shower plane (perpendicular to the page in this figure). The normal vector of this shower plane is parallel to the closest distance between the shower and the telescope. t_a^i is the photon arrival time in each pixel, t_d^i the time interval between the emission and the detection of a fluorescence photon, t_s^i the time interval between the emission point and the impact point. t_0 a is global time offset. $\vec{r}(x, y)$ is the vector to the impact point (from the array centre) and $\vec{s}(\theta, \phi)$ the shower direction.

A reconstruction of the shower axis has been implemented using the reconstructed peaks of the shaped events provided by the trigger algorithm. These peaks are defined as a pair of amplitude and time values, with the time being relative to the start of the traces. An additional array wide relative time-offset between the events of multiple telescopes can be used if multiple telescopes have been triggered. The underlying model of the axis reconstruction code assumes a line-like shape of the shower, disregarding the lateral shape variation within the camera. In this sense, the detected photoelectrons are assumed to be emitted from an isotropic source moving with the speed of light (in vacuum) through the atmosphere. To remedy the fact that the detected photons show a lateral distribution along the shower axis, the assumed point of origin of the respective photons has been taken to be from a plane parallel to the shower axis and its normal vector going through the focal point of the telescope. The telescope set-up itself was modelled as a pinhole camera with the camera sitting behind the pinhole with a distance of 16 m (distance between the mirror dish and the camera of an MST). The coordinates of the pixels in this model have been matched to the output of sim_telarray. The viewing direction of each pixel is then given by the vector between the pixel location in a global Cartesian coordinate system and the pinhole,

by the azimuth and zenith orientation of the telescope itself. The detected photo-electrons are assumed to originate from an emission point along this pixel vector, which is assumed to be from the intersection with the aforementioned shower plane.

Figure 4.23 shows the geometric set-up from a side-on view. The time of arrival t_a^i of each reconstructed peak (with the index i over all pixels participating in the event) depends on the distance of the shower to the array centre $\vec{r}$, the orientation of the shower $\vec{s}$ and the global time-offset t_0. Under the assumption of a known shower geometry, the distance $\vec{d}_i$ of each pixel to the assumed emission point can then be calculated with the following relations:

$$t_a^i = t_0 - t_s^i + t_d^i \tag{4.8}$$

$$t_d^i = t_a^i + t_s^i - t_0 \tag{4.9}$$

$$\vec{d}_i = t_d^i \cdot c_{\text{air}} \cdot \vec{p}_i \tag{4.10}$$

The vector $\vec{p}_i$ is the normalised orientation vector of each pixel, with its location in the camera detection plane. The pixels of the camera are defined in a global coordinate system, with the origin set at the array centre and the time of arrival of each peak in reference to an array wide clock. The optimisation problem needed to solve has 5 free parameters, the shower impact point $\vec{r}(x, y)$ depends on the x and y-coordinate in the global coordinate system, the shower direction $\vec{s}(\theta, \phi)$ depends on the shower azimuth and zenith angles and the global time offset t_0.

Algorithm The algorithm performing the reconstruction has been implemented using the non-linear optimisation library NLOPT [34] with the BOBYQA algorithm [51]. The minimisation objective has been constructed by requiring an overall line-likeness of spatial distribution of the back-projected emission points of each detected peak. The steps of the algorithm are as follows:

- Use the start parameters (or the results from the previous loop) to construct a shower geometry $\vec{r}$ and $\vec{s}$.
- Calculate the distances d_i as a function of the input parameters, and back-project the detected peaks, yielding the emission points of the detected photons.
- Perform a linear least-squares fit in the X-Z and the Y-Z plane (North-Zenith and West-Zenith) creating a reconstructed shower axis, with the peak amplitudes as weights.
- Determine the offset between the input shower axis and reconstructed shower axis using the angle Δs between both $\vec{s}$ vectors and the distances Δr between both $\vec{r}$ vectors.

- Construct the objective value $R = \Delta s^2 + \Delta r^2 + \chi^2_{\text{int}}$, with χ^2_{int} the sum of the squared residuals of the least-squares line fit. R is then returned from the objective function to the optimiser.
- The optimiser stops when a relative change in the input parameters of 10^{-4} has been achieved or 2000 iterations have been performed.

Start parameters The application of the algorithm to the data has shown that the fit does perform poorly (not finding a global minimum) when the start parameters (e.g. at a fixed value for each reconstructed event) placed the starting shower axis outside the field of view of the cameras. In some of the cases (more pronounced in mono trigger mode), the fit converges to a horizontal shower axis close the telescopes, as the different travel times in eq. 4.9 can compensate each other, while the χ^2 of the internal line fit provides not enough discrimination power to avoid this minimum. The overall starting value of t_0 and $\vec{r}$ has been found to be the most dominant influence, as it sets the overall scale to the problem in the first round of the iterative solver. Due to this problem, the approach in this work has been, to start the solver with the Monte-Carlo truth, allowing the algorithm to pre-fit the starting value of t_0 (as this value does not only depend on the shower geometry but also on the simulated array wide clock) and then starting the final solver with an offset of 100 m in r_x, an azimuth angle offset of $+30°$ and a zenith angle offset of $+10°$.

An additional pre-reconstruction algorithm using the PCA components of the trigger algorithm, using the length and width orientation of the track, to determine a plane defined by the line in the camera coordinates and the telescope focal point, and using the time gradient of the track had been tested in the mono-reconstruction, but not incorporated into the reconstruction presented here.

Angular resolution and Impact distance resolution

The shower axis reconstruction algorithm has been applied to the same datasets that has been used to study the effective area of the CTA-South MST array detecting the fluorescence emission from air showers. As before, the differences between the pointing strategies and the mono and stereoscopic trigger modes are highlighted by presenting the results of the angular resolution R and impact resolution I as functions of primary energy E and total image amplitude A (in reconstructed photoelectrons). The resolutions shown are calculated by taking the 68% containment value of the binned statistics with a minimum of 10 events per bin. The angular resolution as a function of total image amplitude is shown in figure 4.24, additionally separated into four ranges of the true impact distance and the full range of possible impact distances. All four simulated primary particles (γ, proton, nitrogen and iron) have been taken into account. Panels 4.24A and 4.24B show the angular resolution for all triggered events, allowing mono mode triggers

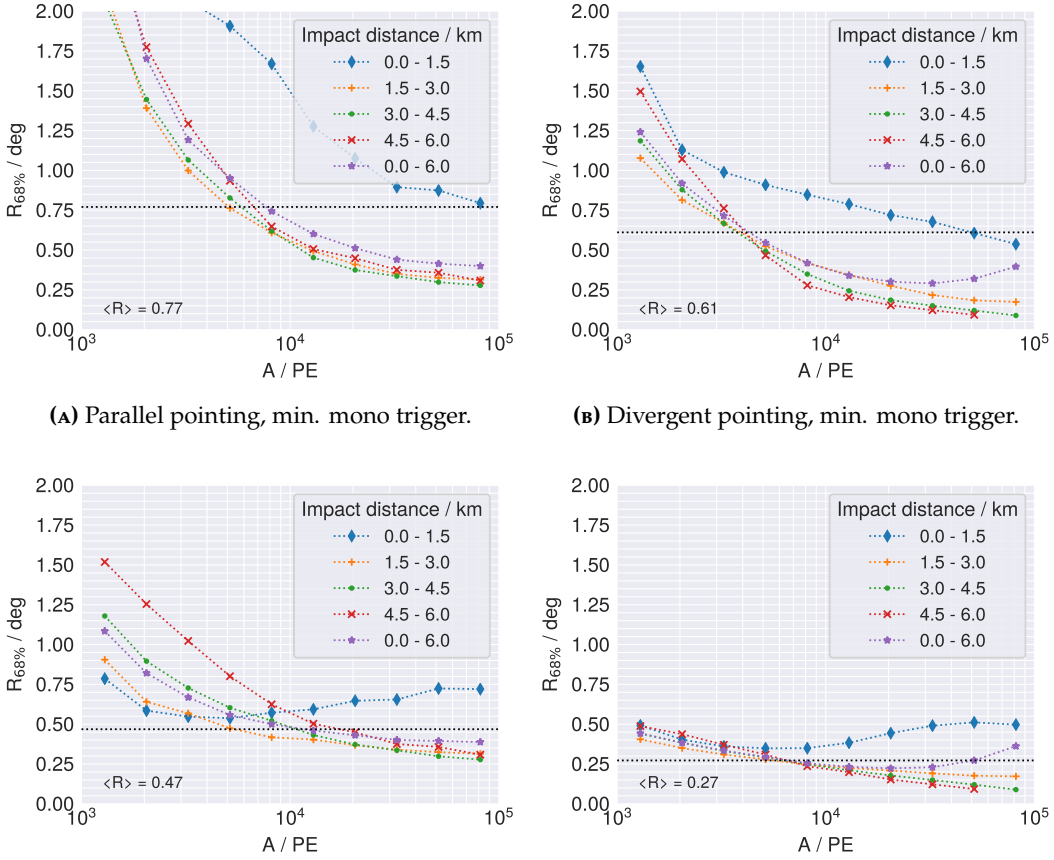

(A) Parallel pointing, min. mono trigger.

(B) Divergent pointing, min. mono trigger.

(C) Parallel pointing, min. stereo trigger.

(D) Divergent pointing, min. stereo trigger.

Figure 4.24: Angular resolution R of the 25 MST sub-array as a function of image amplitude in reconstructed photoelectrons. The shower axis has been reconstructed with a line-like model. The resolution has been determined by the 68% containment value of the angular offset between the Monte-Carlo truth and the reconstruction direction for each event.

to contribute, with an average angular resolution of 0.77° in the parallel pointing mode and an average angular resolution of 0.61° in the divergent pointing mode. The averages presented in all figures in this section are calculated by taking the average of all reconstructed events,only differentiating by the pointing strategy and the minimum telescope multiplicity.

The average resolution for a pure mono trigger is not presented here, but is reported as significantly worse with 1.3° in divergent pointing mode and 4.7° in parallel pointing mode, due to the fact, that the stereoscopic view of the shower provides a better constraint on the shower distances than the difference in arrival time of the pixels within one camera.

Requiring a minimum of two telescopes in the trigger decision (stereo-mode) improves the average angular resolution to 0.47° in parallel pointing and 0.27° in divergent pointing. The results also show a dependence on the impact distance of the shower, where showers impacting too close to the array (< 1.5km) show a worsening in the resolution for too high image amplitudes (cf. panel 4.24c, 4.24d). This is mainly due to the large image sizes for too close showers, where

the requirement on the line-likeness breaks down. The parallel pointing mode shows a more pronounced worsening of the angular resolution in dependence of the impact distance for $<10^4$ PE image amplitude, compared to the divergent pointing mode, as the impact distance shown here is calculated to the array centre and includes shower far to the side (East or West), where the error on the reconstruction is larger due to the longer lever arm and the smaller portion of the shower seen by the array. Using the divergent pointing mode reduces this source of uncertainty due to the wider separation of observation points along the shower axis.

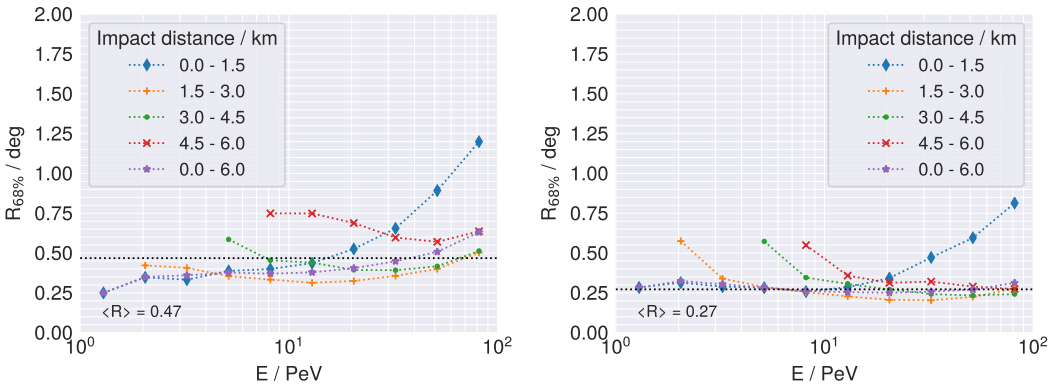

(A) Parallel pointing, min. stereo trigger.

(B) Divergent pointing, min. stereo trigger.

Figure 4.25: Angular resolution of the 25 MST sub-array as a function of primary energy. The shower axis has been reconstructed with a line-like model. The resolution has been determined by the 68% containment value of the angular offset between the Monte-Carlo truth and the reconstruction direction for each event.

The angular resolution R as a function of primary energy (separated into four ranges of impact distance) is shown in figure 4.25. The clear dependence of the detectable distance on the primary energy can be seen due to the cut-off in reconstructed events. As already seen before (4.24), the correlation between image amplitude and primary energy leads to the decrease in resolution for close impact points and high primary energies.

The impact resolution as a function of image amplitude is shown in figure 4.26, with an average resolution of ~ 20 m requiring multi-telescope triggers, and 32-37 m including mono triggered events. The average impact point resolution for pure mono-triggers is 165 m and 92 m for parallel and divergent pointing respectively.

As with the angular resolution, the stereo-mode performs significantly better (as expected). The divergent pointing mode also improves the resolution, while the average improves only slightly, the events impacting far away (>3 km) are significantly better reconstructed.

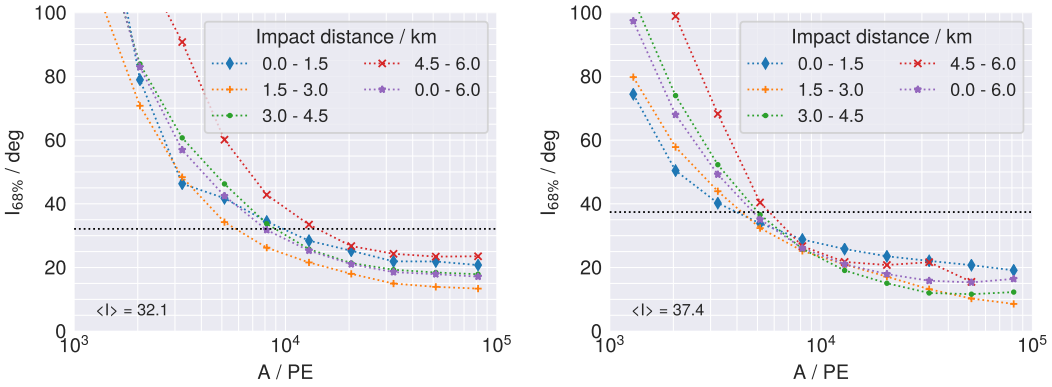

(A) Parallel pointing, min. mono trigger.

(B) Divergent pointing, min. mono trigger.

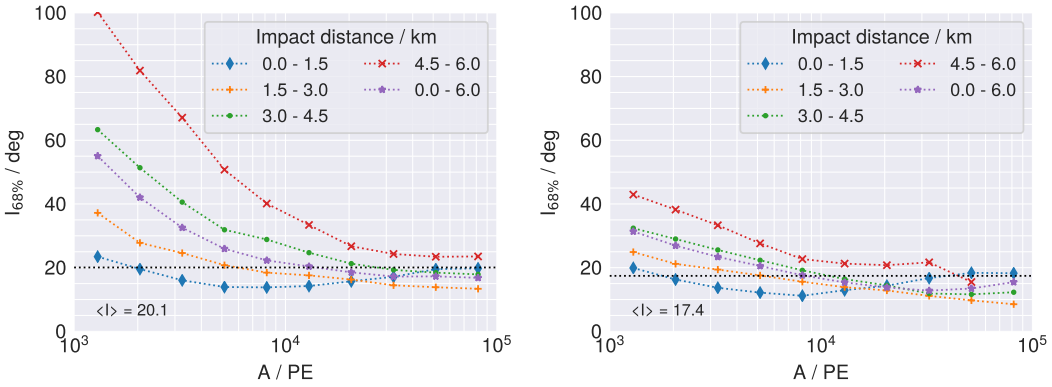

(C) Parallel pointing, min. stereo trigger.

(D) Divergent pointing, min. stereo trigger.

Figure 4.26: Impact point resolution I of the 25 MST sub-array as a function of the reconstructed image amplitude. The shower axis has been reconstructed with a line-like model. The resolution has been determined by the 68% containment value of the impact point offset between the Monte-Carlo truth and the reconstruction location for each event.

4.5 Point source sensitivity

The sensitivity of the CTA-South MST sub-array to a γ-ray point source using the developed fluorescence emission detection technique is studied in this section. To this end, a trigger probability sky map as functions of shower azimuth and zenith angle has been determined, by computing a spline interpolation[9] of the trigger probabilities determined in section 4.1. These maps have been produced for all variations of the telescope array pointing, the pointing strategy, the primary particle type and the primary energy, as well as a range of rotated telescope arrays (in 8 steps of $45°$ in azimuth angle). The trigger requirement regarding telescope multiplicity has been set to a minimum of 2 participating, due to the better reconstruction power.

Using the position of the CTA-South array on Earth, the one year visibility (in steps of 5 min) of a range of source positions has been calculated, with the range in declination between -80° and 40° in steps of 10° and the range in right ascension around the galactic centre between 246.4° and 286.4° in steps of 10°. The requirement on the visibility was threefold, the sun and the moon needed to be below the horizon ($-5°$ in altitude) and the source needed to be above $30°$ altitude (the range in which the simulations have been performed, and the trigger probability maps can be applied).

The one year exposure A_{exp}, depending on the combinatorics of the telescope pointings, source positions, primary particle types and 10 bins of the primary energy, have been determined by calculating the sum of the respective effective area for each time bin (5 min), where the source was visible.

The number of cosmic-ray background events has been computed by using the differential cosmic-ray flux J (cf. 4.18) to determine the integrated flux $F(E_{\mathrm{bin}})$ for each energy bin, scaled with the Ω_{bg} background region around the source positions. Ω_{bg} is dependent on the point spread function (PSF) of the telescope array and the extent of the source (which has been assumed to be point-like). The PSF value used was 0.3° for the divergent pointing mode and 0.5° in the parallel pointing mode, determined by the angular resolution presented in the previous section.

The total number of cosmic-ray background events in one year in the region Ω_{bg} for all previously mentioned combinations of the observation settings and source positions has been calculated with $N_{\mathrm{CR}}(E_{\mathrm{bin}}) = A_{\mathrm{exp}} \cdot F(E_{\mathrm{bin}})$. The excess in number of γ events required for a 5σ detection has been calculated depending on the total number of background events N_{CR} and a scaling constant s, which allows the scaling of the average one year observation time[10].

[9] SmoothBivariateSpline function of the SciPy package [58]

[10] n_{excess} determined by using the `excess_matching_significance` function of the CashCountsStatistic model of the analysis package [12][40].

The integrated minimum flux F_γ for a detection for each energy bin has been calculated as follows,

$$F_\gamma = \frac{n_{\text{excess}}}{A_{\text{exposure},\gamma} \cdot s} \quad \text{with} \quad n_{\text{excess}} = n_{\text{excess}}(N_{\text{CR}}, s, \sigma = 5) \tag{4.11}$$

leading to the differential point source flux sensitivity dN/dE:

$$\frac{dN}{dE} = \frac{(-\alpha + 1)\ E_{\text{mean}}^{-\alpha}}{E_{\text{max}}^{-\alpha+1} - E_{\text{min}}^{-\alpha+1}} \cdot F_\gamma \quad \text{with} \quad \alpha = 2. \tag{4.12}$$

The assumed spectral index in determining the required differential flux is $\alpha = 2$ (although the influence with a fine enough binning of primary energies is small).

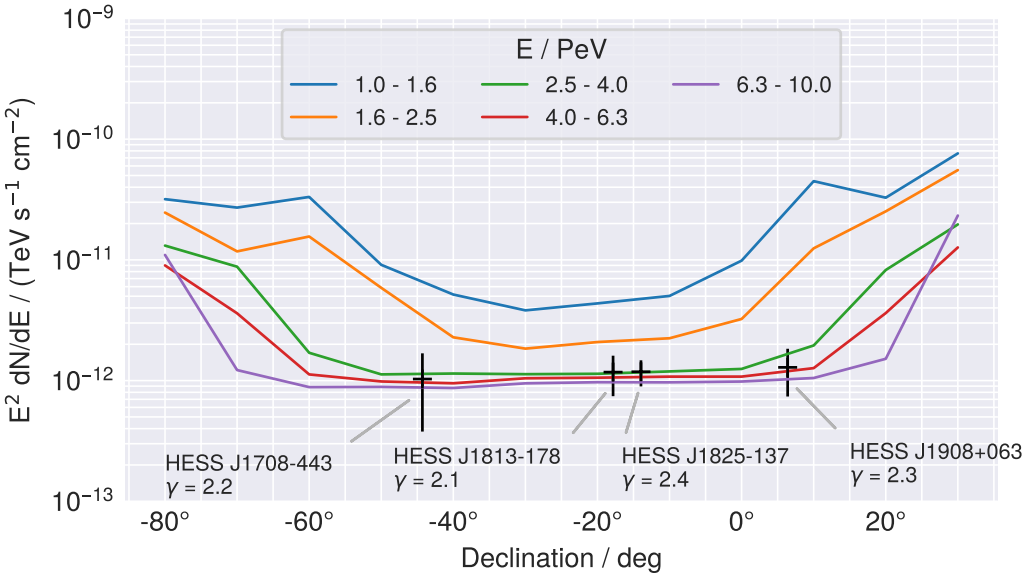

Figure 4.27: The differential γ-ray point source flux sensitivity $E^2 dN/dE$ as a function of source declination, for 5 bins in primary energy. Four exemplary sources are shown with their extrapolated fluxes at an energy of 3 PeV. The observation time of the array has been set to 15 years and a divergent array pointing with a PSF of 0.3° has been assumed. No $gamma$/hadron separation has been taken into account.

Results The results presented here show the average differential flux sensitivity for point-like γ-ray sources as a function of source declination and primary energy (averaged over the 8 x 4 x 5 variations in azimuth and zenith telescope array pointings and source position variations in right ascension). The pointing strategies (parallel and divergent) have been studied separately with their respective (so far) achievable angular resolution (0.3° and 0.5°) and an average total observation time of 15 years, assuming perfect observation conditions (only limited by the visibility of the sources).

The best case scenario, without any γ/hadron separation, using the divergent pointing mode, is presented in figure 4.27, with an achievable differential flux

sensitivity 10^{-12} TeV / (cm^2 s) for primary energies above ~ 3 PeV and source declinations between $-60°$ and $10°$. The comparison to the parallel pointing mode (cf. 4.28) shows an improvement in sensitivity by a factor of ~ 2 for primary energies > 3 PeV. For the low energy bins, the sensitivity improves less due to higher stereoscopic trigger probability and reconstruction power of the parallel pointed telescope array in those energy ranges. The results using only one year of observation time are presented in appendix B, showing an achievable differential flux sensitivity of ~ $5{\cdot}10^{-12}$ TeV / (cm^2 s) and ~ 10^{-11} TeV / (cm^2 s) for the divergent and parallel pointing mode respectively, meaning a factor of ~ 5 in sensitivity is gained by increasing the observation time to ~ 15 years (well within the planned runtime of the CTA observatory).

As a reference, four exemplary sources have been chosen from the H.E.S.S. galactic plane survey catalogue [23] and their spectral models (given in the catalogue) extrapolated to the studied range of primary energy (HESS J1908+06 [2], HESS J1708-443 [22], HESS J1813-178 and HESS J1825-137 [2, 44]). HESS J1908+06 and HESS J1825-132 have also been associated to detected sources by the HAWC observatory with emission above 100 TeV, while HESS J1908+06 shows no apparent cut-off in the spectrum and has been hinted as possible source of neutrino emission [32].

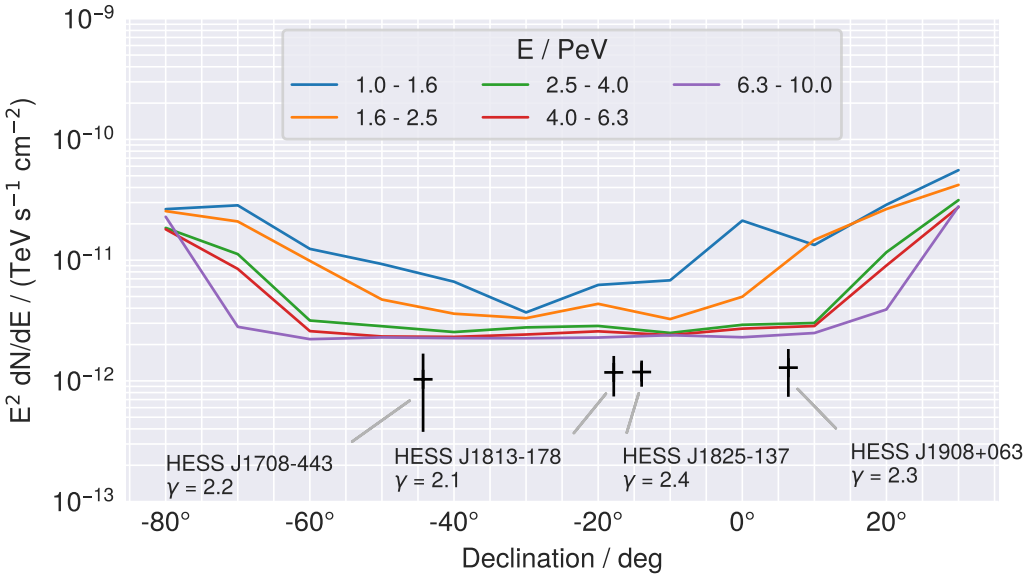

Figure 4.28: The differential γ-ray flux sensitivity E^2dN/dE as a function of source declination, for 5 bins in primary energy. Four exemplary sources are shown with their extrapolated fluxes at an energy of 3 PeV. The observation time of the array has been set to 15 years and a parallel array pointing with a PSF of 0.5° has been assumed. No *gamma*/hadron separation has been taken into account.

Energy dependence The differential flux sensitivity as a function of the primary energy for a range of source target declinations between $-60°$ and $10°$ is shown in figure 4.29, with divergent pointing mode, 15 years of observation and

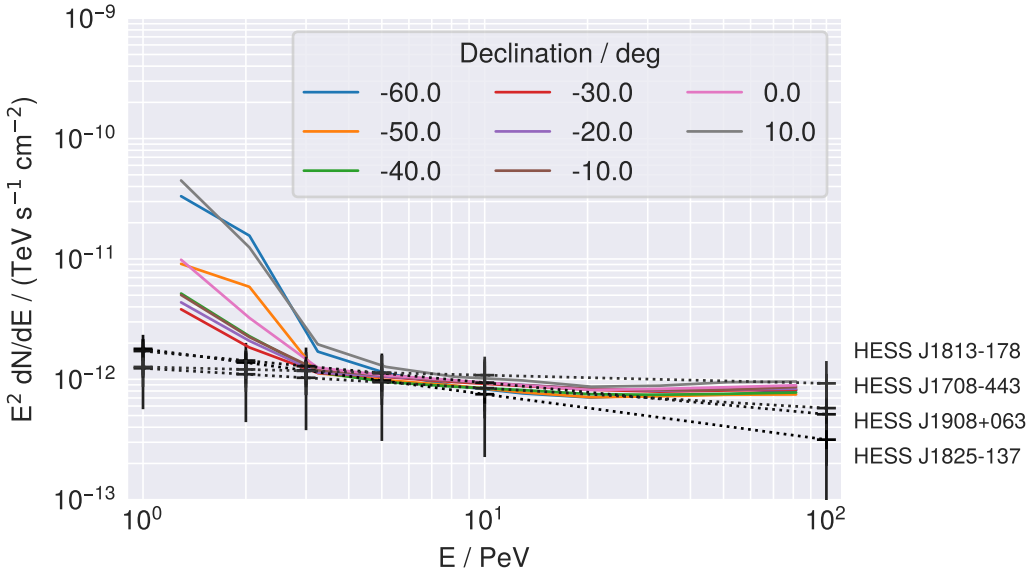

Figure 4.29: The differential γ-ray flux sensitivity $E^2 dN/dE$ as a function of source declination, for 5 bins in primary energy. Four exemplary sources are shown with their extrapolated fluxes. The observation time of the array has been set to 15 years and a divergent array pointing with a PSF of 0.3° has been assumed. No *gamma*/hadron separation has been taken into account.

no γ/hadron separation. The extrapolated flux spectrum of the four exemplary sources show the crossover regions at ≤ 3 PeV up to ~ 10 PeV. Depending on the source spectrum and its absolute flux, a reduction in the assumed observation time may be possible by combining the shown energy bands.

γ/hadron separation The possibility of a working γ/hadron separation has been explored, by decreasing the number of background events in the source region by a factor of 10, assuming that only 10% of the detected showers cannot be identified as of hadronic origin. This has been implemented by scaling the number of background events N_{CR} in the background region (in eq. 4.11) by a factor of 0.1. The overall differential flux sensitivity increases to $\mathrm{E}^2\,\mathrm{dN/dE}$ of $4 \cdot 10^{-13}$ TeV / (cm^2 s). Figure 4.30 shows the results with this assumed γ/hadron separation power, but only a 5 year observation time, highlighting the saved time needed for a possible detection. Possible observables allowing the separation of γ and hadron showers include the mean difference of the depth of the shower maximum (X_{max}) at a fixed primary energy, i.e. γ shower penetrate the atmosphere deeper than hadronic showers, and the lateral width of the showers, as they are on average wider than γ showers, due to their more irregular structure.

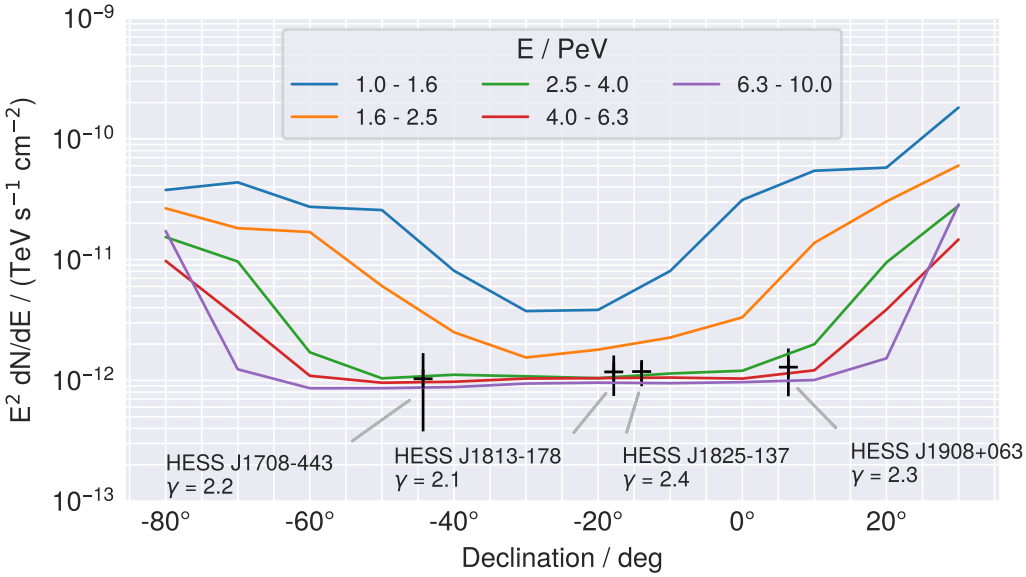

Figure 4.30: The differential γ-ray flux sensitivity $E^2 dN/dE$ as a function of source declination, for 5 bins in primary energy. Four exemplary sources are shown with their extrapolated fluxes at an energy of 3 PeV. The observation time of the array has been set to 5 years and a divergent array pointing with a PSF of 0.3° has been assumed. The possibility of a working γ/hadron separation has been explored by scaling the number of background events by a factor of 0.1.

4.6 Summary & Outlook

In this chapter, the detection capability of fluorescence emission from air showers by use of FlashCam cameras mounted on the MST telescopes of the CTA-South array has been studied. The digital and reconfigurable nature of the FlashCam camera trigger and readout system allows the design of a separate slow time signature trigger path, running in parallel to the fast Cherenkov trigger system. This trigger system can be used to successfully detect air showers in the atmospheric volume above and in front the telescope array, with primary energies between $\sim 10^{15}$ and $\sim 10^{17}$ eV. The field of view of this detection method is estimated at $\sim 45°$, up to $\sim 60°$, depending on the pointing direction, pointing strategy and the primary energy of the particles inducing the air showers. The overall effective area of the observatory has been estimated between $\sim 5\,\mathrm{km}^2$ sr and $\sim 10\,\mathrm{km}^2$ sr mainly dependent on the pointing strategy, with the additional hint, of an actual larger effective area using the divergent pointing mode, due to the closely calculated simulation boundaries. The total trigger rates of hadronic primaries (up to iron) within the simulated energy range have been estimate at ~ 0.5 Hz in stereoscopic trigger mode, with a night-sky background induced mono trigger rate of ~ 1 Hz. A shower axis reconstruction has been implemented using a line-like model, demonstrating that an average angular resolution of the shower direction is achievable between $\sim 0.3°$ (divergent) and $\sim 0.5°$ (parallel), mainly dependent on the pointing strategy. It has also been demonstrated, that a differential flux sensitivity on point like γ ray emitting sources between $2 \cdot 10^{-12} \frac{\mathrm{TeV}}{\mathrm{cm}^2\mathrm{s}}$ and $10^{-12} \frac{\mathrm{TeV}}{cm^2 s}$ for

energies $\geq 2\,\mathrm{PeV}$ is within reach, for observation times of $\sim 15\,\mathrm{years}$. It should be mentioned, that a detection may be achievable with less observation time, when combining multiple energy bands. A working γ/hadron separation may equally reduce the needed observation time for the detection of a point-like γ ray emitter.

Outlook

- The trigger design developed here makes use of the spatial distribution of the detected peaks, while the time structure of the shower development (the track in the camera) has only been taken into account on the individual channel level. Additional track detection methods can be though of (e.g. using a Kalman filter [36] or other structure detection mechanisms). An good solution for the second trigger stage would operate fully on the FlashCam master card, making additional processing on the readout server superfluous.

- The image reconstruction could be improved by using the image shaping as a input to more sophisticated algorithms. Additional optimisation in the compression window (which has been optimised for the trigger) would improve the signal-to-noise ratio on a pixel level, for a better charge reconstruction.

- The shower reconstruction presented here, does not take the longitudinal and lateral shower development into account, which should improve the resolution further. A 3-D model of the shower development can be envisaged, where showers with observations around the shower maximum (X_{max}) or enough data points along the shower axis allow the application of the Gaisser-Hillas function [18] or the Greisen profile [61, 46] in combination with a measurement of the width [42, 21]. This would also enable the reconstruction of the shower energy.

- The divergent pointing strategy used in this work, has been set up "ad-hoc". Further studies regarding the pointing strategy of CTA are ongoing, e.g. a sky survey mode could be using a divergent pointing, increasing the sky coverage (field of view) of the array [14].

- The emission studied in this chapter by simulations has been purely the fluorescence emission of the air showers. An implementation of the fluorescence trigger must take the additional scattered Cherenkov light into account, even for impact distances $\geq 1.5\,\mathrm{km}$.

- The SST (Small-Sized Telescopes) sub-array of the CTA-South observatory extends much further from the array centre (up to 1.2 km) than the MST sub-array. For showers with an intermediate impact distance, still visible by the SSTs in Cherenkov, a supporting role of the MSTs could be thought of, with a combined analysis of mono triggered events in the MST and SST sub-array. However this depends on the relative pointing between the telescope sub-arrays.

Chapter 5

Conclusion

The work undertaken in this thesis was twofold: The verification of the trigger performance of the FlashCam Cherenkov camera and the study of the fluorescence light detection capabilities of the FlashCam camera equipped medium-sized telescope sub-array of the Cherenkov Telescope Array.

- The unique capabilities of the FlashCam camera trigger system have been demonstrated by implementing the trigger algorithm in software, allowing the exact reproduction of the trigger response.
- The full parameter space of the trigger configuration was explored, determining the optimal ranges to chose for various observation conditions, mainly dependent in the night-sky background light level.
- An improvement of the FlashCam detector description in the Monte-Carlo simulations was achieved during the course of this work. A good Monte-Carlo description of the detector is relevant, as the reconstruction and analysis of shower images relies on Monte-Carlo simulations.
- The better understanding of the photomultiplier characteristics and calibration lead to the conclusion that the trigger response of the FlashCam camera is understood on a $\sim 1\,\%$ level and operates close to the Poissonian limit.

The digital and reconfigurable nature of the FlashCam trigger and readout system enables the adaption of a separate trigger path, optimised for the slow time structure of fluorescence light signals from air showers. An extensive Monte-Carlo study was carried out, investigating the fluorescence detection capabilities of the FlashCam-MST.

- It has been shown, that fluorescence light of air showers with up to μs differences in arrival time of the fluorescence photons can be detected by the designed trigger algorithm.
- The effective area for such a detector was estimated to be between $\sim 5\,\mathrm{km}^2$ sr and $\sim 10\,\mathrm{km}^2$ sr, depending on the pointing strategy of the array, for air showers with primary energies >1 PeV.

- The total detection rates due to hadronic air showers up to iron were estimated at $\sim 0.5\,\mathrm{Hz}$ in the stereoscopic trigger operation, with an accidental trigger rate of $\sim 1\,\mathrm{Hz}$ due to night-sky background fluctuations.
- A line-like shower axis reconstruction has been developed and implemented, demonstrating that an angular resolution between $\sim 0.3°$ and $\sim 0.5°$ is achievable with stereoscopic observation of the fluorescence emission of air showers.
- It has also been demonstrated, that a differential flux sensitivity for point-like γ-ray emitting sources between $2 \cdot 10^{-12}\,\frac{\mathrm{TeV}}{\mathrm{cm^2 s}}$ and $10^{-12}\,\frac{\mathrm{TeV}}{\mathrm{cm^2 s}}$ for energies $\geq 2\,\mathrm{PeV}$ is within reach, for observation times of ~ 15 years, with the prospect of a reduced observation time hinging on successful γ/hadron separation. The combination of all detectable energy bands will reduce the needed observation time further.

In conclusion, adding the capability of air-shower detection via fluorescence light to CTA may contribute to the search of acceleration sites of galactic cosmic-rays of the highest energies.

Future prospects A FlashCam camera was installed on the large CT5 telescope of the H.E.S.S. observatory in October 2019, running in routine operation since. Although the field of view of the CTA5 telescope is smaller ($\sim 3.2°$) than the field of view of an MST, the deployed FlashCam would provide a working experiment, allowing a test of a fluorescence trigger implementation in the field. The study of fluorescence detection capabilities of a Cherenkov telescope array has just started with this work - many promising paths to improve the shown baseline trigger & analysis algorithm have been identified.

Appendix A

Trigger verification - supplements

Trigger logic reference implementation in C

We provide an unoptimised, shortened implementation of the trigger logic in C to serve as a reference below. The function `check_trigger()` calculates the trigger of the whole camera at one time step (sample). The array of traces are the readout traces sampled by the camera. The lookup tables have to be filled separately and are specified by the layout of each pixel in the camera. These pixel and patch lists can be found in `sim_telarray/cfg/CTA/camera_CTA-MST-FlashCam_patch3_digitalsum9.dat`.

```
#define FC_PATCHES 588
#define FC_PATCH_SUMS 3

int has_triggered(int trigger_treshold,
                  unsigned short **traces,
                  int sample,
                  int ***lookups,  // patch lookups K & L (Eqs. 2.9)
                  int *athr,  // lower threshold A (Eq. 2.6)
                  int *tgm)  // scale factor S (Eq. 2.7)
{
  for (int k = 0; k < FC_PATCHES; k++) {
    int **patch_lookups = lookups[k];

    unsigned short patch_sum = 0;
    for (int l = 0; l < FC_PATCH_SUMS; l++) {
      int *pixel_lookups = patch_lookups[l];

      unsigned short pixel_sum = 0;
      for (int i = 0; i < 3; i++) {
        int j = pixel_lookups[i];
        pixel_sum += channel_trigger(traces[j], sample, athr[j], tgm[j]);
      }
```

```
      patch_sum += pixel_sum / 2;
    }

    if (patch_sum > trigger_threshold)
      return 1;
  }

  return 0;
}

unsigned short channel_trigger(unsigned short *trace,
                               int sample, // must be >1 and < n-2
                               int athr,
                               int tgm)
{
  // apply default filter (Eq. 2.1); can be exchanged for different filter
  int diff = trace[sample+1] + trace[sample]
           - trace[sample-1] - trace[sample-2];

  if (diff < 0)
    return 0;  // clip falling edges

  if ((athr > 1) && (diff / 2 < athr))
    return 0;  // clip signals below lower threshold

  // return scaled & clipped signal
  unsigned short scaled = (diff * tgm) / 256;
  return (scaled > 85) ? 85 : scaled;
}
```

FlashCam PDP Layout

The positions of the PDP modules in the Flashca

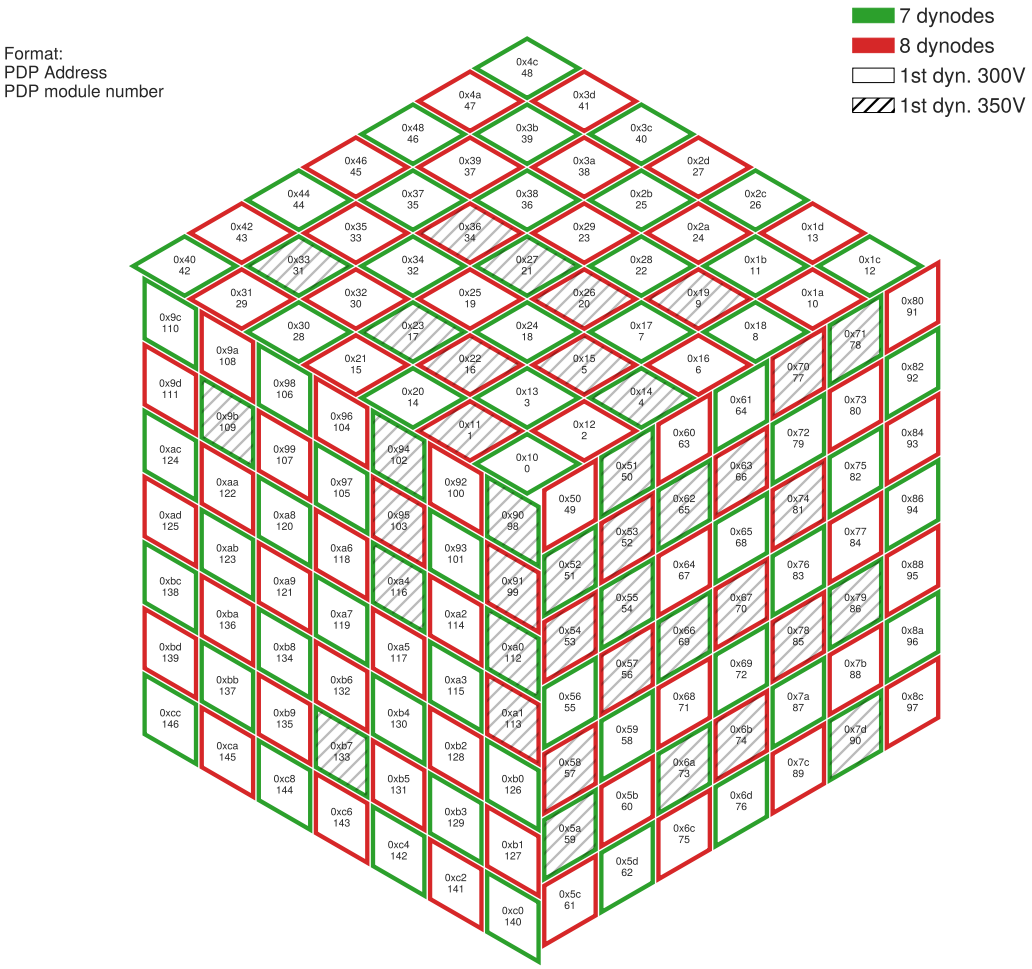
Format:
PDP Address
PDP module number
7 dynodes
8 dynodes
1st dyn. 300V
1st dyn. 350V
0x4c 48
0x4a 47
0x3d 41
0x48 46
0x3b 39
0x3c 40
0x46 45
0x39 37
0x3a 38
0x2d 27
0x44 44
0x37 35
0x38 36
0x2b 25
0x2c 26
0x42 43
0x35 33
0x36 34
0x29 23
0x2a 24
0x1d 13
0x40 42
0x33 31
0x34 32
0x27 21
0x28 22
0x1b 11
0x1c 12
0x31 29
0x32 30
0x25 19
0x26 20
0x19 9
0x1a 10
0x80 91
0x9c 110
0x30 28
0x23 17
0x24 18
0x17 7
0x18 8
0x71 78
0x9a 108
0x21 15
0x22 16
0x15 5
0x16 6
0x70 77
0x82 92
0x9d 111
0x98 106
0x20 14
0x13 3
0x14 4
0x61 64
0x73 80
0x9b 109
0x96 104
0x11 1
0x12 2
0x60 63
0x72 79
0x84 93
0xac 124
0x99 107
0x94 102
0x10 0
0x51 50
0x63 66
0x75 82
0xaa 122
0x97 105
0x92 100
0x50 49
0x62 65
0x74 81
0x86 94
0xad 125
0xa8 120
0x95 103
0x90 98
0x53 52
0x65 68
0x77 84
0xab 123
0xa6 118
0x93 101
0x52 51
0x64 67
0x76 83
0x88 95
0xbc 138
0xa9 121
0xa4 116
0x91 99
0x55 54
0x67 70
0x79 86
0xba 136
0xa7 119
0xa2 114
0x54 53
0x66 69
0x78 85
0x8a 96
0xbd 139
0xb8 134
0xa5 117
0xa0 112
0x57 56
0x69 72
0x7b 88
0xbb 137
0xb6 132
0xa3 115
0x56 55
0x68 71
0x7a 87
0x8c 97
0xcc 146
0xb9 135
0xb4 130
0xa1 113
0x59 58
0x6b 74
0x7d 90
0xca 145
0xb7 133
0xb2 128
0x58 57
0x6a 73
0x7c 89
0xc8 144
0xb5 131
0xb0 126
0x5b 60
0x6d 76
0xc6 143
0xb3 129
0x5a 59
0x6c 75
0xc4 142
0xb1 127
0x5d 62
0xc2 141
0x5c 61
0xc0 140

Figure A.1

Appendix B

Fluorescence detection capabilities - supplement figures

Trigger parameter comparison depending on the array zenith angle

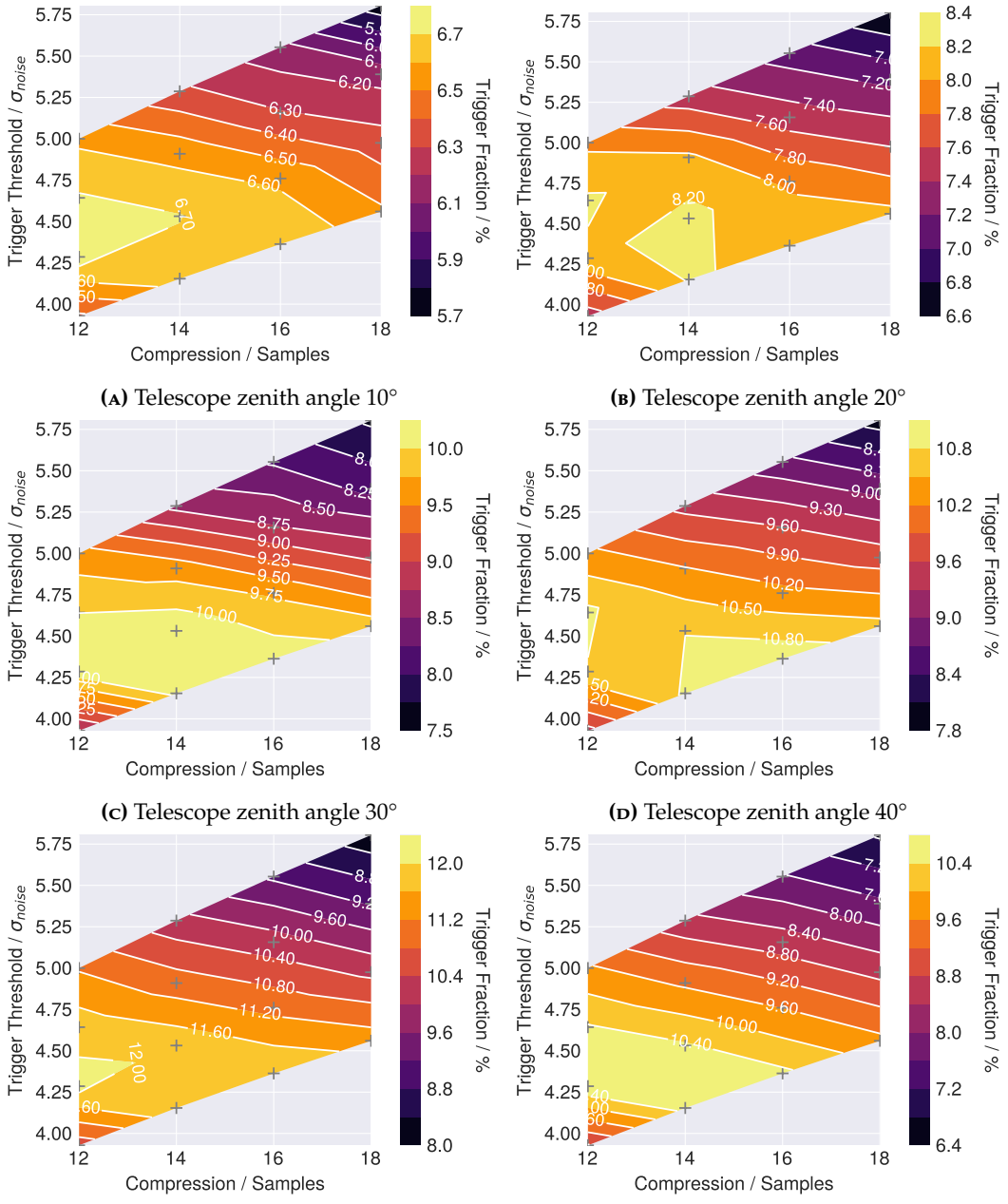

(A) Telescope zenith angle 10°

(B) Telescope zenith angle 20°

(C) Telescope zenith angle 30°

(D) Telescope zenith angle 40°

(E) Telescope zenith angle 50°

(F) Telescope zenith angle 60°

Figure B.1: Trigger fraction of true positive triggered events depending on the telescope zenith angle.

Detection probability

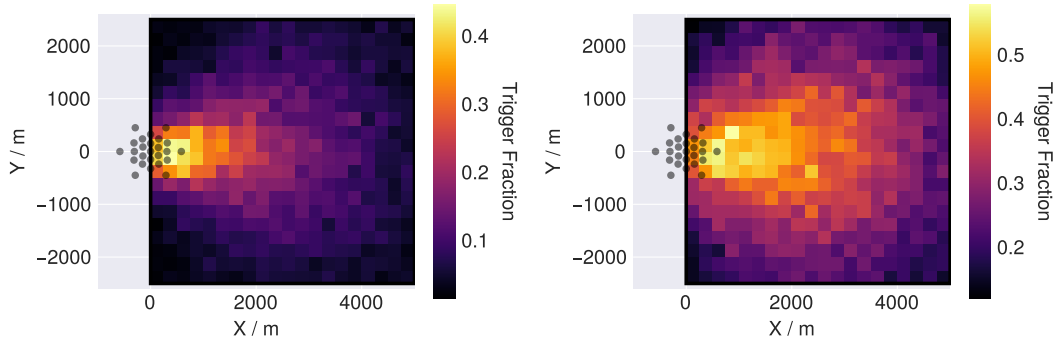

(A) Parallel pointing, array zenith 50°.

(B) Divergent pointing, array zenith 50°.

Figure B.2: Triggered showers in detector level plane. The black boxes are the boundaries of the simulated area, with X pointing towards North and Y pointing West. The simulation boundaries cover a range of 0 m to 5000 m and −2500 m to 2500 m, resulting in an area of 25 km^2. The 2-D Histogram shows the detected fraction of showers in each bin. The grey circles represent the CTA MSTs with mounted FlashCam cameras pointing towards North with a zenith angle of 50°. A multiplicity of 1 to trigger a detection was required.

Relative angular dependence of the detection probability

Figure B.3: Differential fraction $d\epsilon/d\alpha$ of triggered events as a function of the viewing angle α between the air showers and the central telescope for four pointings of the telescope array in divergent pointing mode. The dataset shown contains all four primary particle types and is binned into 4 levels of primary energy. The fractions shown are normalised to the total number of triggered events within each energy bin. A stereoscopic trigger condition was required.

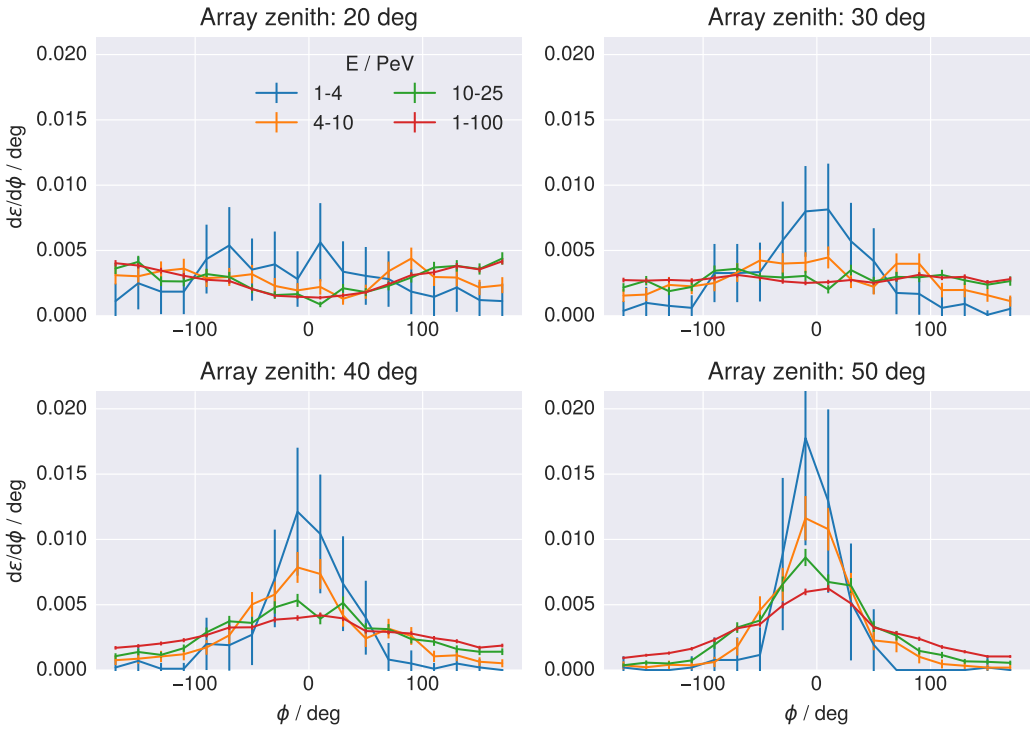

Figure B.4: Differential fraction $d\epsilon/d\phi$ of triggered events as a function of relative azimuth angle ϕ of the air showers and the telescope array (pointing North) for four pointings of the telescope array in divergent pointing mode. Showers incident from North have a relative azimuth angle of 0, while showers coming from behind the array field of view The dataset shown contains all four primary particle types and is binned into 4 levels of primary energy. The fractions shown are normalised to the total number of triggered events within each energy bin. A stereoscopic trigger condition was required.

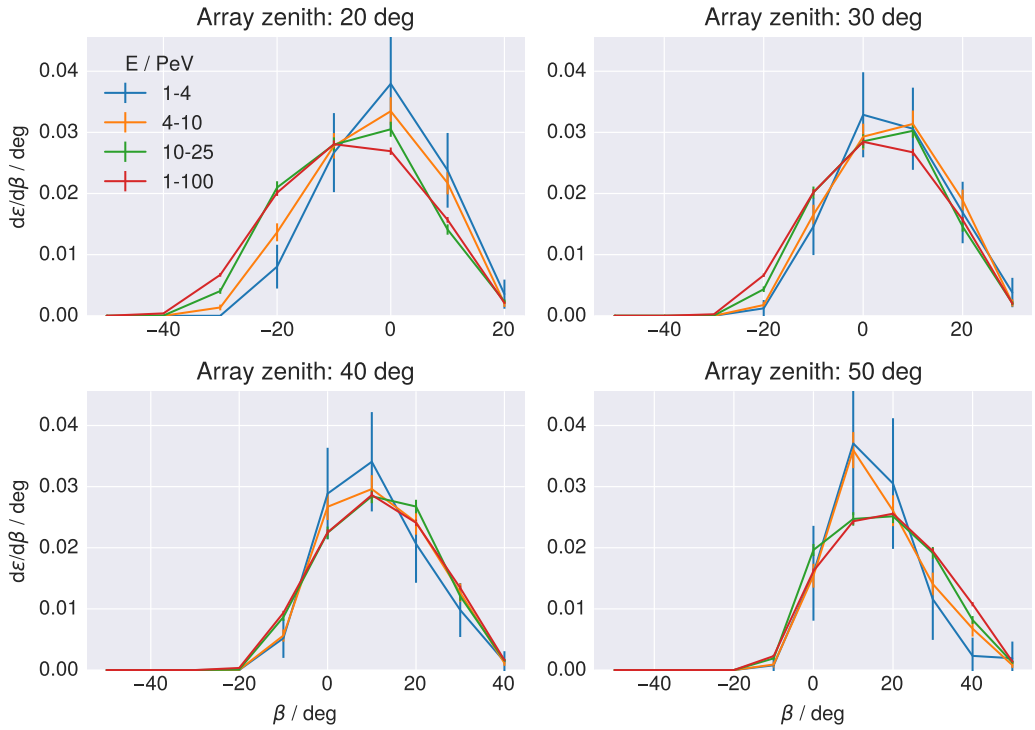

Figure B.5: Differential fraction $d\epsilon/d\beta$ of triggered events as a function of relative zenith angle ϕ of the air showers and the telescope array for four pointings of the telescope array in divergent pointing mode. Positive values of β represent shower zenith angles from above the array pointing, while negative values represent showers coming lower parts of the sky. The dataset shown contains all four primary particle types and is binned into 4 levels of primary energy. The fractions shown are normalised to the total number of triggered events within each energy bin. A stereoscopic trigger condition was required.

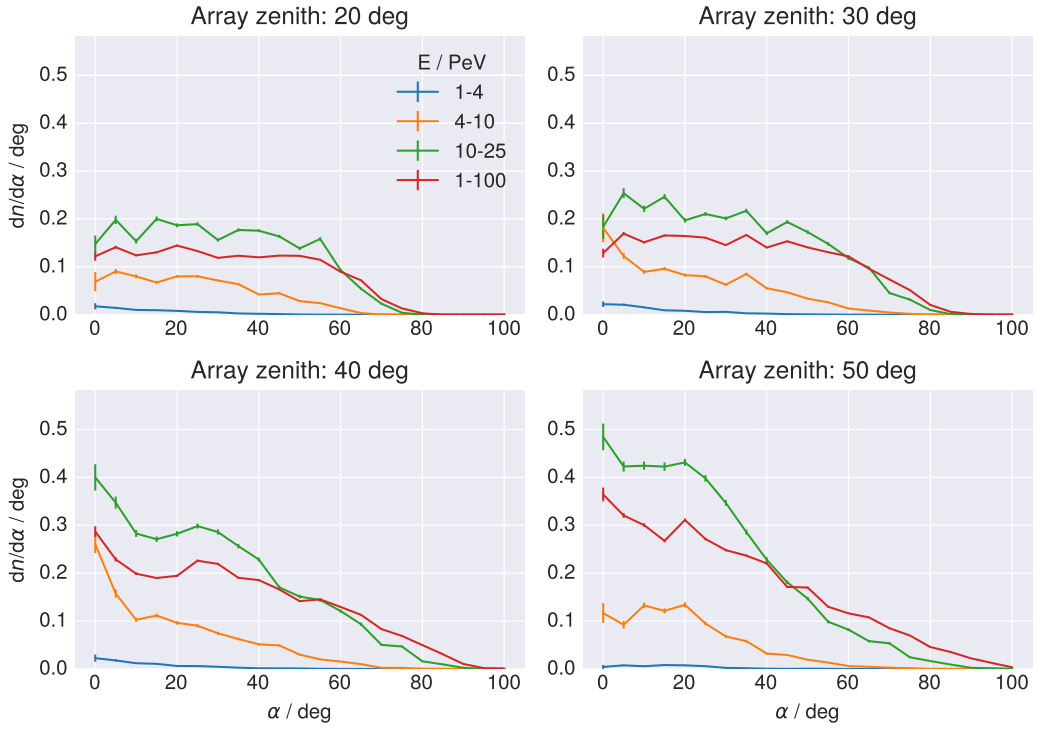

Figure B.6: Differential trigger fraction $dn/d\alpha$ as a function of the viewing angle α between the air showers and the central telescope for four pointings of the telescope array in divergent pointing mode. The dataset shown contains all four primary particle types and is binned into 4 levels of primary energy. The fractions shown are normalised to the total number of *simulated* events within each energy bin. A stereoscopic trigger condition was required.

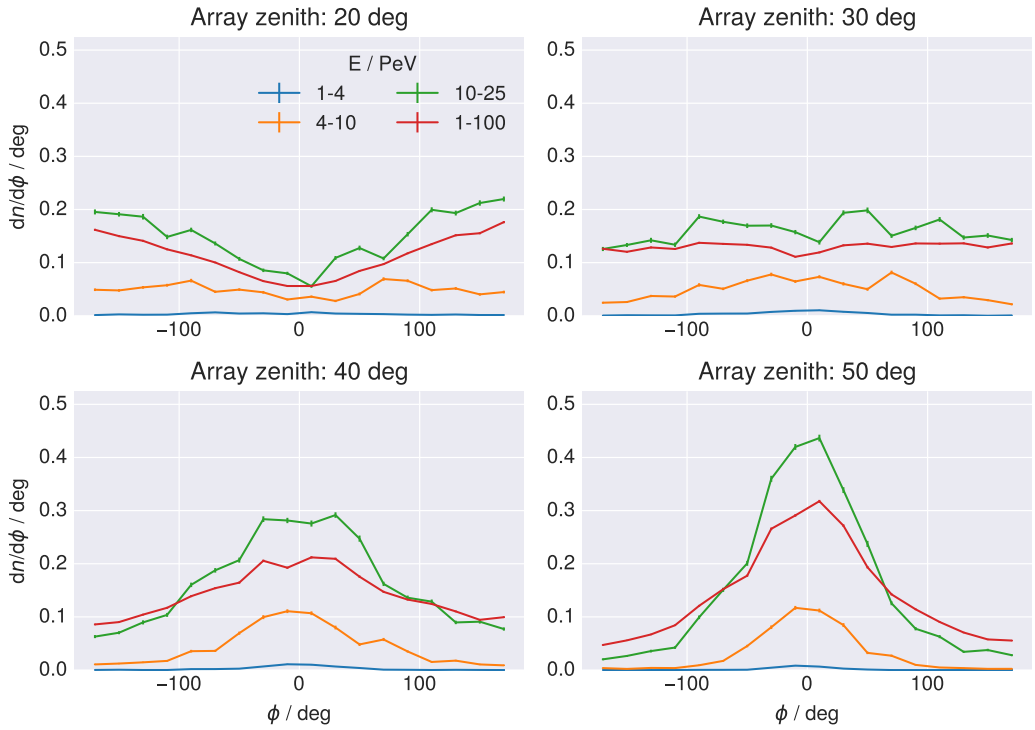

Figure B.7: Differential trigger fraction $dn/d\phi$ as a function of relative azimuth angle ϕ of the air showers and the telescope array (pointing North) for four pointings of the telescope array in divergent pointing mode. Showers incident from North have a relative azimuth angle of 0, while showers coming from behind the array field of view The dataset shown contains all four primary particle types and is binned into 4 levels of primary energy. The fractions shown are normalised to the total number of *simulated* events within each energy bin. A stereoscopic trigger condition was required.

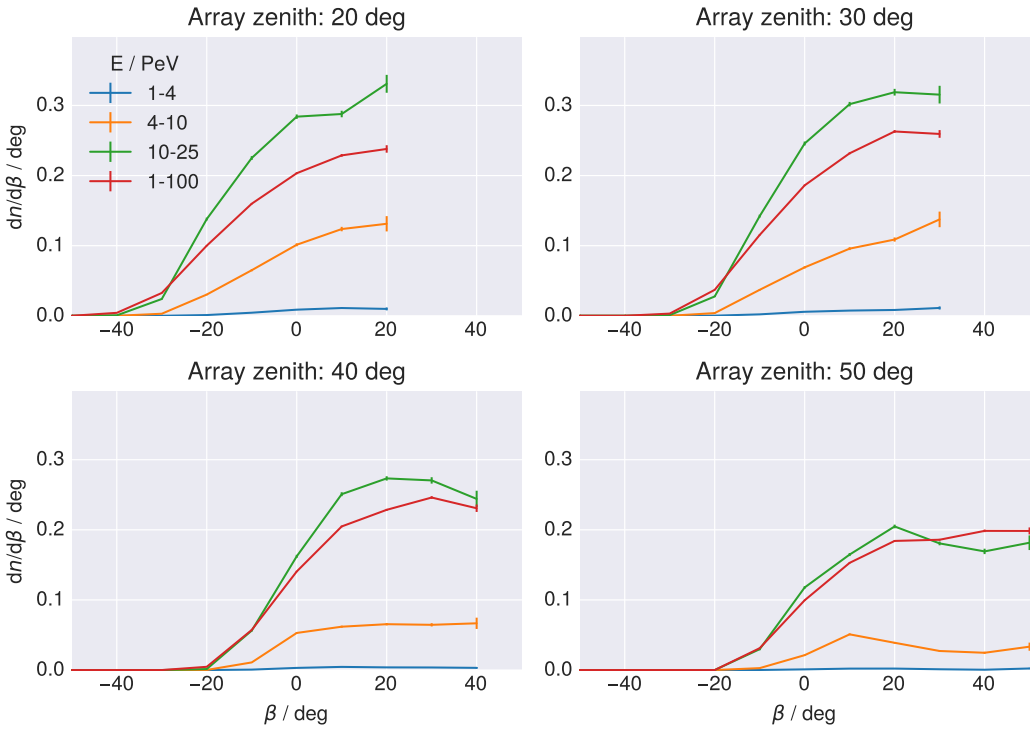

Figure B.8: Differential trigger fraction $dn/d\beta$ as a function of relative zenith angle ϕ of the air showers and the telescope array for four pointings of the telescope array in divergent pointing mode. Positive values of β represent shower zenith angles from above the array pointing, while negative values represent showers coming lower parts of the sky. The dataset shown contains all four primary particle types and is binned into 4 levels of primary energy. The fractions shown are normalised to the total number of *simulated* events within each energy bin. A stereoscopic trigger condition was required.

Cosmic Ray trigger rates

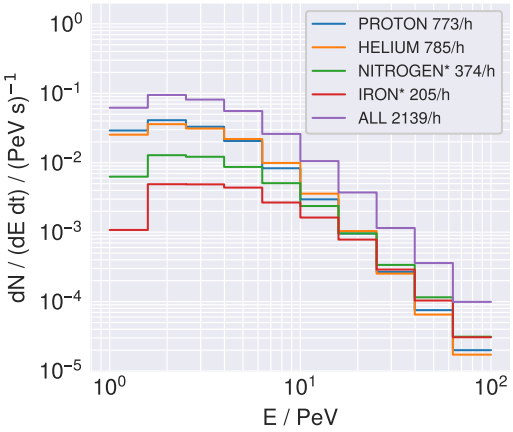

(A) Parallel pointing (40°), min. mono triggers

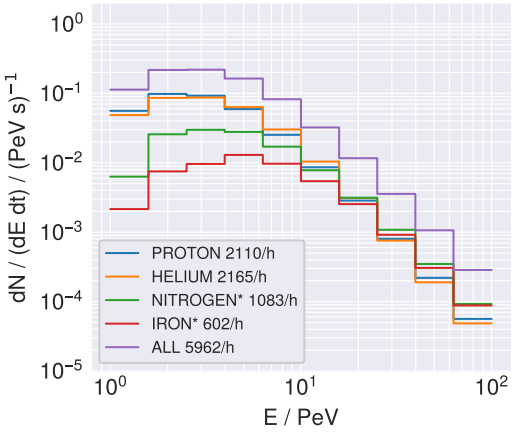

(B) Divergent pointing (40°), min. mono triggers

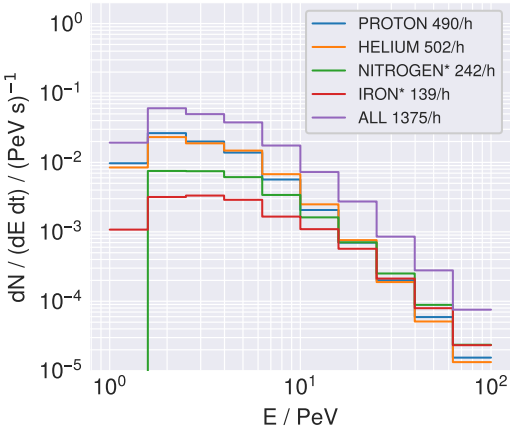

(C) Parallel pointing (40°), min. stereo triggers

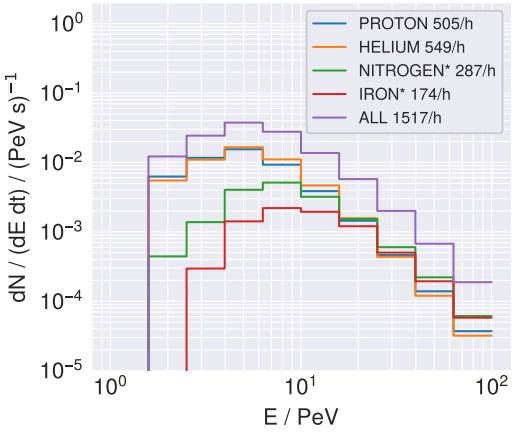

(D) Divergent pointing (40°), min. stereo triggers

Figure B.9: Differential trigger rates due to cosmic ray air showers for four sets of primary particle ranges. The array was pointed at 40° zenith angle in parallel and divergent pointing mode. Compared are also the differences between mono and stereo triggers.

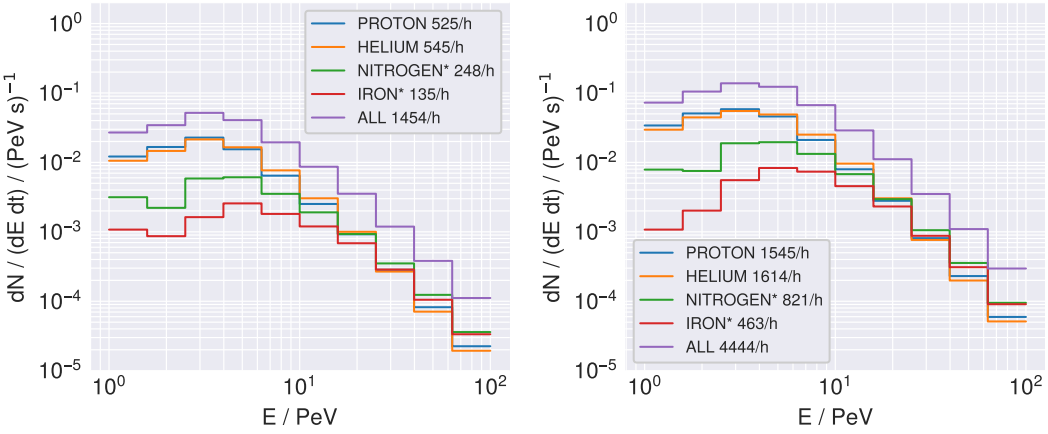

(A) Parallel pointing (50°), min. mono triggers

(B) Divergent pointing (50°), min. mono triggers

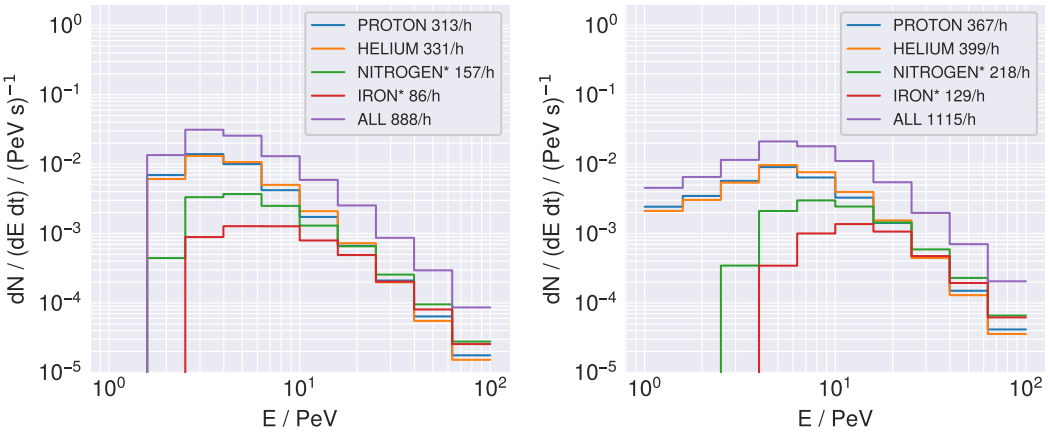

(C) Parallel pointing (50°), min. stereo triggers

(D) Divergent pointing (50°), min. stereo triggers

Figure B.10: Differential trigger rates due to cosmic ray air showers for four sets of primary particle ranges. The array was pointed at 50° zenith angle in parallel and divergent pointing mode. Compared are also the differences between mono and stereo triggers.

Angular resolution

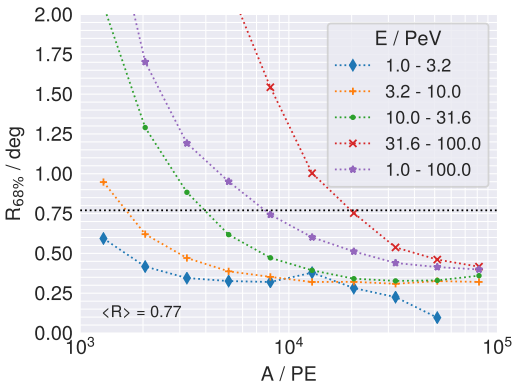

(A) Parallel pointing, min. mono trigger.

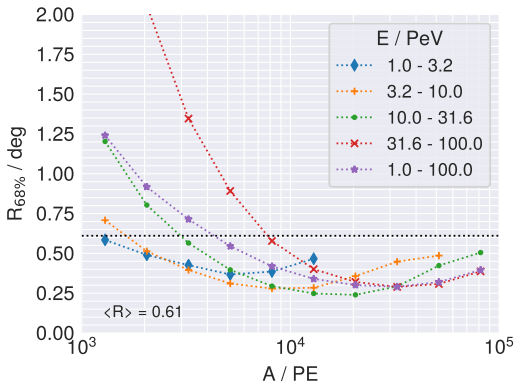

(B) Divergent pointing, min. mono trigger.

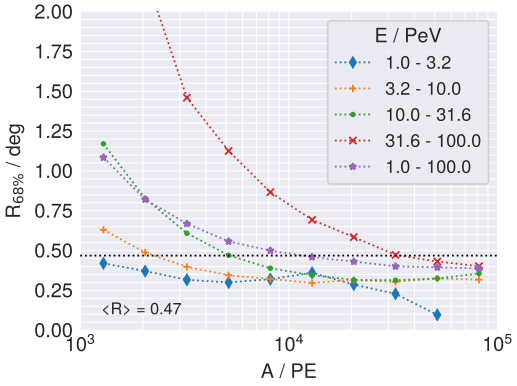

(C) Parallel pointing, min. stereo trigger.

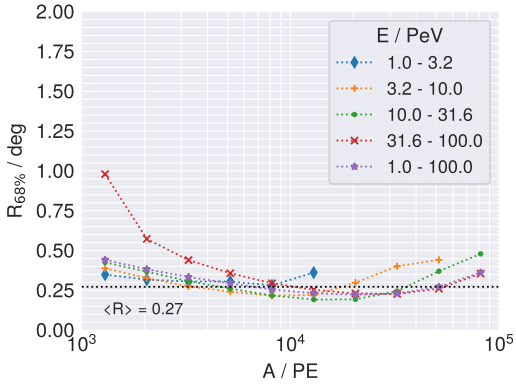

(D) Divergent pointing, min. stereo trigger.

Figure B.11: Angular resolution R of the 25 MST sub-array as a function of image amplitude in reconstructed photoelectrons. The shower axis has been reconstructed with a line-like model. The resolution has been determined by the 68% containment value of the angular offset between the Monte-Carlo truth and the reconstruction direction for each event.

Impact point resolution

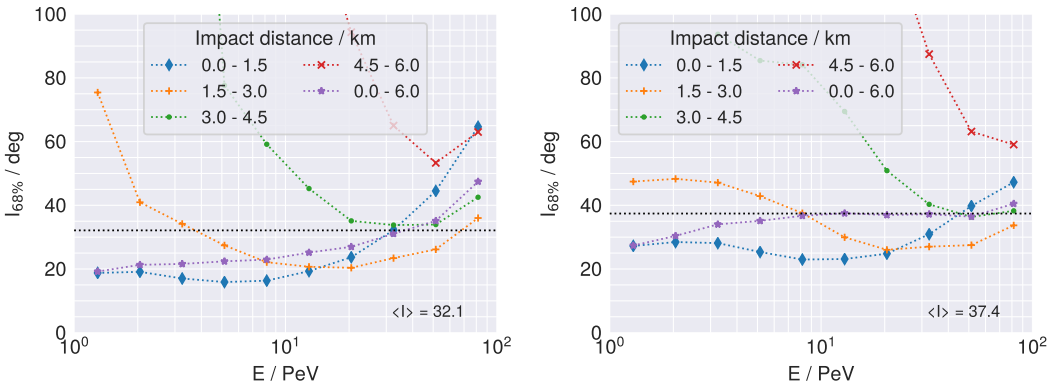

(A) Parallel pointing, min. mono trigger.

(B) Divergent pointing, min. mono trigger.

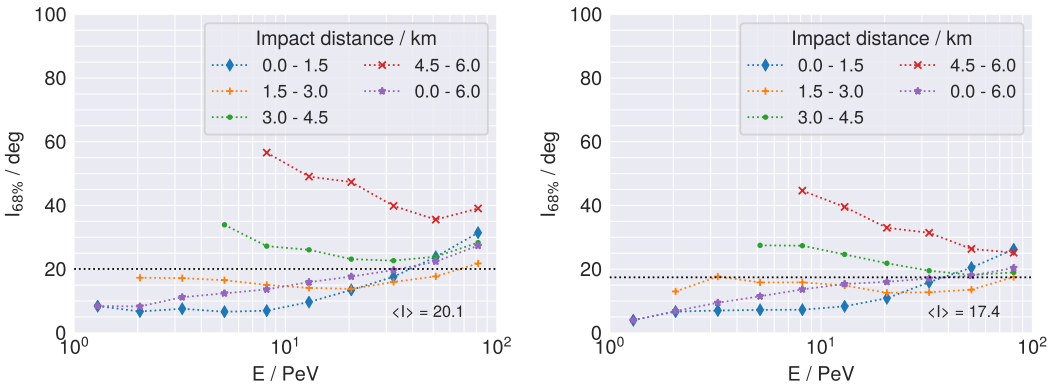

(C) Parallel pointing, min. stereo trigger.

(D) Divergent pointing, min. stereo trigger.

Figure B.12: Impact point resolution I of the 25 MST sub-array as a function of primary energy. The shower axis has been reconstructed with a line-like model. The resolution has been determined by the 68% containment value of the impact point offset between the Monte-Carlo truth and the reconstruction location for each event.

Point source sensitivity

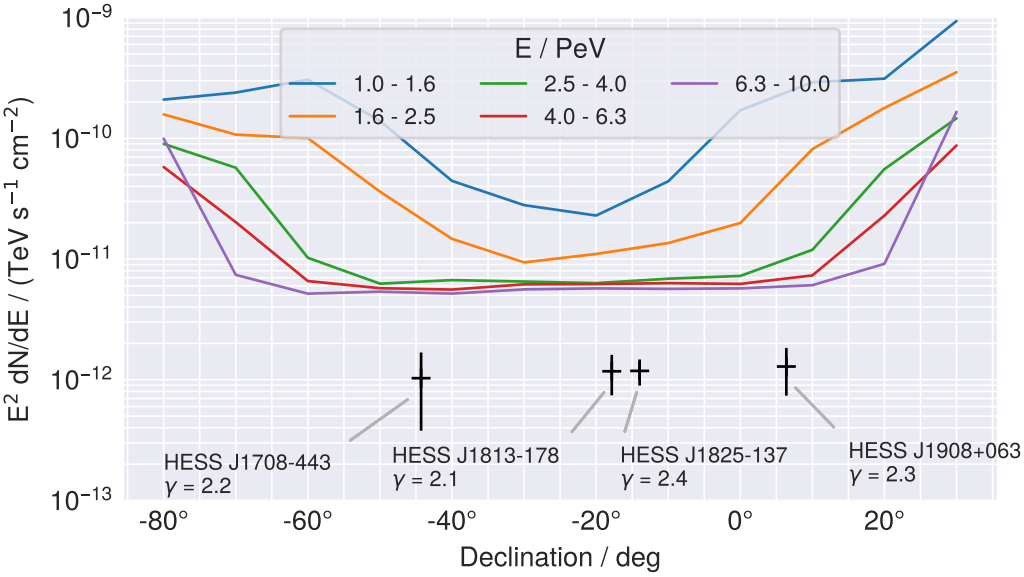

Figure B.13: The differential γ-ray flux sensitivity E^2dN/dE as a function of source declination, for 5 bins in primary energy. Four exemplary sources are shown with their extrapolated fluxes at an energy of 3 PeV. The observation time of the array has been set to 1 year and a divergent array pointing with a PSF of 0.5° has been assumed. No γ/hadron separation has been taken into account.

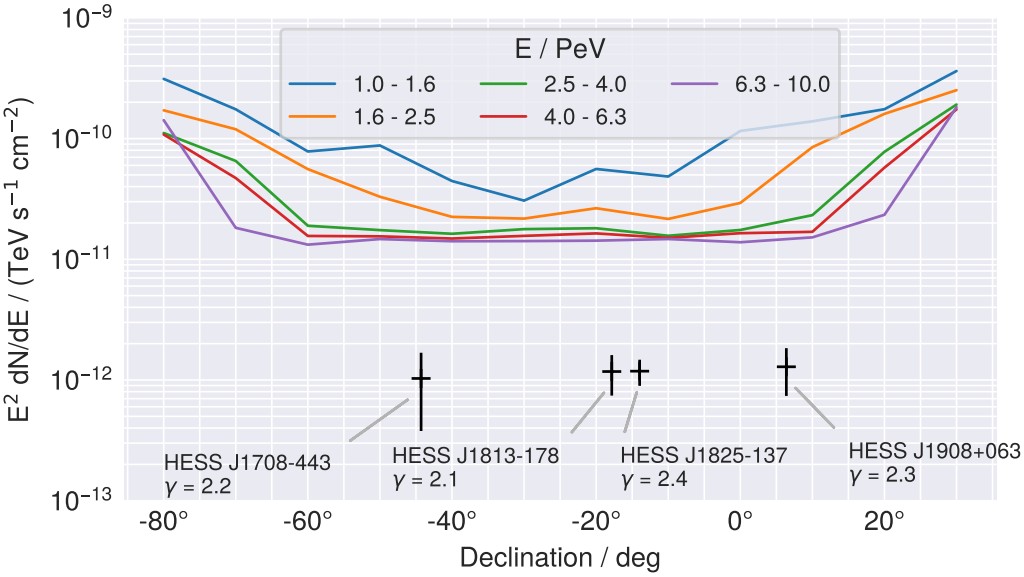

Figure B.14: The differential γ-ray flux sensitivity E^2dN/dE as a function of source declination, for 5 bins in primary energy. Four exemplary sources are shown with their extrapolated fluxes at an energy of 3 PeV. The observation time of the array has been set to 1 year and a parallel array pointing with a PSF of 0.5° has been assumed. No γ/hadron separation has been taken into account.

Acknowledgements

I would like to thank everyone how contributed to the completion of this work! In particular I would like to thank Prof. Jim Hinton for providing me with the opportunity me to work on this thesis, and for refereeing on this work. I would also like to thank Prof. Andreas Quirrenbach for acting as the co-referee. I also would like to mention Jim again, as I could not have wished for a better thesis advisor, for the relaxing atmosphere to work in and the motivation boost, where it was needed.

I would like to thank Felix especially! Words cannot express the gratitude I feel, for receiving me so warmly into the group and the good conversation I have enjoyed very much, for the support and advice. I would like to thank you in particular for proof-reading.. "kurz und knackig".

On a similar level, I want to thank German, for his advice, the breaks, the plots and everything else. I also would like to mention Mizzi for all the time spent outside, fun conversations and his willingness to get out pen&paper and explain everything again. Justus, I would like to thank for his friendship and the fun times we had together, beware of the bugs and birds! Sabina, for the good office conversations and the cookies; Pooja, for sharing the path during this PhD time; Vikas, for the hidden conversations; Axel & Johannes for the Skat and beer rounds. Vincent for checking up on me, it was always appreciated. I would like to mention the IT-group of MPIK, for their endurance regarding my hammering of the cluster and willingness to help. The electronics and mechanics workshop for their sappy welcomes. A special mention must go out to the coffee table, it was always fun, someday that chair will be mine. A general thanks into the round of PhD students, who are an awesome bunch, and the PostDocs, equally awesome. The FlashCam team shall not go unmentioned for the welcoming atmosphere and good collaboration.

I would like to thank anyone I forgot, as my time runs out, printing awaits. Last but not least, I would like to thank my friends and family for the received support and motivation.

Charlie, for your support, caring and love, you made the last years wonderful.

Bibliography

[1] M. G. Aartsen et al. "Search for PeV Gamma-Ray Emission from the Southern Hemisphere with 5 Yr of Data from the IceCube Observatory". In: *The Astrophysical Journal* 891.1 (Feb. 2020), p. 9. DOI: 10.3847/1538-4357/ab6d67.

[2] A. U. Abeysekara et al. "Multiple Galactic Sources with Emission Above 56 TeV Detected by HAWC". In: *Phys. Rev. Lett.* 124 (2 Jan. 2020), p. 021102. DOI: 10.1103/PhysRevLett.124.021102. URL: https://link.aps.org/doi/10.1103/PhysRevLett.124.021102.

[3] Jiju Abraham et al. "The Fluorescence Detector of the Pierre Auger Observatory". In: *Nuclear Instruments and Methods in Physics Research Section A Accelerators Spectrometers Detectors and Associated Equipment* 620 (July 2009). DOI: 10.1016/j.nima.2010.04.023.

[4] Felix Aharonian, Rui-Zhi Yang, and Emma Wilhelmi. "Massive Stars as Major Factories of Galactic Cosmic Rays". In: *Nature Astronomy* 3 (June 2019). DOI: 10.1038/s41550-019-0724-0.

[5] R. Aloisio, V. Berezinsky, and A. Gazizov. "Transition from galactic to extragalactic cosmic rays". In: *Astroparticle Physics* 39 (Dec. 2012), pp. 129–143. DOI: 10.1016/j.astropartphys.2012.09.007. arXiv: 1211.0494 [astro-ph.HE].

[6] E. G. Berezhko. "Maximum energy of cosmic rays accelerated by supernova shocks". In: *Astroparticle Physics* 5 (Oct. 1996), pp. 367–378. DOI: 10.1016/0927-6505(96)00037-0.

[7] K. Bernlöhr et al. "Monte Carlo design studies for the Cherenkov Telescope Array". In: *Astroparticle Physics* 43 (2013). Seeing the High-Energy Universe with the Cherenkov Telescope Array - The Science Explored with the CTA, pp. 171 –188. ISSN: 0927-6505. DOI: https://doi.org/10.1016/j.astropartphys.2012.10.002. URL: http://www.sciencedirect.com/science/article/pii/S0927650512001867.

[8] Konrad Bernlöhr. "Simulation of imaging atmospheric Cherenkov telescopes with CORSIKA and sim_telarray". In: *Astroparticle Physics* 30.3 (2008), pp. 149 –158. ISSN: 0927-6505. DOI: https://doi.org/10.1016/j.astropartphys.2008.07.009. URL: http://www.sciencedirect.com/science/article/pii/S0927650508000972.

[9] C. Bigongiari. "The MAGIC telescope". In: *International Europhysics Conference on High Energy Physics, HEP2005*. Jan. 2005, p. 20. arXiv: astro-ph/0512184 [astro-ph].

[10] Extensive Air Shower Simulation with CORSIKA: A User's Guide. *D. Heck and T. Pierog*. URL: https://web.ikp.kit.edu/corsika/usersguide/usersguide.pdf.

[11] Hans Dembinski et al. "Data-driven model of the cosmic-ray flux and mass composition from 10 GeV to 10^{11} GeV". In: *PoS* ICRC2017 (2017), p. 533. DOI: 10.22323/1.301.0533. URL: https://www.mpi-hd.mpg.de/personalhomes/hdembins/.

[12] A. Donath et al. "Gammapy: An open-source Python package for gamma-ray astronomy". In: *34th International Cosmic Ray Conference (ICRC2015)*. Vol. 34. International Cosmic Ray Conference. July 2015, p. 789. arXiv: 1509.07408 [astro-ph.IM].

[13] Luke O'C. Drury. "Origin of cosmic rays". In: *Astroparticle Physics* 39-40 (2012). Cosmic Rays Topical Issue, pp. 52 –60. ISSN: 0927-6505. DOI: https://doi.org/10.1016/j.astropartphys.2012.02.006. URL: http://www.sciencedirect.com/science/article/pii/S092765051200045X.

[14] G. Dubus et al. "Surveys with the Cherenkov Telescope Array". In: *Astroparticle Physics* 43 (2013). Seeing the High-Energy Universe with the Cherenkov Telescope Array - The Science Explored with the CTA, pp. 317 –330. ISSN: 0927-6505. DOI: https://doi.org/10.1016/j.astropartphys.2012.05.020. URL: http://www.sciencedirect.com/science/article/pii/S0927650512001259.

[15] Stefan Eschbach. "A detailed characterization of PMTs for the CTA project and analysis of first FlashCam prototype data". PhD thesis. Friedrich-Alexander-Universität Erlangen-Nürnberg, 2019.

[16] A. Gadola G. Hermann G. Pühlhofer and F. Werner. *FlashCam Technical Design Report*. Tech. rep. 2016.

[17] T K Gaisser. "The Cosmic-ray Spectrum: from the knee to the ankle". In: *Journal of Physics: Conference Series* 47 (Oct. 2006), pp. 15–20. DOI: 10.1088/1742-6596/47/1/002.

[18] T. K. Gaisser and A. M. Hillas. "Reliability of the Method of Constant Intensity Cuts for Reconstructing the Average Development of Vertical Showers". In: *International Cosmic Ray Conference*. Vol. 8. International Cosmic Ray Conference. Jan. 1977, p. 353.

[19] Markus Garczarczyk et al. "Status of the Medium-Sized Telescope for the Cherenkov Telescope Array". In: (Sept. 2015).

[20] J.-F. Glicenstein and M. Shayduk. "NectarCAM, a camera for the medium sized telescopes of the Cherenkov telescope array". In: *AIP Conference Proceedings* 1792.1 (2017), p. 080009. DOI: 10.1063/1.4969030. eprint: https://aip.scitation.org/doi/pdf/10.1063/1.4969030. URL: https://aip.scitation.org/doi/abs/10.1063/1.4969030.

[21] D. Góra et al. "Universal lateral distribution of energy deposit in air showers and its application to shower reconstruction". In: *Astroparticle Physics* 24.6 (2006), pp. 484 –494. ISSN: 0927-6505. DOI: https://doi.org/10.1016/j.astropartphys.2005.09.007. URL: http://www.sciencedirect.com/science/article/pii/S0927650505001453.

[22] H. E. S. S. Collaboration et al. "Detection of very-high-energy γ-ray emission from the vicinity of PSR B1706-44 and G 343.1-2.3 with H.E.S.S." In: *Astronomy & Astrophysics* 528, A143 (Apr. 2011), A143. DOI: 10.1051/0004-6361/201015381. arXiv: 1102.0773 [astro-ph.HE].

[23] H. E. S. S. Collaboration et al. "The H.E.S.S. Galactic plane survey". In: *Astronomy & Astrophysics* 612, A1 (Apr. 2018), A1. DOI: 10.1051/0004-6361/201732098. arXiv: 1804.02432 [astro-ph.HE].

[24] D. Heck et al. *CORSIKA: a Monte Carlo code to simulate extensive air showers.* 1998.

[25] G. Hermann et al. "A Trigger And Readout Scheme For Future Cherenkov Telescope Arrays". In: 1085 (Dec. 2008). DOI: 10.1063/1.3076822.

[26] HESS Collaboration et al. "Acceleration of petaelectronvolt protons in the Galactic Centre". In: *Nature* 531.7595 (Mar. 2016), pp. 476–479. DOI: 10.1038/nature17147. arXiv: 1603.07730 [astro-ph.HE].

[27] A. M. Hillas. "Cerenkov Light Images of EAS Produced by Primary Gamma Rays and by Nuclei". In: *19th International Cosmic Ray Conference (ICRC19), Volume 3*. Vol. 3. International Cosmic Ray Conference. Aug. 1985, p. 445.

[28] J.A. Hinton and W. Hofmann. "Teraelectronvolt Astronomy". In: *Annual Review of Astronomy and Astrophysics* 47.1 (2009), pp. 523–565. DOI: 10.1146/annurev-astro-082708-101816. eprint: https://doi.org/10.1146/annurev-astro-082708-101816. URL: https://doi.org/10.1146/annurev-astro-082708-101816.

[29] Werner Hofmann. "The high energy stereoscopic system (HESS) project". In: vol. 515. June 2000, pp. 500–509. DOI: 10.1063/1.1291416.

[30] J. Holder et al. "The first VERITAS telescope". In: *Astroparticle Physics* 25 (May 2013), p. 391. DOI: 10.1016/j.astropartphys.2006.04.002.

[31] Jörg R. Hörandel. "Models of the knee in the energy spectrum of cosmic rays". In: *Astroparticle Physics* 21.3 (2004), pp. 241 –265. ISSN: 0927-6505. DOI: https://doi.org/10.1016/j.astropartphys.2004.01.004. URL: http://www.sciencedirect.com/science/article/pii/S0927650504000209.

[32] IceCube Collaboration et al. "Search for steady point-like sources in the astrophysical muon neutrino flux with 8 years of IceCube data". In: *Eur. Phys. J. C* 79.3 (2019), p. 234. DOI: 10.1140/epjc/s10052-019-6680-0.

[33] *Intel Intrinsics Guide*. Accessed: 2020-08-08. URL: https://software.intel.com/sites/landingpage/IntrinsicsGuide/.

[34] Steven G. Johnson. *The NLopt nonlinear-optimization package*. URL: http://github.com/stevengj/nlopt.

[35] Ian Jolliffe. "Principal Component Analysis". In: *International Encyclopedia of Statistical Science*. Ed. by Miodrag Lovric. Berlin, Heidelberg: Springer Berlin Heidelberg, 2011, pp. 1094–1096. ISBN: 978-3-642-04898-2. DOI: 10.1007/978-3-642-04898-2_455.

[36] Rudolph Emil Kalman. "A New Approach to Linear Filtering and Prediction Problems". In: *Transactions of the ASME–Journal of Basic Engineering* 82.Series D (1960), pp. 35–45.

[37] J. Kildea et al. "The Whipple Observatory 10m gamma-ray telescope, 1997–2006". In: *Astroparticle Physics* 28.2 (2007), pp. 182 –195. ISSN: 0927-6505. DOI: https://doi.org/10.1016/j.astropartphys.2007.05.004. URL: http://www.sciencedirect.com/science/article/pii/S0927650507000746.

[38] M. Kobal and Pierre Auger Collaboration. "A thinning method using weight limitation for air-shower simulations". In: *Astroparticle Physics* 15.3 (June 2001), pp. 259–273. DOI: 10.1016/S0927-6505(00)00158-4.

[39] G. Lefeuvre et al. "Absolute measurement of the nitrogen fluorescence yield in air between 300 and 430nm". In: *Nuclear Instruments and Methods in Physics Research Section A: Accelerators, Spectrometers, Detectors and Associated Equipment* 578.1 (2007), pp. 78 –87. ISSN: 0168-9002. DOI: https://doi.org/10.1016/j.nima.2007.04.106. URL: http://www.sciencedirect.com/science/article/pii/S0168900207006912.

[40] T. P. Li and Y. Q. Ma. "Analysis methods for results in gamma-ray astronomy." In: *The Astrophysical Journal* 272 (Sept. 1983), pp. 317–324. DOI: 10.1086/161295.

[41] J. Matthews. "A Heitler model of extensive air showers". In: *Astroparticle Physics* 22.5 (2005), pp. 387 –397. ISSN: 0927-6505. DOI: https://doi.org/10.1016/j.astropartphys.2004.09.003. URL: http://www.sciencedirect.com/science/article/pii/S0927650504001598.

[42] J A J Matthews et al. "A parameterization of cosmic ray shower profiles based on shower width". In: *Journal of Physics G: Nuclear and Particle Physics* 37.2 (Jan. 2010), p. 025202. DOI: 10.1088/0954-3899/37/2/025202.

[43] R. Mirzoyan et al. "The First telescope of the HEGRA air Cherenkov imaging telescope array". In: *Nucl. Instrum. Meth. A* 351 (1994), pp. 513–526. DOI: 10.1016/0168-9002(94)91381-1.

[44] A. Mitchell et al. "Observations of the Pulsar Wind Nebula HESS J1825-137 with H.E.S.S. II". In: *35th International Cosmic Ray Conference (ICRC2017)*. Vol. 301. International Cosmic Ray Conference. Jan. 2017, p. 707. arXiv: 1708.03126 [astro-ph.HE].

[45] J.M.C. Montanus. "An extended Heitler–Matthews model for the full hadronic cascade in cosmic air showers". In: *Astroparticle Physics* 59 (2014), pp. 4 –11. ISSN: 0927-6505. DOI: https://doi.org/10.1016/j.astropartphys.2014.03.010. URL: http://www.sciencedirect.com/science/article/pii/S0927650514000383.

[46] J.M.C. Montanus. "Intermediate models for longitudinal profiles of cosmic showers". In: *Astroparticle Physics* 35.10 (2012), pp. 651 –659. ISSN: 0927-6505. DOI: https://doi.org/10.1016/j.astropartphys.2012.01.006. URL: http://www.sciencedirect.com/science/article/pii/S0927650512000278.

[47] D. Morcuende et al. "Relevance of the fluorescence radiation in VHE gamma-ray observations with the Cherenkov technique". In: *Astroparticle Physics* 107 (2019), pp. 26 –34. ISSN: 0927-6505. DOI: https://doi.org/10.1016/j.astropartphys.2018.11.003. URL: http://www.sciencedirect.com/science/article/pii/S0927650518301725.

[48] A. Obermeier. *The Fluorescence Yield of Air excited by Electron measured with the AIRFLY Experiment*. 2007.

[49] CTA Observatory. URL: https://www.cta-observatory.org.

[50] *OpenMP Gnu Linux*. Accessed: 2020-08-08. URL: https://gcc.gnu.org/projects/gomp/.

[51] M. Powell. "The BOBYQA Algorithm for Bound Constrained Optimization without Derivatives". In: *Technical Report, Department of Applied Mathematics and Theoretical Physics* (2009).

[52] Sabina Pürckhauer. "Characterising light concentrators for CTA and optimising the data selection to improve angular resolution and sensitivity". PhD thesis. University of Heidelberg, 2018.

[53] G. Pühlhofer et al. "FlashCam: A fully digital camera for CTA telescopes". In: 1505 (Nov. 2012). DOI: 10.1063/1.4772375.

[54] Jaime Rosado, Francisco Blanco, and Fernando Arqueros. "On the absolute value of the air-fluorescence yield". In: *Astroparticle Physics* 55 (2014), pp. 51 –62. ISSN: 0927-6505. DOI: https://doi.org/10.1016/j.astropartphys.2014.02.003. URL: http://www.sciencedirect.com/science/article/pii/S0927650514000152.

[55] F. Schmidt. year. URL: https://www.ikp.kit.edu/corsika/.

[56] *Science with the Cherenkov Telescope Array*. WORLD SCIENTIFIC, 2019. DOI: 10.1142/10986. URL: https://www.worldscientific.com/doi/abs/10.1142/10986.

[57] Silvia Vernetto and Paolo Lipari. "The Galactic diffuse gamma ray emission in the energy range 30 TeV - 3 PeV". In: *PoS* ICRC2017 (2018), p. 718. DOI: 10.22323/1.301.0718.

[58] Pauli Virtanen et al. "SciPy 1.0: Fundamental Algorithms for Scientific Computing in Python". In: *Nature Methods* 17 (2020), pp. 261–272. DOI: https://doi.org/10.1038/s41592-019-0686-2.

[59] Heinrich J. Völk and Konrad Bernlöhr. "Imaging very high energy gamma-ray telescopes". In: *Experimental Astronomy* 25.1-3 (Aug. 2009), pp. 173–191. DOI: 10.1007/s10686-009-9151-z. arXiv: 0812.4198 [astro-ph].

[60] F. Werner et al. "Performance verification of the FlashCam prototype camera for the Cherenkov Telescope Array". In: *Nuclear Instruments and Methods in Physics Research A* 876 (Dec. 2017), pp. 31–34. DOI: 10.1016/j.nima.2016.12.056. arXiv: 1612.09528 [astro-ph.IM].

[61] J. G. Wilson and K. Greisen. *Progress in cosmic ray physics. Vol. 3*. Amsterdam : North-Holland, 1956.